From Continuum Mechanics to Smoothed Particle Hydrodynamics for Shocks through Inhomogeneous Media

Iason Zisis

This research was carried out under project number M11.4.10412 in the framework of the Research Program of the Materials innovation institute (M2i) (www.m2i.nl).

From Continuum Mechanics to Smoothed Particle Hydrodynamics for Shocks through Inhomogeneous Media / by Iason Zisis. –

A catalogue record is available from the Eindhoven University of Technology Library.
ISBN: 978-90-386-4297-0

From Continuum Mechanics to Smoothed Particle Hydrodynamics for Shocks through Inhomogeneous Media

PROEFSCHRIFT

ter verkrijging van de graad van doctor aan de Technische Universiteit Eindhoven, op gezag van de rector magnificus prof.dr.ir. F.P.T. Baaijens, voor een commissie aangewezen door het College voor Promoties, in het openbaar te verdedigen op dinsdag 27 juni om 16.00 uur

door

Iason Zisis

geboren te Athene, Griekenland

Dit proefschrift is goedgekeurd door de promotoren en de samenstelling van de promotiecommissie is als volgt:

voorzitter:	prof.dr.ir. J.J. van Wijk
promotor:	prof.dr.ir. B. Koren
copromotor:	dr.ir. B.J. van der Linden (LIME BV en TU Eindhoven)
copromotor:	dr. C.G. Giannopapa (ESA en TU Eindhoven)
leden:	dr. G. Drolshagen (ESA)
	dr. S.W. Rienstra (TU Eindhoven)
	prof.dr. M. Souli (U Lille)
	prof.dr. F. Toschi (TU Eindhoven)

Het onderzoek dat in dit proefschrift wordt beschreven is uitgevoerd in overeenstemming met de TU/e Gedragscode Wetenschapsbeoefening

Abstract

This thesis studies the Smoothed Particle Hydrodynamics (SPH) computational method and its ability to describe multiphase fully compressible flows. By employing the framework of measure-valued evolutions, it is possible to derive the discrete SPH equations from the principles of continuum mechanics. The derivation shows that SPH is indeed the computational method which solves the equations of continuum mechanics for a special type of medium: the smoothed medium. It is precisely the fact that SPH abides by the principles of continuum mechanics, which allows for exact conservation of mass, momentum and energy even for domains under extreme deformations. An analysis of SPH shows the effect of the smoothing length in the resolution of the scheme and how one may choose between different smoothing functions while keeping the same resolution. The relation of the smoothing length to the local number of particles is introduced in the context of measures, thus providing the necessary tool to study the conditions under which the constructed smoothed medium converges to the classical continuum model. Various one- and two-dimensional multiphase compressible tests serve validation purposes and allow for the comparison of the developed schemes. The coupling of number density to the smoothing length plays a critical role in the stable evolution of the SPH system. Finally, the developed multiphase fully compressible SPH scheme, which respects this specific coupling, is applied to the computational analysis of hypervelocity impacts. Upon validation with a set of well-referenced hypervelocity-impact experiments, it is used for the analysis of deformation patterns of laminated materials. The developed scheme simulates well the opening pattern of the laminate, when the latter is modeled as a medium with discontinuous density and material parameters. When the laminate is modeled as a homogenized material —similar to what the current state of the art suggests— a significantly different opening pattern is observed.

In memory of my grandparents,
for their love and support.

Contents

Synopsis

The present thesis begins by considering in Chapter 1, the Introduction, the propagation of shock waves through continuous media. Shock waves are thin regions of steep gradients, which —under appropriate assumptions— can be idealized as discontinuities in the distribution of density and the other related quantities. In case of inhomogeneous media, reflections and transmissions may occur, whenever a shock encounters an interface separating parts of the medium with different properties.

Shocks in gases are easier to create than in solids, where shock-compression is achieved only through rapid impulse-loading. Hypervelocity impacts are perhaps the most distinguished examples of such processes. They typically occur in space, where small-sized meteoroids or space debris may hit a spacecraft at speeds comparable to the speed of sound through the involved materials and thus may seriously endanger the integrity of a spacecraft. To this end, materials on the surface of spacecraft work as protection shields. These shields are not always monolithic materials, but may be laminated instead. The accurate simulation of the resulting wave patterns through the laminated materials poses a challenge.

In the second part of the Introduction, the Smoothed Particle Hydrodynamics (SPH) method is reviewed. SPH is the state of the art for the computational analysis of hypervelocity impacts, due to the advantages it offers as a mesh-free method. SPH is also used as a hydrocode in the analysis of numerous other flows, such as gas dynamics or free-surface flows. Over the last decades there has been substantial growth in the interest of simulating multiphase processes with the SPH method. The research of SPH schemes for weakly compressible flows has advanced and achieved remarkable results. A challenge is to extend the applicability of these SPH schemes to the fully compressible regime. Some new insight into SPH schemes is necessary, if shock propagation through inhomogeneous materials with SPH is to be studied.

Chapter 2 is devoted to an analysis of the SPH method. Literature shows that various functions can serve as smoothing functions, for the construction of smooth discrete estimates, necessary in the context of SPH. To this end, a characteristic length over which the smoothing operation takes place, becomes crucial. A common smoothing length does not incur the same resolution for all smoothing functions. We extend recent literature by showing that there is a link between the standard deviation of any smoothing function with the resulting smoothing length. By this, we are able to endow the same resolution to the SPH scheme, independently of the smoothing function used. Further on, we present ways to construct smooth estimates of a system's quantities. A clear distinction is made between the estimates of invariant quantities, which should be constructed as measures, and variant quantities in the system under study. We observe the significance of the number density in this construction.

From the point of view of computational mechanics, the concept of SPH is to create a link between a continuous medium and a discretized particle system. In order to mitigate any ambiguities and to obtain a better understanding, Chapter 3 presents a novel comparative derivation of the equations of classical continuum mechanics and those for a medium with smoothed density profile —the smoothed medium. It turns out that three well-referenced SPH schemes can be constructed using the following building blocks: 1) one of three basic measures: probability, counting or Lebesgue measure, 2) the principle of least action from continuum mechanics and, 3) an appropriate thermodynamical relation, which leads to the modeling of the desired properties of any medium. The side-by-side derivation of the governing equations of classical continuum mechanics portrays the conditions under which the smoothed system converges to the classical one. After obtaining the governing equations in the continuous setting, a discretization of the introduced measure allows for a formal pass to the discrete setting. Additionally, based on the developed framework, we treat media with full-stress response and underline the differences between constructing the smoothed equations for total Lagrangian versus the smoothed equations in updated Lagrangian description. Moreover, we include deviatoric stresses in a consistent manner, allowing for the modeling of viscous fluids and plastic solids.

In Chapter 4 we discuss issues regarding artificial dissipation and construct a new dissipative mass flux, necessary to counteract numerical instabilities around contact discontinuities. We give numerical evidence that the SPH method converges with respect to the Wasserstein distance, as suggested by relevant theoretical findings from the literature.

The developed schemes are validated in Chapter 5, against a collection of one-dimensional multiphase shock problems, with known analytical solutions. Specifically, the three developed schemes and two different configurations of particles are compared. The two different configurations refer to particles of equal mass with the interparticle distances describing the initial density ratio or particles placed in a uniform pattern with their masses depicting the mass ratio. We see that irrespectively of the configuration, the scheme employing the evolution of the number density outperforms the others. The validation of the selected scheme in two spatial dimensions is achieved via three multiphase flow problems.

Finally, in Chapter 6 the developed schemes are used for the simulation of hypervelocity impact experiments into various materials. The schemes provide improved results compared to results reported in the relevant literature, while it also becomes evident that the solution strategy is generic for any hypervelocity impact problem. Last but not least, we simulate a hypervelocity impact experiment into an inhomogeneous layered material. The algorithm is indeed able to yield the details wanted from such simulations and results give confidence that good quantitative comparison is achievable, provided that more realistic material models are used.

CHAPTER 1

Introduction

1.1 Shock propagation

Let us consider a convoy of cars moving on a narrow road at the same constant speed and at equal distances between successive cars. At the head of the convoy, there is a large heavy truck which abruptly breaks down and instantaneously stops. This disturbance in the traffic is understood by the driver of the first car, who starts breaking. Similarly, the rest of the drivers notice the disturbance, each one due to the reaction of the driver just in front and thus, the disturbance propagates at a finite speed. If the cars are moving at any speed smaller than a critical value, they are not going to crash. After some time, the convoy is compressed (smaller gaps between cars), but the cars remain intact. If the common speed at which the cars are moving is higher than the critical speed, the crash is inevitable. In both cases above, a disturbance in the traffic occurs, travels through the convoy and results in a denser configuration of the convoy. Profoundly, in case the cars crash, a special characteristic is apparent: *the disturbance travels so fast that the convoy is unable to accommodate to it*.

The traffic situation above is an analogue of what may actually happen in continuous media. Disturbances which invoke the compression of continuous media, meaning a change in their local density in the same way the car density on the road changes in the paradigm above, are pressure waves[1]. In case the disturbance is moving faster than

[1] Interestingly, Whitham [1999], Ch.1, argues that: "there appears to be no single precise definition of what exactly constitutes a wave. Various restrictive definitions can be given, but to cover the whole range of wave phenomena it seems preferable to be guided by the intuitive view that a wave is any

adjacent matter can "get out of the way", superposition of the propagated pressure waves leads to increased pressure amplitudes, steep gradients and ultimately, the creation of *shock waves*. These are abrupt jumps in pressure, density, and velocity [Whitham [1999], Ch.1, Toro [2009], Ch.2]. The generation mechanism described above is the *Doppler effect* [Hiermaier, 2008, Ch.4] and this critical speed is *the speed of sound* of the medium. It is a local property of the medium itself, related to the rate of the pressure's change due to the variation of density.

Mathematically, the appearance of shock waves is a feature of the nonlinear conservation equations. Their distinctive feature is that even when the start of the motion is perfectly continuous, shock discontinuities may later arise automatically. Yet, under other conditions, just the opposite may happen; initial discontinuities may be smoothed out [Courant and Friedrichs, 1948, Ch.1]. When the linear approximation of the equations is used —as in acoustics— and the speed of sound is taken as a constant, discontinuities do not arise automatically [Courant and Friedrichs, 1948, Ch.1]. Only initial discontinuities across a surface are preserved as discontinuities and propagate with the medium's speed of sound [Whitham, 1999, Ch.1]. The assumption of linear waves fails as the amplitude of the disturbances increases.

In the nonlinear regime, Courant and Friedrichs [1948], p.119, distinguish two types of discontinuities: *contact surfaces* and *shock fronts*. In recent literature, each of these terms is used interchangeably with *contact discontinuities* and *shock waves* respectively. For continuum mechanics —ruling out cavitation in fluids and damage in solids— across contact discontinuities the acceleration is equal, such that equality of stresses and equality of velocities hold.

A constant speed of sound is not always a relevant assumption, especially for the propagation of high-amplitude pressure waves, which affect the thermodynamical state of the medium. Therefore, the speed of sound becomes a variable, an effect which introduces yet another way of building shocks: *dispersion-driven shocks*. The mechanism is the following. The first high-amplitude pressure wave compresses the medium locally and thus incurs an increase of the medium's speed of sound. Consequently, the next pulse of pressure travels at higher speed and catches up with the previous initial pulse. The coalescence of these pulse-waves leads to the formation of a shock-wave Hiermaier [2008]. So that for the formation of a shock, the speed of the disturbance should not necessarily be higher than the nominal speed of sound.

For a historical review of the shock-wave theory, we refer to Salas [2006].

1.1.1 Conservation equations across discontinuities

Figure 1.1 depicts a discontinuity S of surface area A which moves only with velocity normal to the surface v_S and hence sweeps volume $|v_0 - v_S|\, A\, \mathrm{d}t$, within the infinitesimal time interval $\mathrm{d}t$. The discontinuity brings the medium from state 0 to state 1.

recognizable signal that is transferred from one part of the medium to another with a recognizable velocity of propagation".

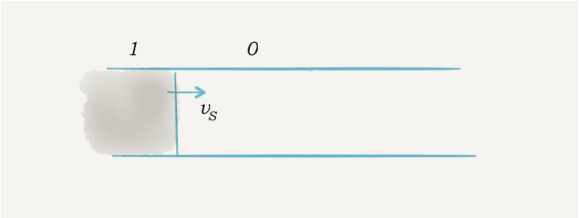

FIGURE 1.1: A propagating discontinuity S, bringing material from state 0 to state 1.

The three fundamental laws of conservation apply and all together, written for the states 0–1, compose the *Rankine-Hugoniot relations*:

$$\rho_0 \, (v_0 - v_S) = \rho_1 \, (v_1 - v_S), \tag{1.1}$$

$$\rho_0 \, (v_0 - v_S) \, v_0 + P_0 = \rho_1 \, (v_1 - v_S) \, v_1 + P_1, \tag{1.2}$$

$$\rho_0 \left(e_0 + \frac{1}{2} v_0^2 \right) (v_0 - v_S) + P_0 \, v_0 = \rho_1 \left(e_1 + \frac{1}{2} v_1^2 \right) (v_1 - v_S) + P_1 \, v_1. \tag{1.3}$$

Above and further on, subscripts refer to the different states of the medium, while ρ, P, v and e denote mass density, pressure, velocity and internal energy of the medium at the corresponding state. By transforming the equations to a system moving along with the shock —that is a shock-fixed coordinate system moving at v_S, the *jump conditions* are obtained [Hiermaier, 2008, Ch.4]:

$$\rho_0 \, v_0 = \rho_1 \, v_1 \equiv \dot{m}, \tag{1.4}$$

$$\rho_0 \, v_0^2 + P_0 = \rho_1 \, v_1^2 + P_1, \tag{1.5}$$

$$\frac{1}{2} v_0^2 + e_0 + \frac{P_0}{\rho_0} = \frac{1}{2} v_1^2 + e_1 + \frac{P_1}{\rho_1}. \tag{1.6}$$

All these relations hold across both shock and contact discontinuities. The latter can be distinguished by considering that the mass flux is zero ($\dot{m} = 0$). Consequently, across contact discontinuities pressures are in equilibrium ($P_0 = P_1$). This type of discontinuities move with the medium and separate two zones of different density and temperature, while pressure and velocity are the same on both sides. Moreover, contact discontinuities may also separate different media.

For a nonzero mass current ($\dot{m} \neq 0$), shock discontinuities are recovered from the relations above. By successive replacements of the first to the second and finally to the third, the *Hugoniot relation* is derived:

$$e_1 - e_0 = \frac{1}{2} (P_1 + P_0) \left(\frac{1}{\rho_0} - \frac{1}{\rho_1} \right), \tag{1.7}$$

which exclusively involves thermodynamic quantities. It is the locus of all admissible states upon a shock transition and it is a curve in the $P - 1/\rho - e$ space (Figure 1.2). This is a material-specific curve and includes all phases of the material —gaseous, liquid or solid. The shock transition, from state 0 to state 1, is assumed to be a straight

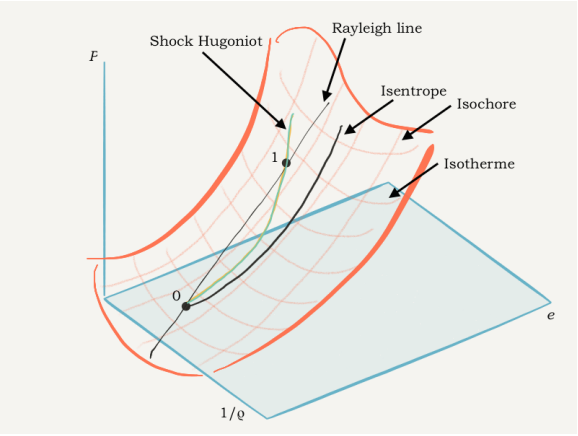

FIGURE 1.2: Thermodynamic paths in the $P - 1/\rho - e$ space.

line called *Rayleigh line* and it does not follow a line of consecutive states of thermodynamic equilibrium, as an isentrope would [Hiermaier, 2008, Ch.4]. Effectively, this means that shock transitions are irreversible processes and there are certain reasons for that.

In the investigation leading to the final relation, it is assumed that the only acting forces are due to pressure differences, while friction forces are ignored. This assumption is justified, provided that the gradients of velocity and temperature are small, for in regions of strong temperature and velocity variations irreversible thermodynamic processes occur [Courant and Friedrichs, 1948, Ch.3]. In these regions, the approximate description of flow in fluids with almost no viscosity and heat transfer by an idealized flow involving shock fronts, but no viscosity and heat conductivity, is necessarily inadequate. The examination of related phenomena shows that the regions of irreversible processes in gases are narrow zones, while outside of these transition zones the flow can be safely described as adiabatic and reversible. Thus the empirical facts suggest that the mathematical idealization of describing irreversible processes by sudden jump discontinuities, is valid. To put it as Courant and Friedrichs [1948], Ch.3: "...the assumption of sharp discontinuities is indeed an idealization which agrees with the facts rather better than we might hope". The thermodynamic condition expressing the irreversible character of the process is that the entropy does not decrease in the discontinuous process, so that $\rho_0 \, v_0' \, s_0 \leq \rho_1 \, v_1' \, s_1$, leads to the inequality for the *specific entropy*:

$$s_0 \leq s_1. \tag{1.8}$$

This entropy condition must be added to the conservation laws. Notice that for contact discontinuities, the conservation of energy and the entropy condition are automatically satisfied.

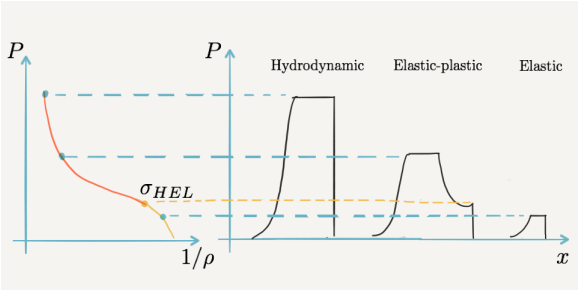

FIGURE 1.3: Wave configurations for different stress regimes and the Hydrodynamic Elastic Limit (HEL).

1.1.2 Shocks through solids

Hiermaier [2008], Ch.4, mentions Prandtl's attempt in 1906 to quantify the thickness of shock fronts in single-atom gases and Oertel's relation between the dimensions of the shock-front thickness and the mean free path λ_{fp} of the gas atoms ahead of the shock wave. In the latter study, thicknesses of $10\lambda_{fp}$ to $2\lambda_{fp}$ are reported for small to high shock Mach numbers respectively. These lead to typical shock-front dimensions of 1×10^{-7} m to 1×10^{-6} m in gases and consequently, replacing these waves as mathematical discontinuities is a reasonable approximation for macroscopic modeling [Toro, 2009, Ch.2].

Regarding metals, Hiermaier [2008], Ch.4, cites the work of Swegle and Grady, who found shock rise-times of 1×10^{-2} μs for pressure jumps across shocks of about 10 GPa —that is Mach ≈ 0.1 jump in Aluminum— and up to 1×10^{-1} μs for weaker shocks of around 2 GPa. Thus for metals, the material-dependent properties of shock-front dimensions are in the order of magnitude of 1×10^{-5} m to 1×10^{-4} m. A distinct characteristic of solids is that they can deal with relatively high stresses without changes in their speed of sound. In the diagram of pressure versus the specific volume ($P - 1/\rho$) of Figure 1.3, this is depicted in the low pressure region (yellow), where the increase of stresses can be approximated as linear, with respect to the specific volume. This behavior is encountered for loadings with stresses below the threshold value σ_{HEL}; the so-called *Hugoniot elastic limit*. In this *elastic* regime, the wave structure corresponds to an elastic wave transmitted into the medium.

For loadings exceeding σ_{HEL}, the speed of sound becomes a nonlinear function of volume. Above this critical value, the solid medium is unable to support shear stresses; plasticity kicks in. It should be mentioned that this limit is not a fixed material constant. It rather varies with the amplitude and the application time of the loading. As seen in Figure 1.3, the typical wave structure in this *elastic-plastic* regime, is an elastic precursor followed by a viscoplastic wave. Hiermaier [2008], Ch.4, mentions that the existence of this precursor wave has been disputed. Whether the elastic precursor is overtaken —and thus annihilated— by very fast plastic waves is only a matter of the load application speed and the achieved maximum pressure level [Hiermaier, 2008, Ch.4].

In the *hydrodynamic* regime the stresses applied to the medium can be considered as isotropic. Under these conditions, normal stresses dominate, being at least a scale of magnitude higher than the shear stresses [Asay and Shahinpoor, 1993, Ch.2]. For this reason, discussion is concentrated on pressure. Since the applied stress greatly exceeds the yield stress of a solid, its behavior can be approximated by that of a fluid because the fractional deviations from stress isotropy are small. Under these conditions, the solid is considered to be hydrodynamic and obtains a fluid-like behavior. On the other hand, material strength, plastic flow and polymorphic transformations are distinct features of solids in lower loading regimes and are not encountered in liquids. From a fundamental perspective, the deformation processes in solids are profoundly different from liquids, at least up to stresses of σ_{HEL}.

The state of the medium determines how easily shock waves occur. For gaseous media, a loading of 1×10^2 MPa —equal to a quarter of the yield strength of Aluminum— results to temperature increases of 1×10^4 K and large changes of the speed of sound. Consequently, gases are highly compressible and the propagation of shock waves is guaranteed in almost every case [Asay and Shahinpoor, 1993, Ch.1]. In order to create disturbances which travel at speeds higher than the speed of sound, or disturbances of amplitude high enough to trigger shock waves, rapid impulse-loading of solids is required. In practice, this is achieved by e.g. flyer-plate tests, detonation or during hypervelocity impacts. The latter are considered in the final chapter (Chapter 6), along with numerical investigations.

1.1.3 Equations of state

The system of Equations 1.4-1.6 includes nine variables. To solve the shock problem, given some information from the right hand side —such as any value of v_S, ρ_1, P_1, v_1 or e_1— an extra relation is necessary. To this end, relations of the form $P = P(\rho, e)$ or $v_S = v_S(v_1)$ are essential. These may arrive from experimental data and/or theoretical considerations. An example is the *equation of state*, which links the three thermodynamical quantities, P, ρ and e, and in specific a *caloric equation of state* [Hiermaier, 2008; Malvern, 1969]. The latter may lead to the creation of an equation of state, given some theoretical considerations and assumptions. Typically it is used for metals, where for c_0 the speed of sound at reference state 0 and ξ a parameter, the linear form $v_S = c_0 + \xi\, v_1$ is adopted, albeit nonlinear forms are advised for some metals [Kerley, 2006].

With the linear expression at hand, the conservation of mass in Equation 1.1 becomes:

$$v_S = \frac{c_0}{1 - \xi\eta}, \quad \eta = 1 - \frac{\rho_1}{\rho_0}, \tag{1.9}$$

so that the Rankine-Hugoniot relations transform into:

$$\rho_1 = \rho_0 \frac{c_0 + \xi v_1}{c_0 + v_1(\xi - 1)}, \tag{1.10}$$

$$P_1 = P_0 + \rho_0 c_0^2 \frac{\eta}{(1-\xi\eta)^2}, \tag{1.11}$$

$$e_1 = e_0 + \frac{\eta}{\rho_0} P_1 - \frac{\eta^2}{2} \frac{c_0^2}{(1-\xi\eta)^2}. \tag{1.12}$$

This approach provides the possibility of deriving a nonlinear equation of state capable of describing the thermodynamics of dynamic deformation processes in a material including shock wave formation and propagation. In some cases it is used indiscriminately as an equation of state, though it is certainly a wrong term.

Another option is to postulate an equation of state in the strict form $P = P(\rho, e)$, based on theoretical models and observations. The *barotropic* equation of state accounts for the changes of pressure due to variations away from the medium's reference density ρ_0, under a constant speed of sound c_0:

$$P(\rho) = \rho_0 c_0^2 \Big(\frac{\rho}{\rho_0} - 1 \Big). \tag{1.13}$$

On the contrary, the *ideal-gas* equation of state, formulates an absolute relation between pressure, internal energy and density:

$$P(\rho, e) = (\gamma - 1)\rho e, \tag{1.14}$$

where γ is the ratio of heat capacities of the gas. In order to accommodate liquids under extreme pressures, an extension of it exists; the *stiffened-gas* equation of state:

$$P(\rho, e) = (\gamma - 1)\rho e + \gamma P_{ref}, \tag{1.15}$$

for P_{ref} a liquid-specific reference high pressure.

In all previous cases, the speed of sound, that is the change of pressure with respect to density, is:

$$c = \sqrt{\frac{\mathrm{d}P}{\mathrm{d}\rho}\Big|_s}, \tag{1.16}$$

and involves both explicit and implicit terms, since in general $P = P(\rho, e)$.

The main idea behind the *Mie-Grüneisen* equation of state, is to split the pressure into a pressure due to a cold compression/expansion and a thermal contribution [[Hiermaier, 2008, Ch.4], Asay and Kerley [1987]], which results in:

$$P(\rho, e) = P_H - \Gamma\rho(e - e_H), \tag{1.17}$$

with P_H, e_H a Hugoniot reference state and $\Gamma = (\partial P/\partial e|_\rho)/\rho$. The Hugoniot data necessarily pertain to the Rankine-Hugoniot equations and thus, it is subtly implied that equilibrium conditions apply across a shock. Typically the relations derived before, upon the assumption of a linear shock-particle velocity, are used. The form used is:

$$P(\rho, e) = \Big(1 - \frac{1}{2}\Gamma\eta\Big) P_H(\rho) + \Gamma\rho(e - e_H), \quad P_H = a_0\eta. \tag{1.18}$$

In practice, especially under high-compression regimes, a reference to the cold curve $e = 0$ is used for the dependency on internal energy [Libersky et al., 1993; Wicklein et al., 2008].

Basically, the Mie-Grüneisen EOS is a first order approximation of the state surface in the neighborhood of the measured Hugoniot curve along an isochoric path. Another important limitation of this EOS is that phase changes are ruled out. Tillotson [1962] developed a branched equation of state, capable of incorporating the physics of phase changes of metals; it has been extended to model water [Brundage, 2013]. A further alternative is the use of a set of tabulated data such as SESAME, discussed in Hiermaier [2008], Ch.4.

1.1.4 Inhomogeneous media

In the case of multicomponent materials, shock waves will not propagate undisturbed through the specimen. The transition from one layer to its adjacent layer is not a smooth function in space; it shows up as a discontinuity in the density distribution and reflections and transmissions may occur, whenever a shock encounters a material interface [Davison, 2008, Ch.4]. Hence, the shock loading problem becomes a multiphase shock problem [Courant and Friedrichs, 1948, Ch.3].

Let us consider the medium, shown in the upper plot of Figure 1.4, where a shock S moving through material at reference state 0, brings it to state 1. Further upstream the shock, there is a contact discontinuity with material at state 2. The moment the shock arrives at the contact discontinuity, maximally two waves can be triggered: one taking material from state 1 to state 3 and another taking material from state 2 to state 4, as seen on the lower plot of Figure 1.4. Any of them can be a rarefaction or a shock, depending on the material parameters of the medium, the states 1 and 2, and the shock S.

The system of Equation 1.1, referring to the states 1-3, is written as:

$$\rho_1 v'_S = \rho_3 (v'_S - (v_3 - v_1)), \tag{1.19}$$

$$P_1 = \rho_3 (v'_S - (v_3 - v_1))(v_3 - v_1) + P_3, \tag{1.20}$$

considering a frame of reference moving along with the material at state 1; that is at v_1. Then, v'_S can be eliminated by substituting the first to the second:

$$\rho_3^2 \frac{(v_1 - v_3)^2}{\rho_1 - \rho_3} = \rho_3 (v_3 - v_1)^2 + P_1 - P_3. \tag{1.21}$$

By applying this across the (shock or contact) discontinuities 1-3 and 2-4, we obtain the system:

$$\rho_3^2 \frac{(v_3 - v_1)^2}{\rho_1 - \rho_3} + \rho_3 (v_3 - v_1)^2 = P_1 - P_3, \tag{1.22}$$

$$\rho_4^2 \frac{(v_4 - v_2)^2}{\rho_2 - \rho_4} + \rho_4 (v_4 - v_2)^2 = P_2 - P_4, \tag{1.23}$$

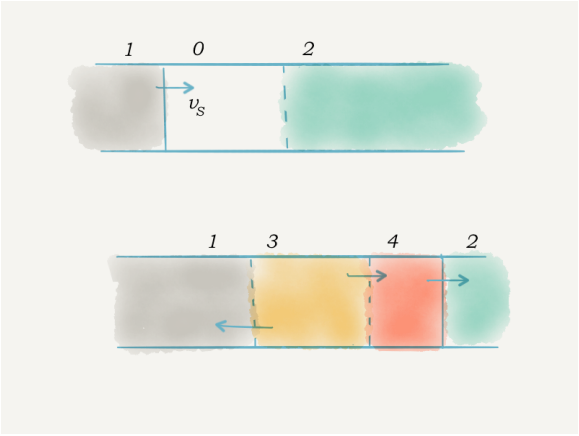

FIGURE 1.4: Wave configuration after the interaction of the shock wave S with the contact discontinuity between states 1-2.

$$e_3 + e_1 + \frac{1}{2}(v_3 - v_1)^2 = P_3\left(\frac{1}{\rho_1} - \frac{1}{\rho_3}\right), \tag{1.24}$$

$$e_4 + e_2 + \frac{1}{2}(v_4 - v_2)^2 = P_4\left(\frac{1}{\rho_2} - \frac{1}{\rho_4}\right). \tag{1.25}$$

Note that these are jump conditions and in case any of the waves is a rarefaction, they can only predict the emerging piecewise constant values of the variables. Additional analysis is required to reveal the region over which the rarefaction expands —the *fan region*.

The four equations above relate sixteen variables in total. Taking states 1 and 2 as initial data: $\rho_1, v_1, e_1, P_1, \rho_2, v_2, e_2, P_2$, become parameters and eight variables are left to be found via the four equations above. The functional relation:

$$P = P(\rho, e), \tag{1.26}$$

provides two additional equations. Moreover, the assumption of a continuous medium translates to equality of velocities and accelerations. Hence, also pressures are equal, thus providing two additional equations:

$$P_3 = P_4 \equiv P_* \quad \text{and} \quad v_3 = v_4 \equiv v_*. \tag{1.27}$$

Therefore, the nonlinear system of eight equations contains eight unknowns and, under certain assumptions, a numerical solution can be sought. In its simplest form, the system incorporates the barotropic equation (5.1), where $P = P(\rho)$, the energy equations become redundant and the system reduces to a quadratic polynomial of v_*.

1.2 Smoothed Particle Hydrodynamics

The articles of Gingold and Monaghan [1977] and Lucy [1977] sketched a novel solution strategy for astrophysical flows. The method aimed at offering an efficient

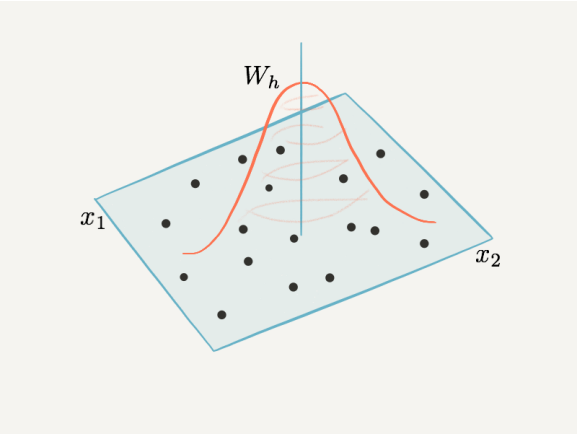

FIGURE 1.5: Typical form of functions used for the construction of the SPH density estimate in a two-dimensional problem domain.

treatment of open boundaries, which is a pronounced characteristic of astrophysical flows. Gingold and Monaghan [1977] coined the name Smoothed Particle Hydrodynamics (SPH) to the method, for the core of SPH is the discretization of media in a finite number of particles and the construction of a smoothed mass density via a convolution-based operation. An appropriately chosen, yet not problem dependent, (see discussion in Chapter 2)— parameter regulates the smoothing region and is called the *smoothing length*. Figure 1.5 shows a Gaussian-like smoothing function W_h, with h the smoothing length, which furnishes the SPH mass density for a finite particle number in a two-dimensional domain. Since SPH solves the equations of hydrodynamics, it falls in the vast category of *hydrocodes*; Zukas [2004] provides a comprehensive review of hydrocodes. SPH adopts the *Lagrangian description of the flow field*, a feature which results to perfect computation of advection and no extra effort for tracking interfaces. The latter two properties are fundamental in the applications SPH is called in for, and are reviewed by Monaghan [2012].

1.2.1 Development and applications

The first use of SPH in compressible flows appeared in Monaghan and Gingold [1983] and the breakthrough is the artificial viscosity term for the treatment of numerical instabilities related to the propagation of shocks. This term is based on the artificial viscosity of Von Neumann from 1948, which is a standard ingredient of hydrocodes. In a later study Monaghan [1997] constructed SPH artificial dissipation terms, viscosity and conductivity, which have a structure similar to the one of Riemann solvers. Similarly to the mesh-based methods, Riemann solvers have been proposed, simple [Parshikov and Medin, 2002] or more elegant [Inutsuka, 2002]. Artificial dissipation is still the favored option in a large body of SPH literature, due to its simplicity, generality and straightforward derivation. Puri and Ramachandran [2014] compare the two approaches and find them to deliver results of the same quality in the solution

of the Euler equations.

In problems of shock propagation, also termed as *fully compressible regime*, the length scales of the problem span over a wide range and some kind of adaptivity is necessary in SPH. Typically, this is achieved by varying the smoothing length[2]. A solution is to write an evolution equation for the smoothing length, which follows the density evolution, such that the mass within the volume of a particle remains constant. Hernquist [1993] examines the errors from such a choice and [Price, 2012] shows that the subsequent derivation of the motion equation is not straightforward. Nelson and Papaloizou [1994] first introduced a varying smoothing length in a way consistent with the equations; it involves a complicated strategy. Bonet and Rodriguez-Paz [2005]; Monaghan and Price [2001]; Springel and Hernquist [2002] show simple ways to involve the variation of the smoothing length in the SPH equations. The first study takes into account the variation of the smoothing length along with the variation of the density in deriving the equations of motion; the second uses Lagrangian multipliers as constraints for the volume of each particle, while the third uses a similar approach as the first, and it additionally couples adaptivity to improved density estimates near fixed boundaries.

The variation of the smoothing length is one kind of adaptivity. A second kind is to have the number of particles vary in time, so that sparsely populated regions of the domain are filled with particles and particles are removed from densely populated regions. To this end, particle splitting and merging algorithms are introduced. The splitting and merging of particles is not always momentum-conserving, let alone energy conserving. For that reason, special care needs to be taken. Vacondio et al. [2012] construct an algorithm for the shallow water equations —referring to isothermal conditions, where both the smoothing length and the number of particles vary. They show that the coupling of a varying smoothing length with particle splitting is not a straightforward task and it is questionable if it can be done in a consistent way, that is including the extra terms discussed in the previous paragraph.

In contrast to the fully compressible flows, those flows that can be described adequately by the weakly compressible regime —or the incompressible one— do not require an adaptive smoothing length. Since SPH solves the equations of hydrodynamics and is best suited to domains with open boundaries, it finds application in the computation of high-speed or high-momentum liquid flows involving free boundaries. The first paper on free surface water flow by Monaghan [1994] considers pressure coupled to density, which is assumed to vary at maximally 1% around its reference value.[3] To arrive at a trustworthy result, a viscosity model is required. It turns out that the artificial viscosity term can be easily tuned in a way that it models the Laplacian of the velocity field and thus shear stresses. This appears to be the standard SPH-way of modelling liquids. Other approaches appeared, as well. Cummins and Rudman [1999] introduced a projection method, where during the update of the velocity the restriction of zero velocity-divergence applies, which was later presented

[2] In early studies [Monaghan, 1997; Monaghan and Gingold, 1983], this task was avoided by simply taking smoothed initial data.

[3] Note that the concept of artificial compressibility, introduced by Chorin [1967], exists in other computational methods as well.

by Hu and Adams [2006] as *Incompressible SPH (ISPH)*.

SPH's Lagrangian description of the domain makes it unnecessary to track interfaces or different materials or fluids. From this point of view, SPH is an excellent candidate for *multiphase* computations. Unfortunately, the application is not as straightforward as it might seem. Monaghan [1995] experimented with multiphase computations and found out that the differential form of mass conservation works better, seconded by the scheme which in later chapters we refer to as the volume scheme and particles of mass ratio per phase equal to the ratio of the density. The paper of Colagrossi and Landrini [2003] advanced the understanding of multiphase SPH and insists on the same SPH scheme and mass arrangement. Hu and Adams [2006] promote the use of the number-density in order to build an expression for density and the same arrangement for mass. In yet another technique, Grenier et al. [2009] construct the density via evolving the determinant of the Jacobian of the medium's configuration in time; particle masses are again unequal per phase. Finally, Monaghan and Rafiee [2013] clearly show that the original scheme and mass configuration [Monaghan, 1995] is a simple and reliable way to model multiphase weakly compressible flows.

The extension of the weakly compressible multiphase schemes to the fully compressible regime is not a straightforward task. Ritchie and Thomas [2001] rearrange the conserved variables such that a smooth estimate of pressure is based on thermal energy and is used for the construction of the density estimate. The study of Hopkins [2013] generalizes this approach, obtaining particle volumes as functions of the internal energy density, rather than mass density. This approach can raise criticism, considering that internal energy is not a conserved quantity, whereas the total energy is. Last but not least, Agertz et al. [2007] argue that the fundamental differences between SPH and mesh-based methods, may drive SPH to suppress mixing of fluids. Price [2008] focuses on Kelvin-Helmholtz instabilities and shows that schemes coming from the standard SPH framework are adequate for multiphase computations by choosing artificial dissipation terms carefully. Thus, two questions rise. First, which of all schemes coming from the standard SPH framework (as described by Monaghan [2005]; Price [2012]) is the most suitable? Second, for fully compressible computations particles of equal masses are advised and typically used [Borve and Price, 2009; Price, 2012]; can particles of unequal masses deliver trustworthy results? Recent studies [Zisis et al., 2015a,b] and the tests of Chapter 5 are devoted to answering this question.

For solid dynamics, hydrodynamic codes become essential when rapid impulsive loading of materials results to the propagation of strong waves. On top of that, SPH's ability in dealing well with open boundaries, makes it a good candidate for the numerical simulation of *hypervelocity impacts*, that is impacts between objects at speeds higher than the speed of sound through the materials involved. With the normal stresses given by the standard SPH algorithm, the critical step is to construct the deviatoric stresses in terms of the particle values. This research was pioneered by Libersky et al. [1993] and resulted in the establishment of SPH as the state of the art methodology for the computational investigation of hypervelocity impacts. Chapter 6 is devoted to the discussion of hypervelocity impacts and the computation of various problems.

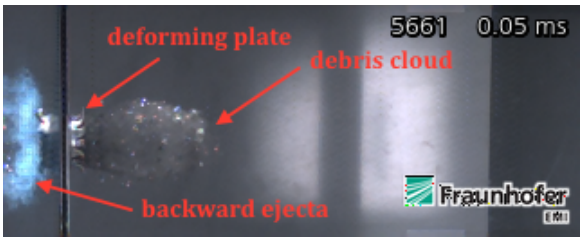

FIGURE 1.6: Experiment

1.2.2 SPH for hypervelocity impacts

Spacecraft in orbit run the risk to experience impacts from small-sized particles such as space debris and micrometeorites. They travel at typical velocities of 10 km/s relative to the spacecraft. Micron-sized particles degrade the spacecraft's shield protection. It is estimated that in the near Earth space, the affected surface area of brittle materials (e.g. solar panels and mirrors) is 0.01–0.001% per year of exposure, with the main impactors being of micrometer size Drolshagen [2008]. Millimeter- and centimeter-sized bodies can puncture vital components of the spacecraft or lead to its complete destruction Drolshagen [2008]. In order to conceive the damage potential of the latter bodies, consider that a centimeter-sized object speeding at 10 km/s, has similar kinetic energy as a car speeding at 40 km/h, only concentrated in a centimeter-sized volume!

Hypervelocity impact events are characterized by the projectile's relative velocity being in the range or higher than the speed of sound of the target material, which is about 6 km/s in Aluminum. Sharp density changes occur, propagated through the target as shock waves. The projectile's momentum is absorbed, visible by the fact that dynamic pressure is abruptly transformed into static pressure. Normal stress effects on an incremental element of the material dominate over the deviatoric stress effects and the hydrodynamic loading regime occurs [Asay and Kerley, 1987; Hiermaier, 2008]. Solid materials will effectively behave like fluids in this loading regime. Hypervelocity impacts are considered to be substantially different than ballistic impacts, where impact velocities are one order of magnitude lower.

Materials and configurations for spacecraft shields were considered by Whipple [1947], even before the first satellite was set in orbit around the Earth. Multicomponent materials are being used extensively [Christiansen et al., 1995].

In the case of multicomponent materials, shock waves will not propagate undisturbedly through the specimen. The transition from one layer to its adjacent layer is not a smooth function in space; it shows up as a discontinuity in the density distribution of the target and reflections and transmissions will occur, whenever a shock encounters a material interface [Davison, 2008, Ch.4]. Hence, the shock loading problem becomes a multiphase shock problem.

Figure 1.6 shows a snapshot of a hypervelocity impact experiment, 50 μs after impact. A spherical Aluminum projectile of diameter 5 mm, moving at 4.36 km/s from left

to right, impacts normally onto a laminated plate, 15 mm thick and made up of five successive Aluminum/epoxy resin layers. On the right of the plate, the transmitted material forms a debris cloud, which is a distinct characteristic of hypervelocity impacts. Depending on the impact parameters (mainly the impact speed), it is full of solid fragments, liquid droplets or even gaseous mixtures coming from sublimated solid material. At higher impact speeds, production of plasma is reported [Drolshagen, 2008]. Additionally, on the left there is a cloud of reflected material, while at the same time the plate is undergoing severe deformation. All these three processes involve continuously evolving surfaces, and their description poses a challenging problem for computational methods.

The appearance of shocks requires a hydrocode with the following features: 1) decomposition of the stress tensor into a hydrodynamic and a deviatoric part; 2) artificial viscosity or a Riemann solver, to treat the strong wave propagation problem [Hiermaier, 2008]. Regarding real viscous and heat-conduction effects, it is typically assumed that the process is much faster than the time necessary for those effects to appear. The exact conservation of mass, momentum and energy are crucial for the long-term stability of the simulation.

Although at the time of the pioneering article of Libersky et al. [1993], the exact conservation properties of SPH were still questionable, other major advantages of SPH are stated: *robustness, conceptual simplicity, ease of adding new physics, a natural treatment of void and the ability to handle high strains in a purely Lagrangian frame*. Due to these properties, they apply SPH to the hypervelocity impact of a Copper projectile onto an Aluminum plate, at 5.5 km/s and qualitatively validate the solver against the corresponding experiment. Moreover, the impact of an Iron cylinder onto a rigid wall at 221 m/s serves as an additional validation case. They use an evolution equation for the smoothing length, which follows the evolution of density. In order to choose the smoothing length factor —the number of particles per smoothing length— for the Cubic spline they run *Noh's implosion problem*, which involves an ideal gas and admits an analytical solution.

Various developments of their code and suggestions for future research are reported in Libersky et al. [1997]. There are two main features. First, the introduction of ghost particles which are created by mirroring the actual particles, so that the convergence of the solution strategy improves close to boundaries. Second, they introduce what they call *conservative smoothing*. Nonetheless, the arsenal which provides a variational derivation of SPH was not developed yet. The algorithm is variationally inconsistent and the conservative smoothing is not similar to the Riemann-like dissipative terms (Monaghan [1997]) of concurrent SPH algorithms.

Johnson [1996] develops an axisymmetric SPH and a three-dimensional SPH algorithm to study high-velocity impacts, which he couples to Finite Elements (FE). It seems to be the first effort towards a coupled strategy. Dyka and Ingel [1995] introduce a second set of points —in addition to the particles— for the calculation of stresses, in an effort to cancel tensile instability. However, this method is difficult to apply in complex arbitrary geometries.

The trust in SPH for the simulation of hypervelocity impacts is augmented by Hiermaier et al. [1997], who undertake a combined experimental-computational campaign. They use an axisymmetric SPH algorithm to simulate the projectile-target impacts of Aluminum-Aluminum, Aluminum-Copper and Aluminum-Lead at velocities of about 6 km/s. In the meantime, the foundations for a Lagrangian derivation of SPH were laid by Nelson and Papaloizou [1994]. The latter work is cited in Hiermaier et al. [1997], when the variation terms related to the smoothing length are disregarded as computationally expensive to calculate. They arrive at an algorithm which produces large variations of 5% in energy conservation. Additionally, they employ the scheme of Libersky et al. [1993], which is variationally inconsistent. It is now known [Bonet and Lok, 1999; Colagrossi and Landrini, 2003] that variational inconsistency of weakly compressible SPH schemes may inflict noisy results. Regarding fully compressible SPH schemes, in Chapter 5 we provide evidence that not all choices of variationally consistent schemes are wise when the smoothing length is a variable.

Hayhurst et al. [1998] report the introduction of SPH to the AUTODYN package, which until today (integrated to the ANSYS workbench package) is a leading commercial package for SPH. That same code is used by Hiermaier and Schafer [1999] to publish numerical-experimental results regarding hypervelocity impacts into pressurized vessels. Air, Aluminum and Titanium are treated in the same computational domain.

Parshikov and Medin [2002] drop the artificial viscosity and construct a Riemann-solver based on the acoustic approximation. They apply it to the simulation of impacts at moderate impact speeds of below 1 km/s. Effectively, it is also a contact algorithm. A comparative study is performed by Mehra and Chaturvedi [2006], who consider four different shock capturing schemes used in SPH. Their performance in simulating moderately high-velocity impacts (at 3 km/s) and hypervelocity impacts (at 6 km/s) is examined. They find that the contact algorithm of Parshikov and Medin [2002] is best suited to impacts of moderately high-velocity (3 km/s), since it does not suffer from nonphysical fracture and particle-clumping. Regarding hypervelocity impacts, algorithms based on artificial dissipation seem to be more suitable, notwithstanding an overestimation of the resulting crater diameter on the target (by 12–16% in Al–Al impact). Eventually, they note that the overestimation of the crater size in hypervelocity impact could be attributed to excessive artificial viscosity, which enhances transverse momentum transfer. Finally, they also found that the choice of alternative equations of state does not significantly change the results.

In a different context, the study of Vignjevic et al. [2005] compares SPH, Discrete Elements and Erosive Finite Elements. They obtain good agreement for all methods, in terms of target damage with the available experimental results. The element-erosion method shows problems in following the correct deformation pattern as a large number of elements are deleted. The other two methods describe failure patterns with more ease, although tensile instability appears in SPH and a better definition of the node linkage failure criterion is required for the Discrete Elements Method.

In an effort to remedy the instabilities of SPH, Shintate and Sekine [2004] extend the traditional algorithm by introducing a particle merger/generation technique and they

study high-velocity impact scenarios. Especially for the moderately high-velocity impacts, results are promising. Nonetheless, in a later work, Vacondio et al. [2012] warn that it is not a straightforward task to render accurate schemes or momentum conserving schemes from the traditional framework, when particle adaptivity is applied.

In the literature, there exist two methods which are conceptually similar to SPH for hypervelocity impacts. First, Fahrenthold and Koo [2001] employ a rather complicated framework, which resembles SPH and is derived from variational principles. The benefit is that it is consistent to thermodynamics, while at the same time it makes it possible to capture small deformations. Second, Li et al. [2010] construct the Optimal Transportation Meshfree method, which incorporates concepts from the theory of optimal transportation, with meshfree interpolation and material point sampling (which effectively is the previously mentioned stress-points [Dyka and Ingel, 1995]). Notwithstanding the formal mathematical basis, the resulting scheme is practically the same as the SPH schemes with the integral mass conservation and artificial viscosity. They apply the method to high-velocity impacts.

Substantial effort was made to simulate hypervelocity impacts onto multicomponent structures with SPH. Homogenized materials were introduced, with the averaged properties of their components as material properties. The homogenization approach became popular in the community of hypervelocity impacts and was equipped with a rigorous procedure of producing averaged versions of anisotropic materials [Clegg et al., 1999; Riedel et al., 2006; Wicklein et al., 2008]. Nevertheless, two major drawbacks are apparent in this approach: the homogenization process is based on assumptions coming from quasi-static loading regimes, and the effects of shock reflection-transmission are neglected. Following a different approach, the Modified-SPH method is introduced [Zhang and Batra, 2007] to solve an elastic wave propagation problem through a functionally graded material. The properties of such a material are smooth functions in space. Therefore, without any discontinuities in the properties of the material it is impossible for any transmission-reflection pattern to occur.

Zhou et al. [2007] introduce the Adaptive SPH methodology of Owen et al. [1998] in the field of high velocity impacts. This methodology consists of creating a tensorial smoothing length, so that the smoothing kernel becomes ellipsoidal. It is advantageous because it is able to adjust to the asymmetries of the strains per direction, which are observed during an impact. On the other hand, Price [2012] explains that this choice is impossible to deliver variationally consistent schemes.

Zisis et al. [2013] present multiphase fully compressible SPH schemes to treat hypervelocity impacts into inhomogeneous materials, focusing on a basic isothermal impact test. The key ingredient is an artificial mass-flux term —which acts as an approximate acoustic Riemann solver— and suppresses the instabilities occurring on the interface of two different materials. Later [Zisis et al., 2014b], the algorithm is employed to study impacts into materials which involve large- and small-scale inhomogeneities. The former correspond to laminate plates and the latter to random inhomgeneities.

Liu et al. [2013] apply SPH to the hypervelocity impacts of laminated plates, without any special treatment to suppress the shock-induced instabilities on the interface of different materials. Zhang et al. [2015] employ a transport velocity algorithm for moderately high-velocity impacts at 3 km/s. This approach is susceptible of corrupting the conservation properties of the scheme, since it is not variationally consistent. Finally, Zisis et al. [2016b] show the differences in the deformation patterns occurring during hypervelocity impacts of monolithic plates, laminated plates and simple homogenized models of laminated plates.

Finally, it seems relevant to clearly state the merits leading to the choice of SPH as the appropriate computational method for hypervelocity impacts. First and foremost, these are its conservation properties, which allow for the long term stability of the solution. Second, its simplicity of adding physics and last, but not least the natural treatment of free boundaries, multibody interactions and discontinuous flows. As a downside, one should consider the reduced accuracy and the related —as we show in a later chapter— appearance of tensile instability.

1.2.3 Derivation

The central idea of the SPH method is to set up a relation between the continuum and a particle system, in which the continuum is loosely considered to be the limit case in which the number of particles tends to infinity. Two comments are necessary to raise any ambiguities. First, the term *particle* should not be interpreted as a physical object of any scale, like an atom, molecule or grain, but rather as a numerical entity attributed with mass, position, velocity and other properties of the medium it represents. Second, the loose link between the continuum and the resulting particle system, is by no means an *ad hoc* connection.

There exist two generally accepted ways to derive the SPH equations of continuum mechanics. The first way starts by constructing convolution-based discrete approximations of the differential operators which appear in the equations of mass, momentum and energy conservation [Liu and Liu, 2003; Violeau, 2012]. Thus, a plethora of differential operators becomes available, without a straightforward way of choosing which operator best mimics the conservation equations. It turns out that one has to choose a less accurate approximation for the momentum equation in order to derive a conservative scheme. The second way of introducing SPH is indeed a consistent way, since it employs *the principle of least action* applied to a particle system. Then, the SPH density estimator, being a weighted sum of the system's particle masses, is introduced as a constraint to the equation of motion. Nelson and Papaloizou [1994] are credited with the first derivation in this way and are followed by Bonet and Lok [1999], Monaghan and Price [2001] and Springel and Hernquist [2002]. The importance of the variational structure of the system is already mentioned in the article of Gingold and Monaghan. [1978]. In later literature [Monaghan and Gingold, 1983; Monaghan and Lattanzio, 1985] the derivation of SPH schemes by constructing discrete approximations of differential operators is promoted.

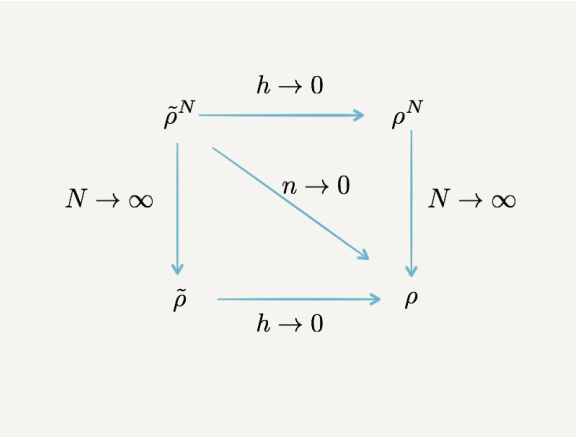

FIGURE 1.7: The convergence of the SPH density to the density of continuum mechanics.

Regarding the derivation of SPH from the Lagrangian of a particle system, a subtlety lies in the fact that in the derivation of the SPH equations from the particle system, the action of the particle system is minimized rather than the action of the continuum. The minimization of the action at the continuum level and the subsequent discretization of the motion equation in terms of particles do not necessarily yield the same equation of motion (at the discrete level). The latter procedure also reveals the mathematical formalities necessary to convince oneself that SPH indeed comes from principles of continuum mechanics.

DiLisio et al. [1998] are the first to cognize the significance of a measure-valued formulation for SPH, since it allows the study of both the particle system, and the limiting continuum setting in a single context. Nonetheless, they prove the convergence of an SPH-like scheme, rather than the one actually used in the practice of SPH. Their work has been extended by Evers et al. [2015], who first derive the classic SPH scheme in a systematic manner and then prove its convergence as the number of particles grows to infinity. Following the pioneering work of DiLisio et al. [1998], they adopt the *Wasserstein distance* in the space of probability measures, to study convergence. Effectively, it is a way to assign a cost function to any admissible configuration of the system and thus one can obtain an upper bound which is a necessary ingredient to prove convergence. Additionally, they show numerical evidence of the theoretical findings. In any case, smoothing the density practically means that the original problem is deliberately turned into a regularized/smoothed one, which is afterwards solved by means of an SPH scheme. Hence, by choosing SPH as the solution method one is automatically bound to studying a different problem than the original one, already at the continuum level. In the diagram of Figure 1.7, four different density functions appear and the ways they converge to each other, either as the number of particles $N \to \infty$, either as the smoothing length $h \to 0$ or as both previous occur via $n = n(N \to \infty, h \to 0) \to 0$. Thus, three questions naturally arise:

- Does the solution of the smoothed problem converge to the solution of the

original problem of classical continuum mechanics, $\tilde{\rho} \to \rho$ as $h \to 0$?

- Does the particle solution of the smoothed problem converge to the solution of the smoothed continuum problem, $\tilde{\rho}^N \to \tilde{\rho}$ as $N \to \infty$?
- Does the particle solution of the smoothed problem converge to the solution of the original problem of continuum mechanics, $\tilde{\rho}^N \to \tilde{\rho}^N$ as $n \to 0$?

The present study shows how the concepts of measure-valued evolutions can advance our understanding for these questions.

CHAPTER 2

Constructing smooth estimates

The strong asset of SPH is that it can treat transforming and discontinuous domains with relative ease, compared to other numerical methods [Monaghan, 2005]. Fundamental to this is the convolution-based operation which is applied on a function and delivers a smoothed version of it. However, the integral operation requires a good partitioning of the domain, which is far from being the case in the discontinuous domains in which SPH gives good results.

In order to provide a straightforward framework for this challenge, we formulate the smoothing operation in the context of *measure-valued evolutions*. This formulation is inspired by two studies [DiLisio et al., 1998; Evers et al., 2015], which provide mathematically rigorous proofs of convergence for the classical SPH scheme applied in hydrodynamics. The present chapter aims at bridging the gap between the aforementioned studies and the current SPH literature. In order to do so, we first discuss the importance of formulating the SPH estimates in terms of measures when the problem domain undergoes a transformation. Second, we show how the various SPH estimates fit in this framework and at the same time we underline the difference between approximating invariants of the system and any other, variant quantity. Finally, we introduce the differential operators which are used in deriving the SPH equations of motion in the following chapter.

2.1 Smoothing in a fixed domain

The term *mollifier* is coined by Friedrichs [1944] to the linear integral operator which provides the smooth approximation:

$$\tilde{f}(x) = \int_{\mathbb{R}^d} f(y)\, W_h(x-y)\, \mathrm{d}\lambda(y), \quad x, y \in \mathbb{R}^d, \quad h \in (0, \infty), \tag{2.1}$$

for the function $f : \mathbb{R}^d \to \mathbb{R}$ and h a —still to be defined— parameter of the smooth function $W_h : \mathbb{R}^d \to \mathbb{R}$. Here, for reasons which are discussed further on, it is written with the help of λ, the *Lebesgue measure*. In this way [Evans, 1998, App.C], the notion of derivative is extended to the *weak derivative*:

$$\partial_\alpha \tilde{f}(x) = \int_{\mathbb{R}^d} f(y)\, \partial_\alpha W_h(x-y)\, \mathrm{d}\lambda(y), \tag{2.2}$$

adopting an index notation α, β, γ for the spatial dimensions. In the related literature, the above operation serves as the basis for *the theory of distributions* which applies to all locally integrable functions f [Schwartz, 1969, Ch.1].

The usefulness of this *smoothing* or *regularization* or *mollification* operation[1] is twofold. First, it allows to construct approximations of the differential operators which appear in differential equations; thus making the equations possibly easier to analyze or solve, especially numerically. Second, in case discontinuous functions or point-wise data (given a discretization of the domain) are treated, the operation transforms the problem into a problem with corresponding smooth data, while providing a concrete framework under which the solutions of the smoothed problem converge to those of the original one.

Note that in the literature the smooth function W_h is found under various names, such as *kernel*, *test function*, *smoothing function*, or even *mollifier*, although Friedrichs [1944] reserves the latter for the integral operator. In our discussion we use the term commonly used in the SPH-literature, namely *smoothing function*, while the integral operation is termed *smoothing*.

2.1.1 Smoothing functions

The class of radially symmetric smoothing functions can be written in the form:

$$W_h(x) = \frac{c_d}{h^d}\, w(q), \qquad q := \frac{\|x\|}{h}, \qquad c_d^{-1} := \int_{\mathbb{R}^d} w\, \mathrm{d}\lambda, \tag{2.3}$$

[1] Although the term smoothing is primarily used in this work —adhering to the common SPH terminology, we consider these three terms to be equivalent.

with $\|\cdot\|$ the *Euclidean distance*. The prototype of such functions, as presented by Evans [1998], App.C, is the *standard mollifier*[2]:

$$w(q) = \begin{cases} \exp\left(\frac{1}{q^2-1}\right), & q < 1, \\ 0, & q \geq 1, \end{cases} \tag{2.4}$$

with $c_d \approx [2.2523, 4.826, 5.08]$ for $d = [1, 2, 3]$, the parameter which guarantees the standard mollifier's scaling to unity[3]. Properties tantamount to the convergence of $\tilde{f}$ to f as $h \to 0$ in Equation 2.1 are [Evans, 1998, App.C]:

1. infinite smoothness, $W_h \in C^\infty$;
2. compact support, $W_h(\|x\| > \vartheta h) = 0$, for some fixed $\vartheta \in \mathbb{R}_{>0}$;
3. scaling to unity, $\int_{\mathbb{R}^d} W_h \, \mathrm{d}\lambda = 1$;
4. convergence, $W_{h\to 0}(x) = \delta(x)$;
5. radial symmetry, $W_h(x) = W_h(\|x\|)$.

The latter property implies that the mollifier's gradient:

$$\partial_\alpha W_h(x) = \frac{c_d}{h^{d+1}} \begin{cases} \frac{x_\alpha}{q} \frac{\mathrm{d}w(q)}{\mathrm{d}q}, & q > 0; \\ 0, & q = 0, \end{cases} \tag{2.5}$$

is antisymmetric, since $\partial_\alpha W_h(-x) = -\partial_\alpha W_h(\|x\|)$. This is a property frequently used in the SPH literature and in Chapter 3.

The defining properties of the standard mollifier are broad enough to accommodate a vast variety of functions which can be used in the solution of numerical problems. On the other hand, apart from studying the problem in terms of mathematical analysis, its numerical solution appears in the discrete setting. This may allow for weakening some of the aforementioned five properties. For example, the scaled *Gaussian function*:

$$w(q) = \exp[-(3q)^2], \tag{2.6}$$

for $c_d = [3/\sqrt{\pi}, 3/\pi, 3/(\pi\sqrt{\pi})]$ in $d = [1, 2, 3]$ defies the second property, as it is not compactly supported. In order to establish a common radius for all functions under study, $q \in [0, 1]$ is considered as an indicative "support radius" for the Gaussian. After all, its truncated version is an attractive option, since values for $q > 1$ are close to zero with acceptable numerical accuracy [4]. In contrast to the Gaussian, functions of finite

[2] It frequently appears under the name *bump function*, as well.

[3] Without an analytical expression available for the integral, the values are obtained numerically, with the accuracy decreasing for increasing dimensionality.

[4] The integral operator of Equation 2.1 with the Gaussian is frequently termed *Weierstrass transform*.

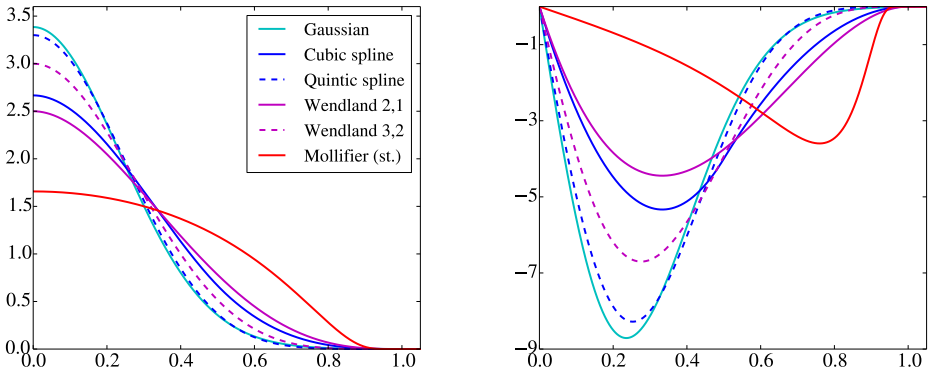

FIGURE 2.1: Kernels (*left*) and their gradients (*right*) in a common support radius and scaled to unity.

differentiability challenge the property of infinite smoothness, however they turn out to be amenable. Examples of the latter are the *Schoenberg kernels* and the *Wendland kernels*, which enjoy popularity in practice [Dehnen and Aly, 2012; Monaghan, 2005; Price, 2012].

The family of Schoenberg kernels is widely known as *B-splines* and they are piece-wise polynomials of finite differentiability [Price, 2012]. The *cubic spline* is the $M4$ kernel:

$$w(q) = (1-q)_+^3 - 4(1/2-q)_+^3, \tag{2.7}$$

used with $c_d = [8/3, 80/(7\pi), 16/\pi]$. Note that the introduced notation should read $(\cdot)_+ = \max\{0, (\cdot)\}$. Splines with polynomials of higher degrees approach the Gaussian, and the *quintic spline* is the $M6$ kernel:

$$w(q) = (1-q)_+^5 - 6(2/3-q)_+^5 + 15(1/3-q)_+^5, \tag{2.8}$$

for $c_d = [3^5/40, 3^7 7/(478\pi), 3^7/(40\pi)]$, which offers a good approximation to the Gaussian. A drawback, which can be serious (see discussion following 2.11), is that their *Fourier transforms* in $d > 1$ are not positive definite [Dehnen and Aly, 2012].

This property is the cornerstone of the family of the Wendland kernels, which by construction have positive definite Fourier transforms for all d. Examples are the $C2$ kernel:

$$w(q) = (1-q)_+^{\tau_{1d}}(1 + \tau_{1d}\, q), \tag{2.9}$$

with $\tau_{1d} = [3, 4, 4]$ and $c_d = [5/4, 7/\pi, 21/(2\pi)]$ and the smoother $C6$ kernel:

$$w(q) = (1-q)_+^{\tau_{1d}}(1 + \tau_{1d}\, q + \tau_{2d}\, q^2), \tag{2.10}$$

with $\tau_{1d} = [5, 6, 6]$, $\tau_{2d} = [8, 35/3, 35/3]$ and $c_d = [3/2, 9/\pi, 495/(32\pi)]$, mentioned in Dehnen and Aly [2012]. Figure 2.1 shows the kernels which are discussed above, along with their gradients.

2.1.2 Fourier transform of the smoothing function

Typically, f is the estimate of mass density, which is pursued in SPH. On physical grounds it must be positive. This is guaranteed for $W_h(x-y) \geq 0, \forall\, x, y \in \mathbb{R}^d$, whence in the discrete system a *positive definite* function w is required. A function $w : \mathbb{R} \to \mathbb{C}$ is called positive definite, if the matrix $[w(x_i - x_j)]_{i,j=1}^N$ is positive definite for all N, no matter the choice of x_i's Stewart [1976]. Thus, it is necessary, but not sufficient, that $w(0) \geq 0$ and $|w(x)| \geq w(0)$, which is indeed the case for all w functions presented before.

An important result [Stewart, 1976] is that if w is positive definite, then, taking $\int_{\mathbb{R}^d} w(x)\,\mathrm{d}p(x) = \int_{\mathbb{R}^d} w(x)\,\mathrm{d}x/(2\pi)^{d/2}$, its *Fourier transform* [Rudin [1987], Ch.9, Evans [1998], Ch.4]:

$$\mathcal{F}\{w\}(\zeta) = \int_{\mathbb{R}^d} w(x)\, e^{-\mathrm{i}\zeta x}\mathrm{d}p(x), \quad \zeta \in \mathbb{R}^d, \quad \mathrm{i}^2 := -1, \tag{2.11}$$

is non-negative, provided that it exists. Conversely, if w satisfies the Fourier inversion:

$$\mathcal{F}^{-1}\{w\}(x) = \int_{\mathbb{R}^d} \mathcal{F}\{w\}(\zeta)\, e^{\mathrm{i}\zeta x}\mathrm{d}p(\zeta) = \int_{\mathbb{R}^d}\int_{\mathbb{R}^d} w(y)\, e^{\mathrm{i}\zeta(x-y)}\mathrm{d}\zeta\,\mathrm{d}p(y), \tag{2.12}$$

and $\mathcal{F}^{-1}\{w\} \geq 0, \forall x$, then w is a positive definite function [Stewart, 1976]. The latter remark imposes another demand on w, and by extension on W_h. Hence, in addition to the previous five properties, a W_h with:

6. non-negative inverse Fourier transform, $\mathcal{F}^{-1}(W_h) \geq 0$,

is required. It should be mentioned that given the radial symmetry of the w functions, the Fourier transform in $d > 1$ coincides with the *Hankel transform*, which can provide significant simplification in the calculations.

2.1.3 Scaling the smoothing functions

The kernels above (also see Figure 2.1) are written with a support radius $q = 1$, although they can be expanded or contracted to different radii as $q \to \vartheta q$. This transformation leaves the functional form w unchanged [Dehnen and Aly, 2012] and thus, given a W_h, the smoothing length obtains a different meaning for each kernel. Up to this point, the parameter h is only understood as $h \to 0$.

Various ways are proposed in order to define a relation $h = h(W_h)$ [Dehnen and Aly, 2012]:

- the distance $\|r^*\|$ of the kernel's inflection point, $r^* : |\partial_\alpha W_h(r^*)| = \max\Big(\partial_\alpha W_h(x)\Big)$;
- the ratio $W_h(r^*)/|\partial_\alpha W_h(r^*)|$;

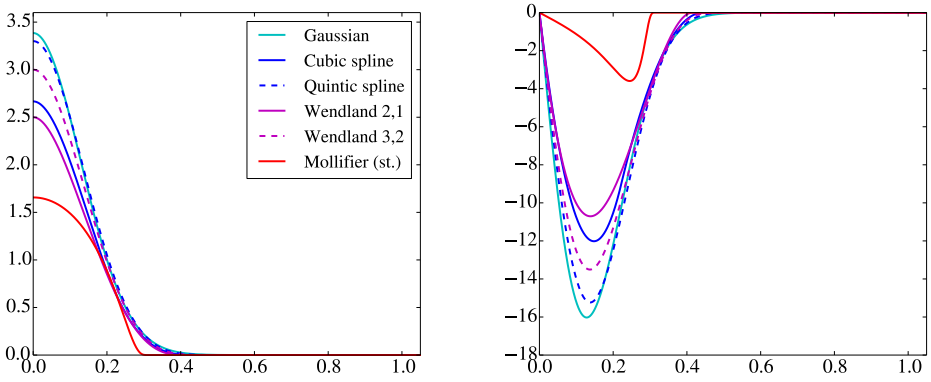

FIGURE 2.2: Kernels (*left*) and their gradients (*right*) in the appropriate σ-based support radius.

- the kernel's standard deviation, $\sigma^2 = \int_{\mathbb{R}^d} x^2 \, W_h(x) \mathrm{d}\lambda$,

with the latter offering an implicit definition. Indeed, all these definitions coincide for the Gaussian [Dehnen and Aly, 2012]. More importantly, σ^2 is the second moment of the kernel and the first which has a different value for each functional form w. Notice that the zeroth moment of W_h is the scaling to unity and the first is nullified due to the antisymmetry of the kernel's gradient. Additionally, it turns out that σ is directly related to the numerical resolution of waves and that is why it is usually preferred to set $h = 2\sigma$, for every kernel [Dehnen and Aly, 2012].

However, we can show that σ also has a different meaning for each kernel (the derivation requires the change of the coordinate system to a radially symmetric one), according to:

$$\sigma^2 = \int_{\mathbb{R}^d} x^2 \, W_h \, \mathrm{d}\lambda = c_d \, h^2 \, \sigma_w^2, \quad \sigma_w^2 := c_d \, h^2 \int_{\mathbb{R}^d} w \, \mathrm{d}\lambda. \tag{2.13}$$

Hence, we conclude that the relation of the smoothing length to the kernel's standard deviation differs for the various functional forms w. Consequently, in order to have the same resolution (governed by σ) for any chosen kernel, the smoothing length:

$$h^2 = c_d \Big(\frac{\sigma}{\sigma_w} \Big)^2, \tag{2.14}$$

becomes a certain kernel-specific quantity. It offers a way to achieve the same resolution with different kernels. Thus, by no means is it an explicit definition of the smoothing length. Figure 2.2 shows the kernels which are discussed above, along with their gradients, in the support radius which is defined according to σ.

2.1.4 Resolution of the discretized system

Consider the partitioning of Ω as: $\Omega^N = \{\bigcup_{i=1}^{N} \Omega_i = \Omega : \Omega_i \bigcap \Omega_{j\neq i} = \varnothing, \forall i, j \in [1, N]\}$, $N \in \mathbb{N}^+$, and the points $x_i \in \Omega_i$ in each subdomain. The function:

$$\tilde{f}^N(x) = \sum_{j=1}^{N} f(x_j)\, W_h(x - x_j)\, \lambda(\Omega_j), \tag{2.15}$$

converges to $\tilde{f}$ of Equation 2.1 as $N \to \infty$, for a space filling distribution. The latter implies that as $N \to \infty$, a condition such as $\max_j \|x_i - x_j\| \to 0, \forall x_j \in \Omega_i$, is necessary to obtain a reasonable partitioning. A stronger requirement would be to assume $\max_i \lambda(\partial\Omega_i) \to 0$, for $\partial\Omega_i$ denoting the boundary of Ω_i. Certain constructions respect the former requirement and they are discussed in Section 3.1.1. Note that the superscript N is used to distinguish a quantity in the discrete setting from the corresponding quantity in the continuous setting.

The $h = h(W_h)$ relation tells something about the behavior of h, however, it provides no link whatsoever with the discrete system to be solved. In a review article, Monaghan and Lattanzio [1985] state a simple rule and the following puts this rule in the context of measures, thus providing a more formal understanding of the resolution of the discretized SPH system.

The total number of integration points is given by the *counting measure* [Cheng, 2008; Rudin, 1987, Ch.2]:

$$\nu(\Omega^N) = \begin{cases} \text{elements of } \Omega^N, & \text{if } \Omega^N \neq \Omega, \\ \infty, & \text{if } \Omega^N = \Omega, \end{cases} \tag{2.16}$$

which can be written as the sequence:

$$\nu = \sum_{i=1}^{N} \delta_{x_i}. \tag{2.17}$$

In the discrete case, it obtains the *number* or *point density*:

$$n(x_i) = \frac{\int_{\Omega_i} \mathrm{d}\nu}{\int_{\Omega_i} \mathrm{d}\lambda} = \frac{1}{\int_{\Omega_i} \mathrm{d}\lambda}, \tag{2.18}$$

which is a local property at the smallest scale of the numerical system. There exists a larger scale in the system, corresponding to a region $\Omega_{h,i} = \{x : \|x - x_i\| \leq \vartheta h\}$. Therefore, the number density can be approximated as:

$$n(x_i) = \frac{\nu(\Omega_i)}{\lambda(\Omega_i)} \approx \frac{\nu(\Omega_{h,i})}{\lambda(\Omega_{h,i})} = \frac{a_d(\vartheta\eta)^d}{a_d\,(\vartheta h)^d} = \left(\frac{\eta}{h}\right)^d = \overline{n}(x_i), \tag{2.19}$$

with η the number of points per ϑ units of support radius and $a_d = [1, \pi, 4\pi/3]$ constant, depending on the dimensionality of the problem. For the above we underline

that $\overline{n} \to n$ for $h \to 0$, because $\Omega_i^{h \to 0} = \Omega_i$, as the h-neighborhood collapses towards a point. Notice that in any case for a regular distribution of points $n(x_i) = \overline{n}(x_i)$ holds. Therefore, the previous relation offers a definition for the smoothing length, as:

$$h(n) := \eta \, n^{-1/d}, \tag{2.20}$$

especially since the number density —or an estimate of it— is available given the configuration of points.

It is worth pondering how does the dependence $h = h(W_h)$ —described by Equation 2.14— pop up within the last definition of h. To this end, consider the scaling property of the kernel:

$$1 \approx \sum_j W_{h,ij} \lambda(\Omega_j) = \sum_j W_{h,ij} \frac{1}{n(x_j)} \approx \sum_j W_{h,ij} \frac{h^d}{\eta^d} = \frac{c_d}{\eta^d} \sum_j w_{ij}, \qquad \forall \, j : \|x_i - x_j\| < \vartheta h, \tag{2.21}$$

where the second approximation is in case the configuration of integration points is not regular and the condition involving h is due to the fact that the summation of w-values emanates from a summation of W_h-values. Hence:

$$\eta \approx \left(c_d \sum_j w_{ij} \right)^{1/d} \sim \vartheta \Big(c_d \, a_d \, \max(w_{ij}) \Big)^{1/d}, \quad \forall \, j : \|x_i - x_j\| < \vartheta h, \tag{2.22}$$

depends on: 1) the functional form w, via its values and the scaling factor c_d, and on 2) how large the compact support of the kernel is, in ϑ units of h. The last (crude) approximation is performed by considering a block function of value $\max(w_{ij})$. Finally, note that η becomes independent of the problem's dimensions only for kernels with c_d being a power of the dimensions, like the Gaussian function. Therefore, Equation 2.20 is a fundamental link between the resolution of the continuous and the discretized domains.

2.2 Smoothing in a transforming domain

The smoothing in the previous section is performed in a fixed domain and therefore the domain's partitioning can be chosen to be regular. Let us now assume that the domain Ω is the transformation —via a deterministic or probabilistic process— of an original domain Ω_0. The points $x = x(x_0)$ of Ω are in one-to-one correspondence with points x_0 of Ω_0. A regular partitioning of the original domain Ω_0, as the upper left plot in Figure 2.3, does not necessarily end up to a regular distribution pattern of the discretization points in Ω, see e.g. the upper right graph in Figure2.3. Consequently, there is an aporia of how to calculate the associated volumes in order to employ Equation 2.1.

Starting from the partitioning of Ω_0 as: $\Omega_0^N = \{ \bigcup_{i=1}^N \Omega_{0,i} = \Omega_0 \, : \, \Omega_{0,i} \bigcap \Omega_{0,j \neq i} = \varnothing, \forall i, j \in [1, N] \}$, for $x_{0,i} \in \Omega_{0,i}$, and along with the above mentioned condition

for a space filling distribution, there are various ways to obtain the volumes $\lambda(\Omega_i)$ in the transformed domain Ω^N. The crudest approach is to assume equally sized subdomains $\lambda(\Omega_i) = \lambda(\Omega_{0,i}) = \sum_j \lambda(\Omega_{0,j})/N$. This concept characterizes integration in a *Monte-Carlo* way. Another approach is to deploy a fixed background Cartesian grid of $A \supseteq \Omega$ with $A_{j\in\{1,M\}}$ subdomains and count the $\nu(A_j)$ particles, such that $\lambda(\Omega_i) = \lambda(A_j)/\nu(A_j)$, for all $\Omega_i \in A_j$. This approach is depicted in the lower left plot of Fig.2.3 and forms the basis of the *Particle In Cell* method. Alternatively, it is always a possibility to perform a *Voronoi tesselation* in the transformed domain Ω and thus obtain $\lambda(\Omega_i)$, as in the lower right plot of Fig.2.3.

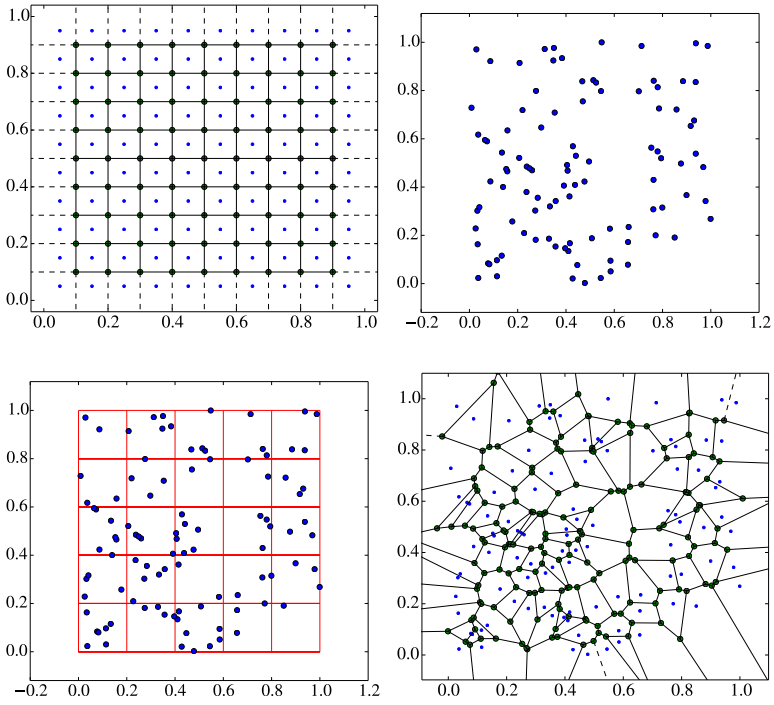

FIGURE 2.3: The initial and the transformed domain (*upper plots*), and two ways to obtain a partitioning of the transformed domain (*lower plots*).

2.2.1 Invariant quantities

A different concept is to formulate the problem in terms of the system's inherent invariants, if any. Suppose that φ is an invariant quantity. Then, we describe it by the measure:

$$\varphi(\Omega) = \int_{\Omega} \mathrm{d}\varphi(x) = \int_{\Omega_0} \mathrm{d}\varphi_0(x_0) = \varphi_0(\Omega_0), \tag{2.23}$$

and its smoothing leads to its smoothed density (e.g. see the treatment of mass in Evers et al. [2015]):

$$\tilde{f}(x) = \int_{\Omega} W(x-y)\,\mathrm{d}\varphi(y). \tag{2.24}$$

The above equality is guaranteed by the one-to-one correspondence[5] between the points of Ω_0 and Ω. Moreover, the integration over the two domains:

$$\int_{\Omega} g(x)\,\mathrm{d}\varphi(x) = \int_{\Omega_0} g(x_0)\,\mathrm{d}\varphi(x_0), \tag{2.25}$$

is equivalent for any bounded function g.

Considering that φ is absolutely continuous with respect to the Lebesgue measure and thus, the *Radon-Nikodym derivative* of the measure φ with respect to the Lebesgue measure, provides a well-defined density:

$$f(x) = \frac{\mathrm{d}\varphi}{\mathrm{d}\lambda}\Big|_{(x)}. \tag{2.26}$$

According to the latter, Equation 2.24 transmutes to Equation 2.1 and thus allows for the calculation of $\tilde{f}$ without prior knowledge of f. A well-defined f_0 is typically available in Ω_0 and the calculation of $\tilde{f}$ can be performed in the following steps:

- Partition Ω_0 into Ω_0^N and assign points $x_{0,i} \in \Omega_{0,i}$;
- Introduce the discrete measure $\varphi_0^N = \sum_i p(x_i)\delta_{x_{0,i}}$, where $p(x_i) := \int_{\Omega_{0,i}} f_0\,\mathrm{d}\lambda$;
- Obtain $\tilde{f}^N$ in the transformed domain, as: $\tilde{f}^N(x) = \sum_j p(x_j)\,W_j(x)$.

Regarding SPH schemes, this is precisely the ingredient which allows for the relatively easy treatment of discontinuous flows, with φ the measure of mass and $\tilde{f}$ the smoothed density of mass. Moreover, this effect endows SPH with the property of exact conservation of mass. On the other hand, this is the reason why in order to study SPH schemes, a measure-based formulation is necessary.

For systems lacking inherent invariant quantities, the total number of the discretized system's points offers an alternative.With $N \to \infty$, each $\Omega_{0,i}$ collapses into the point $x_{0,i}$ and the continuous domain is recovered as $(\mathbb{R}^d)^N \supset \Omega_0^N \to \Omega_0 \subset \mathbb{R}^d$. Thus, the total number of integration points within Ω_0^N, given by $\nu_0 = \sum_i \delta_{x_{0,i}}$, is a conserved quantity as:

$$\nu(\Omega^N) = \sum_i \delta_{x_i} = \sum_i \delta_{x_{0,i}} = \nu_0(\Omega_0^N). \tag{2.27}$$

The smoothed number density:

$$\tilde{n}(x_i) = \int_{\Omega^N} W(x_i - y)\mathrm{d}\nu(y) = \sum_j W(x_i - x_j), \tag{2.28}$$

[5]The rigorous procedure goes through the definition of the *pushforward operation* and is described in [Evers et al., 2015].

is explicitly computable for the discrete system, as well as the per-particle density of the conserved quantity φ:

$$p(x_i) = \frac{\int_{\Omega_i} \mathrm{d}\varphi}{\int_{\Omega_i} \mathrm{d}\nu} = \int_{\Omega_i} \mathrm{d}\varphi. \tag{2.29}$$

Eventually, f is approached as the limit:

$$\lim_{N\to\infty} \tilde{f}^N(x_i) = \lim_{N\to\infty} p(x_i)\,\tilde{n}(x_i) = \lim_{N\to\infty} \frac{\int_{\Omega_i} \mathrm{d}\varphi}{\int_{\Omega_i} \mathrm{d}\lambda} = \left.\frac{\mathrm{d}\varphi}{\mathrm{d}\lambda}\right|_{(x)} = f(x), \tag{2.30}$$

with the conservation of $p(x_i) = \int_{\Omega_i} \mathrm{d}\varphi = \int_{\Omega_{0,i}} \mathrm{d}\varphi_0$. Accordingly, given f_0 in Ω_0, the calculation of $\tilde{f}^N$ can be performed in the following steps:

- Partition Ω_0 into Ω_0^N and assign points $x_{0,i} \in \Omega_{0,i}$;
- Introduce the discrete measures $\varphi_0^N = \sum_i p(x_i)\,\delta_{x_{0,i}}$ and $\nu = \sum_i \delta_{x_{0,i}}$, where $p(x_i) \equiv \int_{\Omega_{0,i}} f_0 \,\mathrm{d}\lambda$;
- Obtain $\tilde{f}^N$ in the transformed domain, as: $\tilde{f}^N(x_i) = p(x_i)\,\sum_j W_j(x_i)$.

Finally, for domains which are discretized in a uniform pattern, Equation 2.19 shows that $h(\overline{n}) = \eta\,\overline{n}^{-1/d}$. In case of a large span of n in the transformed domain, a better estimate can be achieved by considering h to vary with the number density[6]. Therefore, we resort to $\tilde{n}$, which is a readily available estimate of n, and postulate:

$$\tilde{f}^N(x_i) = p(x_i)\,\tilde{n}(x_i), \qquad h(\tilde{n}(x_i)) = \eta\,\tilde{n}(x_i)^{-1/d}, \tag{2.31}$$

which is a system of simultaneous equations.

2.2.2 Variant quantities

In contrast to the procedure above, which applies to invariant quantities, the smoothed estimate of any variant quantity of the system necessitates the definition of a volume. Inhibiting the use of a meshing procedure, the construction of a volume can be accomplished in two ways. In case there exists an invariant φ in the system, with regularized density $\tilde{f}$, then volume increments are obtained as $\mathrm{d}\lambda \approx \mathrm{d}\varphi/\tilde{f}$, thus arriving at:

$$\tilde{g}(x) = \int_\Omega g(y)\,W(x-y)\,\mathrm{d}\lambda(y) \approx \int_\Omega g(y)\,W(x-y)\,\left.\frac{\mathrm{d}\varphi}{\tilde{f}}\right|_{(y)}, \tag{2.32}$$

which is clearly only an approximation. By introducing the discrete measure φ^N, the sum:

$$\tilde{g}^N(x) = \sum_j g(x_j)\,W(x-x_j)\,\frac{\varphi^N(\Omega_j)}{\tilde{f}_j^N}, \tag{2.33}$$

[6] In literature of SPH, this is a usual approach [Monaghan, 2005], yet only a few studies underline the significance of number density (e.g. [Price, 2012]).

converges to the integral as $N \to \infty$. Alternatively, if no inherent invariants exist we resort to the construction of an increment for the discrete measure of volume via the number density, as $\lambda(\Omega_j) = \nu(\Omega_j)/n(x_j)$. The smoothed estimate becomes:

$$\tilde{g}^N(x) = \sum_j g(x_j) W(x - x_j) \lambda(\Omega_j) \approx \sum_j g(x_j) W(x - x_j) \frac{1}{\tilde{n}(x_j)}. \tag{2.34}$$

Similarly to the construction of smoothed estimates for invariant quantities in domains with a non-uniform discretization, the estimate for variant quantities becomes:

$$\tilde{g}^N(x_i) = \sum_j g(x_j) W_j(x_i, h(x_i)) \frac{1}{\tilde{n}(x_j)}, \quad h(x_i) = \eta\, \tilde{n}(x_i)^{-1/d}, \tag{2.35}$$

which is again a system of coupled equations.

2.3 Smoothing operators

Having constructed the smoothed invariant quantity and its derivative:

$$\tilde{f}(x) = \int_\Omega W(x - y)\, \mathrm{d}\varphi(y), \quad \partial_\alpha \tilde{f}(x) = \int_\Omega \partial_\alpha W(x - y)\, \mathrm{d}\varphi(y), \tag{2.36}$$

we now proceed to the definition of other operators that are used in the following chapters. Note that we suppress the explicit reference to h, so that $W \equiv W_h$. The transformation of the original domain Ω_0 into Ω implies a *variation* of the smoothing integral operator with respect to a change in the coordinates by δx. The integral appearing in $\tilde{f}$ above varies as:

$$\delta \tilde{f}(x) = \int_\Omega \partial_\alpha W(x - y) \Big(\delta x_\alpha - \delta y_\alpha \Big) \mathrm{d}\varphi(y). \tag{2.37}$$

Last but not least, since the transformation begins from the original configuration Ω_0 of the system, it is necessary to define the weak derivative with respect to that configuration as well. The smoothing applied to the measure φ and the corresponding weak derivative are:

$$\hat{f}_0(x_0) = \int_{\Omega_0} \hat{W}(x_0 - y_0)\, \mathrm{d}\varphi_0(y_0), \qquad \partial_{0\alpha} \hat{f}_0(x_0) = \int_{\Omega_0} \partial_{0\alpha} \hat{W}(x_0 - y_0)\, \mathrm{d}\varphi_0(y_0). \tag{2.38}$$

Note that $\hat{W} \equiv \hat{W}_{\hat{h}}$ is not necessarily the same as $W \equiv W_h$. Also, $\hat{h}$ does not equal h in general. Obviously, the variation in this case is:

$$\delta \hat{f}_0(x_0) = 0. \tag{2.39}$$

Regarding the smoothing operators for a variant quantity, its estimate and the corresponding derivative are:

$$\tilde{g}(x) = \int_\Omega g(y)\, W(x - y)\, \frac{\mathrm{d}\varphi}{\tilde{f}}\Big|_{(y)}, \qquad \partial_\alpha \tilde{g}(x) = \int_\Omega g(y)\, \partial_\alpha W(x - y)\, \frac{\mathrm{d}\varphi}{\tilde{f}}\Big|_{(y)}. \tag{2.40}$$

For a variation of the spatial coordinates, all the terms of the functional need to be taken into account:

$$\delta\tilde{g}(x) = \int_\Omega \delta g(y) W(x-y) \frac{\mathrm{d}\varphi}{\tilde{f}}\Big|_{(y)} + \int_\Omega g(y) \partial_\alpha W(x-y) \Big(\delta x_\alpha - \delta y_\alpha\Big) \frac{\mathrm{d}\varphi}{\tilde{f}}\Big|_{(y)} - \int_\Omega g(y) W(x-y) \frac{\delta\tilde{f}}{\tilde{f}^2}\Big|_{(y)} \mathrm{d}\varphi(y). \tag{2.41}$$

Interestingly, in case g coincides with $\tilde{f}$, then the first term is an approximation of $\delta\tilde{f} = \partial\tilde{f}/\partial x_\alpha \, \delta x_\alpha$ and the third term is its opposite, leaving only the second term. This effect forms the basis for a density estimate in the following chapter.

The smoothed estimate of a function with respect to the original coordinates is:

$$\hat{g}(x) = \int_{\Omega_0} g(y) \, \partial_\alpha \hat{W}_{\hat{h}}(x_0 - y_0) \, \mathrm{d}\lambda(y_0), \qquad \partial_{0\alpha}\hat{g}(x) = \int_{\Omega_0} g(y) \, \partial_\alpha \hat{W}_{\hat{h}}(x_0 - y_0) \, \mathrm{d}\lambda(y_0), \tag{2.42}$$

while it can be improved by using the analysis of Section 2.4. Equation 2.42 is used in the following sections. Note that in contrast to the density of the conserved quantity, this estimate depends on the particle trajectories. Consequently, $\hat{g}$ varies as:

$$\delta\hat{g}(x) = \int_{\Omega_0} \partial_\alpha g(y) \, \delta y_\alpha \, \hat{W}_{\hat{h}}(x_0 - y_0) \, \mathrm{d}\lambda(y_0). \tag{2.43}$$

and we underline that $\mathrm{d}\lambda(y_0)$ typically arrives from a partitioning of the original domain Ω_0 and thus it is known.

2.4 Convergence of smooth estimates

Until now, we constructed $\tilde{f}$ —the estimate of the density of a conserved quantity in a transforming domain— without using f and the estimate $\tilde{g}$ under the least assumption that g is locally integrable. In order to study the convergence of these estimates, to f and g respectively, the latter two should at least be piecewise continuous functions.

From an SPH point of view, we follow the concepts also presented in Monaghan [2005], Price [2012] and Macia et al. [2012]. Nevertheless, we highlight the distinction between the regularized density $\tilde{f}$ and the density $f = \mathrm{d}\varphi/\mathrm{d}\lambda$. This allows us to trace a nonlinearity which is typically shunned in most SPH error analyses. We note the scalings:

$$W_h = \mathcal{O}(1), \quad \partial_\alpha W_h = \mathcal{O}(h^{-1}), \quad \text{and} \quad (x-y)^\theta = \mathcal{O}(h^\theta). \tag{2.44}$$

2.4.1 Invariant quantities

In the regions of the domain Ω where f is smooth enough, the *Taylor expansion*:

$$\begin{aligned}\tilde{f}(x) &= \int_\Omega W(x-y)\,\mathrm{d}\varphi(y) = \int_\Omega f(y)\,W(x-y)\,\mathrm{d}\lambda(y)\\ &= f(x)\,H(x) + \partial_\alpha f(x)\,\Theta_\alpha(x) + \partial_{\alpha\beta} f(x) I_{\alpha\beta}(x) + \mathcal{O}(h^3),\end{aligned} \tag{2.45}$$

reveals the convergence $\tilde{f}$ to f, for the functionals:

$$\begin{aligned}&H(x) \equiv \int_\Omega W(x-y)\,\mathrm{d}\lambda(y), \quad \Theta_\beta(x) \equiv \int_\Omega (y_\alpha - x_\alpha)\,W(x-y)\,\mathrm{d}\lambda(y),\\ &I_{\alpha\beta}(x) \equiv \frac{1}{2}\int_\Omega (y_\alpha - x_\alpha)(y_\beta - x_\beta)\,W(x-y)\,\mathrm{d}\lambda(y).\end{aligned} \tag{2.46}$$

Due to the scaling of W to unity, in unbounded domains $H(x) = 1$. Additionally, W is symmetric, whence for the same domains $\Theta_\alpha(x) = 0$ and $I_{\alpha\beta}(x) \neq 0$. Therefore, we deduce that in the general case of unbounded or bounded continuous domains:

$$\tilde{f} = f + \mathcal{O}(h^\kappa), \qquad 0 \leq \kappa \leq 2. \tag{2.47}$$

Similarly, for the weak derivative we obtain:

$$\begin{aligned}\partial_\alpha \tilde{f}(x) &= \int_\Omega \partial_\alpha W(x-y)\,\mathrm{d}\varphi(y) = \int_\Omega f(y)\,\partial_\alpha W(x-y)\,\mathrm{d}\lambda(y)\\ &= f(x)\,K_\alpha(x) + \partial_\beta f(x)\,\Lambda_{\alpha\beta}(x) + \partial_{\beta\gamma} f(x) M_{\alpha\beta\gamma}(x) + \mathcal{O}(h^2),\end{aligned} \tag{2.48}$$

for the functionals:

$$\begin{aligned}&K_\alpha(x) \equiv \int_\Omega \partial_\alpha W(x-y)\,\mathrm{d}\lambda(y), \quad \Lambda_{\alpha\beta}(x) \equiv \int_\Omega (y_\beta - x_\beta)\partial_\alpha W(x-y)\,\mathrm{d}\lambda(y),\\ &M_{\alpha\beta\gamma}(x) \equiv \frac{1}{2}\int_\Omega (y_\beta - x_\beta)(y_\gamma - x_\gamma)\,\partial_\alpha W(x-y)\,\mathrm{d}\lambda(y).\end{aligned} \tag{2.49}$$

Since $\partial_\alpha W$ is antisymmetric, $K_\alpha = 0$ in unbounded domains. Moreover, $\Lambda_{\alpha\beta} = \delta_{\alpha\beta}$, for $\delta_{\alpha\beta}$ the *Kronecker delta*, and $M_{\alpha\beta\gamma} = 0$. Thus, the result is:

$$\partial_\alpha \tilde{f} = \partial_\alpha f + \mathcal{O}(h^\xi), \qquad -1 \leq \xi \leq 2, \tag{2.50}$$

for the general case of unbounded or bounded continuous domains.

It is necessary to stress that the observed possible divergence only appears for partitionings which are away from being reasonable, or on the boundaries of the domain. Regarding bounded domains, we discuss certain fixes in the next subsection. About problematic partitionings, we will see how these inefficiencies manifest themselves in instabilities during the dynamical evolution of the SPH system (see Section 3.4). Fixing them is not a straightforward task, as then the dynamics of the system itself is affected.

2.4.2 Variant quantities

For regions of Ω where g is analytical, the Taylor expansion of its smoothed estimate is:

$$\tilde{g}(x) = \int_\Omega g(y)\, W(x-y)\, \frac{\mathrm{d}\varphi}{\tilde{f}}\Big|_{(y)} = g(x)\, \tilde{H}(x) + \partial_\alpha g(x)\, \tilde{\Theta}_\alpha(x) + \mathcal{O}(h^2), \tag{2.51}$$

for the functionals:

$$\begin{aligned}
\tilde{H}(x) &\equiv \int_\Omega W(x-y)\, \frac{\mathrm{d}\varphi}{\tilde{f}}\Big|_{(y)} = \int_\Omega W(x-y)\, \frac{f\,\mathrm{d}\lambda}{\tilde{f}}\Big|_{(y)}, \\
\tilde{\Theta}_\alpha(x) &\equiv \int_\Omega (y_\alpha - x_\alpha)\, W(x-y)\, \frac{\mathrm{d}\varphi}{\tilde{f}}\Big|_{(y)} = \int_\Omega (y_\alpha - x_\alpha)\, W(x-y)\, \frac{f\,\mathrm{d}\lambda}{\tilde{f}}\Big|_{(y)}.
\end{aligned} \tag{2.52}$$

According to Equation 2.47, for nonzero $\tilde{f}$, $f/\tilde{f} = [1+\mathcal{O}(h^\kappa)]^{-1}$, $0 \le \kappa \le 2$. Considering the *binomial series*[7], we may write up to first order:

$$\tilde{H} = H\Big(1 - h^\kappa\Big), \qquad \tilde{\Theta}_\beta = \Theta_\beta\Big(1 - h^\kappa\Big). \tag{2.53}$$

Thus, the leading error term is the error of $H = \mathcal{O}(1)$ and we establish that:

$$\tilde{g} = g + \mathcal{O}(h^\kappa), \quad 0 \le \kappa \le 2. \tag{2.54}$$

An improvement to the estimate appearing in Equation 2.51 is to consider:

$$\frac{\tilde{g}(x)}{\tilde{H}(x)} = \frac{1}{\tilde{H}(x)} \int_\Omega W(x-y) \frac{\mathrm{d}\varphi}{\tilde{f}}\Big|_{(y)}, \tag{2.55}$$

an operation which is known as the *Shepard correction* [Macia et al., 2012]. Consequently, the convergence is:

$$\frac{\tilde{g}}{\tilde{H}} = g + \mathcal{O}(h^\kappa), \quad 1 \le \kappa \le 2. \tag{2.56}$$

Note that $H = \mathcal{O}(1)$, so that divergence problems related to the division by a positive power of h do not arise[8].

Regarding the weak derivative of g, it converges as:

$$\partial_\alpha \tilde{g}(x) = \int_\Omega g(y)\, \partial_\alpha W(x-y)\, \frac{\mathrm{d}\varphi}{\tilde{f}}\Big|_{(y)} = g(x)\tilde{K}_\alpha(x) + \partial_\beta g(x)\tilde{\Lambda}_{\alpha\beta}(x) + \mathcal{O}(h^2), \tag{2.57}$$

with the functionals:

$$\tilde{K}_\alpha(x) = \int_\Omega \partial_\alpha W(x-y)\, \frac{\mathrm{d}\varphi}{\tilde{f}}\Big|_{(y)}, \quad \tilde{\Lambda}_{\alpha\beta}(x) = \int_\Omega (x_\beta - y_\beta)\partial_\alpha W(x-y)\, \frac{\mathrm{d}\varphi}{\tilde{f}}\Big|_{(y)}. \tag{2.58}$$

[7] The binomial series $(1+z)^\theta = 1 + \theta z + ...$, converges for $|z| < 1$.

[8] Actually, such problems occur in the discrete setting, for points away from any other; then the discrete estimate of H tends to 0 and the calculation blows up.

Again by employing the binomial series and keeping first order terms, we find that:

$$\tilde{K}_\alpha = K_\alpha\Big(1 - h^\kappa\Big), \quad \tilde{\Lambda}_{\alpha\beta} = \Lambda_{\alpha\beta}\Big(1 - h^\kappa\Big). \tag{2.59}$$

and the approximation becomes:

$$\partial_\alpha \tilde{g} = \partial_\alpha g + \mathcal{O}(h^\xi), \qquad 0 \leq \xi \leq 2. \tag{2.60}$$

In order to guarantee convergence, Equation 2.57 can be turned into:

$$g(x)\,\tilde{K}_\alpha(x) - \partial_\alpha \tilde{g}(x) = \int_\Omega \Big(g(y) - g(x)\Big)\partial_\alpha W(x-y)\,\frac{\mathrm{d}\varphi}{\tilde{f}}\Big|_{(y)}. \tag{2.61}$$

The subtraction definitely removes the terms $\mathcal{O}(1)$ and delivers the convergence result for bounded or unbounded domains:

$$g(x)\,\tilde{K}_\alpha - \partial_\alpha \tilde{g} = \partial_\alpha g + \mathcal{O}(h^\xi), \quad 1 \leq \xi \leq 2, \tag{2.62}$$

since $\tilde{\Lambda}_{\alpha\beta} = \Lambda_{\alpha\beta}\Big(1 - h^\kappa\Big)$ and $\Lambda_{\alpha\beta} = \mathcal{O}(\delta_{\alpha\beta} + h)$. Finally, Equation 2.57 suggests that convergence of $\xi = 2$ can be achieved by inverting the tensor $\tilde{\Lambda}_{\alpha\beta}$ in the expression:

$$\partial_\beta g(x)\tilde{\Lambda}_{\alpha\beta}(x) = \int_\Omega \Big(g(y) - g(x)\Big)\partial_\alpha W\,\frac{\mathrm{d}\varphi}{\tilde{f}}\Big|_{(y)}. \tag{2.63}$$

This operation can be problematic though. Notice that for $\alpha \neq \beta$, $\mathcal{O}(h)$ terms are introduced in the approximation, due to $\tilde{\Lambda}_{\alpha\beta} = \mathcal{O}(\delta_{\alpha\beta} + h)$.

Apart from the constructions presented so far, there is a plethora of improved smoothed estimates that can be constructed for functions or their derivatives. An extensive review is given by Price [2012] and Violeau [2012]. We delineate the most popular and those that are used for the analysis of the smoothed equations of mechanics, as becomes apparent in Section 3.4.

Effectively, the convergence of the estimates and their derivatives to the corresponding functions depends on the values of the functionals $\tilde{H}$, $\tilde{\Theta}_\alpha$, $\tilde{K}_\alpha$ and $\tilde{\Lambda}_{\alpha\beta}$. Although the previous analysis related them to H, Θ_α, K_α and $\Lambda_{\alpha\beta}$ and in turn to the proximity of a point to the boundaries, in discretized domains their behavior is strictly connected to the configuration of the moving points.

Finally, it is crucial to underline that the conservation of the quantity φ is independent of the convergence of $\tilde{f}$ to f. The latter convergence plays an important role in the convergence of smoothed estimates of the variant quantity g.

CHAPTER 3

The SPH equations from continuum mechanics

In the literature of SPH, it is established that the classical SPH scheme can be derived by applying the principle of least action to a particle system, where the SPH density estimate acts as a constraint [Bonet and Lok, 1999; Monaghan, 2005; Monaghan and Price, 2001; Price, 2012]. The importance of the particle system's Lagrangian function is already recognized in early articles about SPH (e.g. Gingold and Monaghan. [1978]). A subtlety lies in the fact that in the derivation of the SPH equations the action of the particle system is minimized rather than the action of the continuum. The minimization of the action at the continuum level and the subsequent discretization of the motion equation in terms of particles do not necessarily yield the same equation of motion (at the discrete level). The latter procedure also reveals the mathematical formalities necessary to convince oneself that SPH indeed comes from principles of continuum mechanics.

For this reason, we follow a somewhat different path. We start by considering a general framework for the derivation of the equations of mechanics for continuous media. The indicated framework consists of the following triptych: *measure-valued evolutions*, *the principle of least action* and *the fundamental relation of thermodynamics*. Thereupon, we delve into the derivation of two types of equations: the *classical* equations and the *smoothed* ones. This distinction is understood in the following sense: while the classical equations designate a functional relation of density with local distortions, the smoothed equations adopt a smoothed density profile, which is eventually an explicit function of the medium's configuration. Three different smoothings are constructed based on three basic measures: the *measure of mass*, which upon scaling with the total mass of the medium is a probability measure, the *counting*

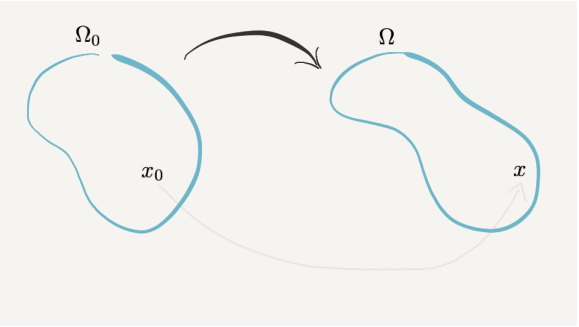

FIGURE 3.1: Transformation of a medium from Ω_0 to Ω.

measure and the *Lebesgue measure*. All three offer a formal way to pass to the discretized SPH equations. We finally conclude with remarks and suggestions for the use of the developed schemes.

3.1 General concepts

Classical mechanics defines a *particle* as a moving point of mass. Continuum mechanics is based on the notion of a particle in order to introduce the *continuous medium* as a mechanical system consisting of an infinite number of particles [Berdichevsky, 2009, Ch.3]. In the latter case, particles are definitely not physical entities of any scale. The infinite set of particles $\Omega_t \subset \mathbb{R}^d$, which constitute the medium at any time $t \in [0, T)$, is in one-to-one correspondence with a set of points of some region $\Omega_0 \subset \mathbb{R}^d$. Particles are tagged with their coordinates $x_0 \in \Omega_0$ and in this way the *material* or *Lagrangian coordinates* are defined [Berdichevsky, 2009, Ch.3]. The *particle trajectories* are the functions:

$$x = x(x_0, t), \qquad x \in \Omega_t, \tag{3.1}$$

which describe the *Eulerian coordinates* of the particles in the observer's frame of reference. Although curvilinear coordinate systems can be used, in what follows we avoid complications by assuming a single fixed *Cartesian frame* as the observer's frame of reference. Regarding the reference configuration, this may be any of the configurations attained by the medium during its motion. In case Ω_0 coincides with the initial configuration, then the description is called *total Lagrangian*. Alternatively, if the current configuration Ω_t is chosen as the reference, then the problem obtains an *updated Lagrangian* description. In order to keep the notation concise, we suppress the explicit dependence of Ω_t on t and simply write $\Omega \equiv \Omega_t$. The transformation of the medium from Ω_0 to Ω is depicted in Figure 3.1, where every point x of the new configuration corresponds to one point in the initial configuration.

Using an index notation for the spatial dimensions, the particle trajectories (3.1) appear as:

$$x_\alpha = x_\alpha(x_0, t), \qquad \alpha \in \{1, 2, 3\}, \tag{3.2}$$

or also $\beta, \gamma \in \{1,2,3\}$ further on. The summation convention applies wherever repeated indices are encountered. Accordingly, the Lagrangian coordinates in index notation become $x_{0\alpha}$ and they are fixed in time. Thus, the time derivatives of the trajectories provide the particle velocities:

$$v_\alpha(x(x_0,t),t) = \frac{\mathrm{d}x_\alpha}{\mathrm{d}t}\Big|_{(x_0,t)}, \tag{3.3}$$

with $\mathrm{d}(\cdot)/\mathrm{d}t$ denoting the *total* or *material derivative*. Note the difference in the temporal derivatives. In general, any real-valued function $f = f(x(x_0,t),t)$ of the Eulerian coordinates and time, obtains the total derivative:

$$\frac{\mathrm{d}f}{\mathrm{d}t} = \frac{\mathrm{d}f(x(x_0,t),t)}{\mathrm{d}t} = \partial_t f + \partial_\alpha f \frac{\mathrm{d}x_\alpha}{\mathrm{d}t} = \partial_t f + v_\alpha\, \partial_\alpha f, \tag{3.4}$$

where $\partial_t(\cdot)$ is the variation in time for the observer's frame and $\partial_\alpha(\cdot)$ are the spatial derivatives with respect to Eulerian coordinates. Therefore, we emphasize that:

$$\partial_t\, v_\alpha(x) \neq \frac{\mathrm{d}^2 x_\alpha}{\mathrm{d}t^2}. \tag{3.5}$$

Similarly, the derivatives with respect to the Lagrangian coordinates becomes $\partial x_{0\alpha}(\cdot)$.

For any real-valued function $g = g(x) = g(x(x_0,t))$ of the particle trajectories, we define the function $g_0 := g_0(x_0) = g(x(x_0,0))$, which represents values at the medium's initial configuration.

Finally, we reserve i, j, k to denote particle indices in the discrete setting, so that the comma in $v_{\alpha,i}$ simply separates the α-component of the velocity vector from particle i index.

3.1.1 Measure-valued formulation

The equations derived in the following sections are formulated with the help of three measures, characterizing basic quantities of the medium. Emphatically, we adopt the notation λ, μ and ν.

For a medium found in the domain Ω, its total volume is given by the *Lebesgue measure*:

$$\lambda(\Omega) = \int_\Omega \mathrm{d}\lambda. \tag{3.6}$$

While the volume of a medium changes under certain transformations, its mass:

$$\mu(\Omega) = \int_\Omega \mathrm{d}\mu(x) = \int_{\Omega_0} \mathrm{d}\mu_0(x_0) = \mu_0(\Omega_0), \tag{3.7}$$

is always conserved in the absence of sinks or sources. The above equality is guaranteed by the one-to-one correspondence between the set of particles in the medium's

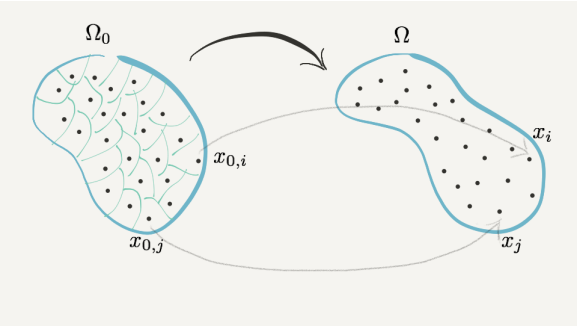

FIGURE 3.2: Transformation of a discretized medium from Ω_0 to Ω.

reference configuration Ω_0 and any later configuration Ω. Similarly, the integration limits in integrals with respect to mass:

$$\int_{\Omega_0} f(x)\,\mathrm{d}\mu_0(x_0) = \int_{\Omega} f(x)\,\mathrm{d}\mu(x), \tag{3.8}$$

may change for any bounded function f.

The measure-valued definition of mass conservation (3.7) is more general than the typical form:

$$\int_{\Omega} \rho(x)\,\mathrm{d}\lambda(x) = \int_{\Omega_0} \rho_0(x_0)\,\mathrm{d}\lambda(x_0), \tag{3.9}$$

since the requirement for a well-defined *mass density*, as the *Radon-Nikodym* derivative of the measure of mass with respect to the Lebesgue measure:

$$\rho(x) = \frac{\mathrm{d}\mu}{\mathrm{d}\lambda}\Big|_{(x)}, \tag{3.10}$$

becomes redundant. Thus, it offers the basis for a generalized approach for both continuous and discretized media. Within this context, we may construct the discrete approximation μ_0^N of μ_0, which can then be used for numerical analysis. Essentially, the continuously distributed mass is "squeezed" towards a countable number of point masses. This construction is achieved using one of the two methods described in a formal manner by Evers et al. [2015].

In principle, consider the partitioning $\Omega_0^N = \{\bigcup_{i=1}^N \Omega_{0,i} = \Omega_0 : \Omega_{0,i} \bigcap \Omega_{0,j\neq i} = \varnothing, \forall i,j \in [1,N]\}$, $N \in \mathbb{N}^+$, and the points $x_{0,i} \in \Omega_{0,i}$ in each subdomain. A condition such as $\max_j \|x_i - x_j\| \to 0, \forall x_j \in \Omega_i$, is necessary to obtain a reasonable partitioning, as $N \to \infty$. A stronger requirement would be to assume $\max_i \lambda(\partial\Omega_i) \to 0$, for $\partial\Omega_i$ denoting the boundary of Ω_i. This concept is visualized in Figure 3.2, for the trajectories of particles i and j. In the first approach, the empirical measure:

$$\mu_0^N = \bar{m} \sum_{i=1}^{N} \delta_{x_{0,i}}, \qquad \bar{m} := \frac{\mu_0(\Omega_0)}{N} \tag{3.11}$$

assigns the same amount of mass to each particle. Particle positions should be carefully chosen, such that they replicate the density function ρ_0. Thus, this procedure can be very demanding for ρ_0 varying in Ω_0. Conversely, the second method delivers equal subdomains $\Omega_{0,i}$. The latter is a simple construction in case Ω_0 is for instance a rectangle in a domain of two spatial dimensions, otherwise the *centroidal Voronoi tessellation* is the relevant procedure. In any other case (e.g. partitioning a sphere with cubes), it should be understood as a converging procedure with increasing N. Eventually, the discrete measure is:

$$\mu_0^N = \sum_{i=1}^{N} m(x_{0,i})\, \delta_{x_{0,i}}, \qquad m(x_{0,i}) := \int_{\Omega_{0,i}} \mathrm{d}\mu_0, \tag{3.12}$$

and due to the one-to-one correspondence of the particles between Ω^N and Ω_0^N, it is also conserved:

$$\mu^N(\Omega) = \int_{\Omega} \mathrm{d}\mu^N(x) = \int_{\Omega_0} \mathrm{d}\mu_0^N(x_0) = \mu_0^N(\Omega_0), \tag{3.13}$$

under any transformation.

The convergence of μ_0^N to μ_0 is intuitively discerned, but the convergence of μ^N to μ is the subject of lengthy proofs [DiLisio et al., 1998; Evers et al., 2015], due to the dynamics involved.

Apart from mass, there exists another invariant quantity in a transforming medium: *the total number of its particles*. Naturally, this becomes infinite for Ω_0 and therefore it is necessary to introduce it as a limiting process.

Essentially, with $N \to \infty$, each $\Omega_{0,i}$ collapses into the point $x_{0,i}$ and the continuous domain is recovered by the set of points. Thus, the total number of subdomains in Ω_0^N is given by the counting measure $\nu_0 = \sum_{i=1}^{N} \delta_{x_{0,i}}$, which is a conserved quantity. The number density n, defined in Equation 2.18 as:

$$n(x_i) = \frac{\int_{\Omega_i} \mathrm{d}\nu}{\int_{\Omega_i} \mathrm{d}\lambda} = \frac{1}{\int_{\Omega_i} \mathrm{d}\lambda}, \tag{3.14}$$

becomes infinite for the continuous system, while the *mass-per-particle density*:

$$m(x_i) = \frac{\int_{\Omega_i} \mathrm{d}\mu}{\int_{\Omega_i} \mathrm{d}\nu} = \int_{\Omega_i} \mathrm{d}\mu, \tag{3.15}$$

reduces to zero in the same limit. A combination of the latter two densities furnishes the mass density as:

$$\lim_{N\to\infty} m(x_i)\, n(x_i) = \lim_{N\to\infty} \frac{\int_{\Omega_i} \mathrm{d}\mu}{\int_{\Omega_i} \mathrm{d}\lambda} = \frac{\mathrm{d}\mu}{\mathrm{d}\lambda}\Big|_{(x)} = \rho(x). \tag{3.16}$$

Additionally, the conservation of mass (3.7) implies that $m(x_i) = \int_{\Omega_i} \mathrm{d}\mu(x) = \int_{\Omega_{0,i}} \mathrm{d}\mu_0(x_0)$, hence is known from the initial configuration. Due to this limiting behavior, it becomes possible to construct the mass density at any time, using the number density and stay within the context of continuum mechanics.

3.1.2 The principle of least action

The *principle of least action* states that the true motion of the continuum is a stationary point of the *action functional*:

$$\mathcal{S} = \int_{t_0}^{t_1} L \, \mathrm{d}t, \quad t_0, t_1 \in [0, T] \tag{3.17}$$

obeying the constraint of initial and final positions [Berdichevsky, 2009, Ch.4]. The *Lagrangian function* is the *difference between the medium's kinetic and potential energy per unit mass e* and is written with the help of the introduced measure as:

$$L = \int_{\Omega} \Big(\frac{1}{2} v_\alpha^2 - e \Big) \, \mathrm{d}\mu = \int_{\Omega_0} \Big(\frac{1}{2} v_\alpha^2 - e \Big) \, \mathrm{d}\mu_0, \tag{3.18}$$

for $e = e(x)$ an explicit or implicit function of the particle positions. Note that the Lagrangian may be written equivalently, with reference to the initial configuration, as described by Equation 3.8. The action's stationary point is found through the action's vanishing variation with respect to an infinitesimally small disturbance δx of the trajectories x:

$$\delta \mathcal{S} \Big|_{t_0}^{t_1} = 0. \tag{3.19}$$

The operator coined with $\delta(\cdot)$ has certain properties, with respect to the already defined differential operators. It commutes with $\mathrm{d}(\cdot)/\mathrm{d}t$ and $\partial(\cdot)/\partial x_{0\alpha}$, while it does not with the spatial derivative $\partial(\cdot)/\partial x_\alpha$ [Berdichevsky, 2009, Ch.4].

The infinitesimal disturbance is chosen such that it vanishes at initial and final times $\delta x|_{t_0} = \delta x|_{t_1} = 0$ and on the boundaries of the domain $\delta x_\alpha|_{\partial\Omega} = 0$ as well. Then, the action's variation expands as:

$$\begin{aligned}
\delta \mathcal{S} \Big|_{t_0}^{t_1} &= \delta \int_{t_0}^{t_1} L \, \mathrm{d}t = \int_{t_0}^{t_1} \int_{\Omega} \Big(\delta \Big(\frac{1}{2} v_\alpha^2 \Big) - \delta e \Big) \, \mathrm{d}\mu \, \mathrm{d}t \\
&= \int_{t_0}^{t_1} \int_{\Omega} \Big(v_\alpha \, \delta v_\alpha - \frac{\delta e}{\delta x_\alpha} \delta x_\alpha \Big) \, \mathrm{d}\mu \, \mathrm{d}t \\
&= \int_{t_0}^{t_1} \int_{\Omega} \Big(v_\alpha \, \frac{\mathrm{d}}{\mathrm{d}t} \Big(\delta x_\alpha \Big) - \frac{\delta e}{\delta x_\alpha} \, \delta x_\alpha \Big) \, \mathrm{d}\mu \, \mathrm{d}t \\
&= \int_{t_0}^{t_1} \int_{\Omega} \Big(- \frac{\mathrm{d}v_\alpha}{\mathrm{d}t} \delta x_\alpha - \frac{\delta e}{\delta x_\alpha} \delta x_\alpha \Big) \, \mathrm{d}\mu \, \mathrm{d}t + \int_{\Omega} \Big[v_\alpha \delta x_\alpha \Big]_{t_0}^{t_1} \mathrm{d}\mu = 0.
\end{aligned} \tag{3.20}$$

Since the variation vanishes at initial and final times, the last term of Equation 3.20 drops and thus the variational principle writes:

$$\int_{t_0}^{t_1} \int_{\Omega} \Big(\frac{\mathrm{d}v_\alpha}{\mathrm{d}t} + \frac{\delta e}{\delta x_\alpha} \Big) \delta x_\alpha \, \mathrm{d}\mu \, \mathrm{d}t = 0. \tag{3.21}$$

Note that by preserving the notation $\delta e / \delta x_\alpha$, we imply that the internal energy might be a functional, rather than a function. The *fundamental lemma of calculus of variations*

states [Berdichevsky, 2009, Ch.4] that in order for the previous Equation 3.21 to hold for any arbitrary variation δx_α, the integrand should be zero and therefore the equation of motion for each point of the system becomes:

$$\frac{\mathrm{d}v_\alpha}{\mathrm{d}t} = -\frac{\delta e}{\delta x_\alpha}. \tag{3.22}$$

Nonetheless, the functions of potential energy which are examined further on involve implications. Thus, in order to find the functional derivative $\delta e/\delta x_\alpha$, we first seek the variation of the energy functional in the form:

$$\delta\mathcal{E}\Big|_{t_0}^{t_1} = \int_{t_0}^{t_1}\int_\Omega \delta e \;\mathrm{d}\mu\,\mathrm{d}t = \int_{t_0}^{t_1}\int_\Omega \frac{\delta e}{\delta x_\alpha}\delta x_\alpha \;\mathrm{d}\mu\,\mathrm{d}t. \tag{3.23}$$

With this expression at hand, the variational principle is written in the form of Equation 3.21 and Equation 3.22, the equation of motion, follows straightforwardly.

3.1.3 Thermodynamic relations

A particularly interesting form of potential energy is a system's *internal energy*, for which an expression for its change is known, rather than an explicit formula. In what follows, we consider internal energy as the only form of potential energy in the system. For processes which are *reversible*, meaning that they follow a continuous thermodynamic path of equilibria, the medium's thermodynamic state is fully determined by the $k+1$ state variables $\xi_1, \xi_2, ..., \xi_k$ and s. Here ξ_r are the *thermodynamic substate variables* and s is the specific entropy [Malvern, 1969, Ch.5]. Thus, a general *caloric equation of state* provides the internal energy per unit mass:

$$e = e(s, \pi_r, x_0), \tag{3.24}$$

with the *thermodynamic temperature* and the *thermodynamic tensions* defined by

$$T := \frac{\partial e}{\partial s}\Big|_{\xi}, \qquad \pi_r := \frac{\partial e}{\partial \xi_r}\Big|_{s}, \qquad r = 1, 2, ..., k. \tag{3.25}$$

Note that inhomogeneous media are permitted by the form of e due to x_0, the initial particle positions. The change of internal energy within the system is then delivered by *Gibbs' relation for thermodynamics*:

$$\mathrm{d}e = T\,\mathrm{d}s + \pi_r\,\mathrm{d}\xi_r, \tag{3.26}$$

which accommodates the changes of the system's entropy, while at the same time it provides a very broad framework for physical modeling. What is necessary, is to choose the relevant thermodynamic substate variables and use their *conjugate* thermodynamic tensions. The latter may include mechanical, electromagnetic or chemical effects in the system. These describe the part of the internal energy which is available for use by the system —this is the concept of *work*. The variation of the internal energy δe is required by the equation of motion .

We first examine a form of internal energy which is encountered in *ideal media*. This term refers to media for which their internal energy varies with the medium's specific volume $1/\rho$, constituting $e = e(\rho)$. The conjugate thermodynamic tension of volume is a mean volumetric stress P, the *pressure*, at each particle of the medium [Malvern, 1969, Ch.5]. By convention, it is taken to be positive under compression and ultimately:

$$\mathrm{d}e|_s = P\mathrm{d}\Big(1/\rho\Big) = \frac{P}{\rho^2}\mathrm{d}\rho. \tag{3.27}$$

Thus, in view of the least action principle, the equation of motion of an ideal compressible medium depends on how ρ changes in the system.

3.2 Classical equations

The one-to-one correspondence between the initial particle positions x_0 and the current ones $x = x(x_0, t)$, seconded by the fixed infinitesimal masses which are associated to each particle, imply that:

$$\mathrm{d}\mu(x) = \mathrm{d}\mu_0(x_0). \tag{3.28}$$

The definition of the medium's density function (3.10) delivers:

$$\rho(x)\,\mathrm{d}\lambda(x) = \rho_0(x_0)\,\mathrm{d}\lambda(x_0). \tag{3.29}$$

Volume increments are translated to length increments per direction [Malvern [1969], Ch.4; Berdichevsky [2009], Ch.3; Seliger and Whitham [1968]]:

$$\rho\,\mathrm{d}x_1\,\mathrm{d}x_2\,\mathrm{d}x_3 = \rho_0\,\mathrm{d}x_{01}\,\mathrm{d}x_{02}\,\mathrm{d}x_{03}, \tag{3.30}$$

and consequently the classical medium's density:

$$\rho(x) = \rho_0(x_0)\frac{1}{J(x)}, \tag{3.31}$$

turns out to be a function of the *Jacobian matrix*:

$$\mathbf{J} = \frac{\partial(x_1, x_2, x_3)}{\partial(x_{01}, x_{02}, x_{03})}, \qquad J_{\beta\gamma} = \frac{\partial J}{\partial x_{\beta\gamma}}, \tag{3.32}$$

via its determinant $J = \epsilon_{\alpha\beta\gamma}\, x_{1\alpha}\, x_{2\beta}\, x_{3\gamma}$, for $\epsilon_{\alpha\beta\gamma}$ *the Levi-Civita symbol* [Berdichevsky [2009],Ch.3; Seliger and Whitham [1968]]. Note that this form of mass conservation is useful only if the reference configuration is different than the current configuration. Thus it is typically used for problems in the total Lagrangian formulation.

From Equation 3.27, the medium's internal energy becomes $e = e(\rho(J))$ and the variation of density is:

$$\delta\rho = \frac{\mathrm{d}\rho}{\mathrm{d}J}\frac{\partial J}{\partial x_{\alpha\beta}}\delta x_{\alpha\beta} = -\frac{\rho_0}{J^2}\frac{J}{x_{\alpha\beta}}\delta\Big(\frac{\partial x_\alpha}{\partial x_{0\beta}}\Big) = -\frac{\rho_0}{J}\frac{\partial x_{0\beta}}{\partial x_\alpha}\frac{\partial}{\partial x_{0\beta}}\Big(\delta x_\alpha\Big) = -\rho\partial_\alpha\Big(\delta x_\alpha\Big). \tag{3.33}$$

Given a temporal variation of the positions of the medium, we arrive at the *continuity equation*[1]:

$$\frac{\mathrm{d}\rho}{\mathrm{d}t} = -\rho\,\partial_\alpha v_\alpha. \tag{3.34}$$

For the total Lagrangian description, both Equations 3.31 and 3.34 can be used, while for the updated Lagrangian, only the latter is useful.

In order to write out the equation of motion (3.22), the variation of energy with respect to a variation in δx is required. To this end, we start by writing:

$$\delta e = \frac{\mathrm{d}e}{\mathrm{d}\rho}\delta\rho = -\frac{P}{\rho^2}\rho\,\partial_\alpha\Big(\delta x_\alpha\Big). \tag{3.35}$$

According to the derivation strategy the variation of energy is cast into the variation of the functional in Equation 3.23:

$$\begin{aligned}
\delta\mathcal{E}\Big|_{t_0}^{t_1} &= \int_{t_0}^{t_1}\int_\Omega \delta e\,\mathrm{d}\mu\,\mathrm{d}t = -\int_{t_0}^{t_1}\int_\Omega \frac{P}{\rho}\,\partial_\alpha\Big(\delta x_\alpha\Big)\,\mathrm{d}\mu\,\mathrm{d}t \\
&= -\int_{t_0}^{t_1}\int_\Omega P\partial_\alpha\Big(\delta x_\alpha\Big)\,\mathrm{d}\lambda\,\mathrm{d}t \\
&= -\int_{t_0}^{t_1}\int_\Omega \partial_\alpha\Big(P\,\delta x_\alpha\Big)\,\mathrm{d}\lambda\,\mathrm{d}t + \int_{t_0}^{t_1}\int_\Omega \partial_\alpha P\delta x_\alpha\,\mathrm{d}\lambda\,\mathrm{d}t \\
&= -\int_{t_0}^{t_1}\int_{\partial\Omega}\Big[P\,\delta x_\alpha\Big]_{\partial\Omega}\zeta_\alpha\,\mathrm{d}\Gamma\,\mathrm{d}t + \int_{t_0}^{t_1}\int_\Omega \frac{1}{\rho}\partial_\alpha P\,\delta x_\alpha\,\mathrm{d}\mu\,\mathrm{d}t \\
&= \int_{t_0}^{t_1}\int_\Omega \frac{1}{\rho}\partial_\alpha P\,\delta x_\alpha\,\mathrm{d}\mu\,\mathrm{d}t.
\end{aligned} \tag{3.36}$$

where we used the definition $\rho = \mathrm{d}\mu/\mathrm{d}\lambda$ and the fact that the variation $\delta x|_{\partial\Omega} = 0$ vanishes on the boundaries $\partial\Omega$ with outward normal unit vector ζ_α. With the integral of δe above in the form required by the variation of the action in Equation 3.20, the equation of motion (3.22) becomes:

$$\frac{\mathrm{d}v_\alpha}{\mathrm{d}t} = -\frac{1}{\rho}\partial_\alpha P. \tag{3.37}$$

This is the *Euler equation* for inviscid flows, written in terms of the material derivative of velocity[2].

[1] The continuity equation can also be derived from Equation 3.9 by applying the *Reynolds transport theorem* and the *Gauss theorem* [Berdichevsky, 2009, Ch.3]. Notably, the latter is an approach more flavored by the fluid mechanics community. Presumably because it does not involve the introduction of any reference configuration which is a concept closer to solid mechanics.

[2] In case a variational principle with respect to the Eulerian coordinates is pursued, by comparison of Equation 3.37 to 3.22, the Lagrangian is simply the pressure P. The proof is quite involved and is based on *Clebsch potentials*, as shown in Seliger and Whitham [1968].

3.3 Smoothed equations

The definition of a continuous medium guarantees a continuous mass distribution, which results in the density $\rho = \mathrm{d}\mu/\mathrm{d}\lambda$. Nevertheless, in order to describe the mass distribution in a more general way and thus include cases of discontinuous media, the measure-based formulation (3.7) offers an alternative.

The smoothed density obtains a weak derivative and thus conveys continuous solutions to the equation of motion through internal energy, as exhibited by the thermodynamic relation (3.26). Three different smoothed density estimates are introduced and the corresponding equations of motion are derived.

3.3.1 Mass-smoothed medium

The measure of mass (3.7) obtains the smoothed density:

$$\tilde{\rho}(x) = \int_\Omega W(x-y)\,\mathrm{d}\mu(y), \tag{3.38}$$

where $y := x(y_0, t)$ for any y_0 particle of the medium at the reference configuration. It is the continuous form of the classical SPH density estimate [Monaghan, 2005; Monaghan and Gingold, 1983; Price, 2012]. The smoothed density's variation with respect to a change in the medium's positions is:

$$\delta\tilde{\rho}(x) = \int_\Omega \partial_\alpha W(x-y)\left(\delta x_\alpha - \delta y_\alpha\right)\mathrm{d}\mu(y). \tag{3.39}$$

Therefore, a temporal variation of the particle trajectories delivers the medium's continuity equation:

$$\left.\frac{\mathrm{d}\tilde{\rho}}{\mathrm{d}t}\right|_{(x)} = \int_\Omega \partial_\alpha W(x-y)\left(v_\alpha(x) - v_\alpha(y)\right)\mathrm{d}\mu(y). \tag{3.40}$$

The evolution of density constitutes a *differential form of mass conservation for the smoothed system*, as opposed to the *integral form of mass conservation* appearing in Equation 3.10. Moreover, any allusion to the reference configuration is disregarded in the derivation of the continuity equation of the smoothed medium. Thus, the description of the medium always corresponds to the updated Lagrangian, as delineated in the beginning of the chapter.

By adopting $\tilde{\rho}$, the internal energy of the smoothed medium becomes $e = e(\tilde{\rho}(x))$ and from the thermodynamic relation (3.26), it follows that $P = P(\tilde{\rho}, e)$. The variation of the medium's internal energy is:

$$\delta e(x) = \left.\frac{\partial e}{\partial\tilde{\rho}}\right|_{(x)}\delta\tilde{\rho}(x) = \left.\frac{P}{\tilde{\rho}^2}\right|_{(x)}\int_\Omega \partial_\alpha W(x-y)\left(\delta x_\alpha - \delta y_\alpha\right)\mathrm{d}\mu(y), \tag{3.41}$$

and the energy functional varies as:

$$\delta\mathcal{E}\Big|_{t_0}^{t_1} = \int_{t_0}^{t_1}\int_\Omega \delta e\,\mathrm{d}\mu\,\mathrm{d}t =$$

$$
\begin{aligned}
&= \int_{t_0}^{t_1} \int_\Omega \left(\int_\Omega \frac{P}{\tilde{\rho}^2}\Big|_{(x)} \partial_\alpha W(x-y)\, \mathrm{d}\mu_0(y) \right) \delta x_\alpha \, \mathrm{d}\mu(x)\mathrm{d}t \\
&\quad - \int_{t_0}^{t_1} \int_\Omega \int_\Omega \frac{P}{\tilde{\rho}^2}\Big|_{(x)} \partial_\alpha W(x-y)\, \delta y_\alpha \, \mathrm{d}\mu(y)\mathrm{d}\mu(x)\, \mathrm{d}t \\
&= \int_{t_0}^{t_1} \int_\Omega \left[\int_\Omega \left(\frac{P}{\tilde{\rho}^2}\Big|_{(x)} + \frac{P}{\tilde{\rho}^2}\Big|_{(y)} \right) \partial_\alpha W(x-y) \mathrm{d}\mu(y) \right] \delta x_\alpha \, \mathrm{d}\mu(x)\, \mathrm{d}t. \qquad (3.42)
\end{aligned}
$$

A critical step is that we swap x with y in the second term and use the antisymmetry property of the gradient of the smoothing function (see properties of the smoothing function in Chapter 2). Ultimately, the variation of the energy functional is in the form of Equation 3.23, whence Equation 3.22 delivers:

$$
\frac{\mathrm{d}v_\alpha}{\mathrm{d}t}\Big|_{(x)} = -\int_\Omega \left(\frac{P}{\tilde{\rho}^2}\Big|_{(x)} + \frac{P}{\tilde{\rho}^2}\Big|_{(y)} \right) \partial_\alpha W(x-y)\, \mathrm{d}\mu(y), \qquad (3.43)
$$

the *equation of motion for the mass-based smoothed medium*.

By introducing the discrete measure $\mu^N = \sum_i m(x_i)\, \delta_{x_i}$, we obtain:

$$
\frac{\mathrm{d}\tilde{\rho}}{\mathrm{d}t}\Big|_{(x_i)} = \sum_j \partial_\alpha W(x_i - x_j) \Big(v_\alpha(x_i) - v_\alpha(x_j) \Big) m(x_j), \qquad (3.44)
$$

$$
\frac{\mathrm{d}v_\alpha}{\mathrm{d}t}\Big|_{(x_i)} = -\sum_j \left(\frac{P(\tilde{\rho})}{\tilde{\rho}^2}\Big|_{(x_i)} + \frac{P(\tilde{\rho})}{\tilde{\rho}^2}\Big|_{(x_j)} \right) \partial_\alpha W(x_i - x_j)\, m_j, \qquad (3.45)
$$

the discrete SPH scheme of the mass-smoothed medium.

3.3.2 Volume-smoothed medium

Although the conservation of volume is not a principle of mechanics, another scheme is derived starting from the medium's *characteristic function* or *color function*:

$$
q_\Omega(z) = \begin{cases} 1, & z \in \Omega, \\ 0, & z \notin \Omega. \end{cases} \qquad (3.46)
$$

Within the medium, the latter obtains the smoothed version:

$$
\tilde{q}_\Omega(x) = \int_\Omega W(x-y)\, \mathrm{d}\lambda(y), \qquad (3.47)
$$

which may be used to construct the smoothed density:

$$
\tilde{\rho} = \rho\, \tilde{q}. \qquad (3.48)
$$

Considering that $\rho = \mathrm{d}\mu/\mathrm{d}\lambda$, the variation of the previous becomes:

$$
\delta\tilde{\rho}(x) = \delta\rho(x) \int_\Omega W(x-y)\, \frac{\mathrm{d}\mu}{\rho}\Big|_{(y)}
$$

$$
\begin{aligned}
&+\rho(x)\Big(\int_\Omega \delta W(x-y)\frac{\mathrm{d}\mu}{\rho}\Big|_{(y)} - \int_\Omega W(x-y)\frac{\delta\rho\,\mathrm{d}\mu}{\rho^2}\Big|_{(y)}\Big)\\
&= \delta\rho(x)\,H(x) + \rho(x)\int_\Omega \delta W(x-y)\frac{\mathrm{d}\mu}{\rho}\Big|_{(y)} - \rho(x)\Big(\frac{\delta\rho}{\rho}\Big|_{(x)} H(x) + \mathcal{O}(h^\xi)\Big)\\
&= \rho(x)\int_\Omega \delta W(x-y)\frac{\mathrm{d}\mu}{\rho}\Big|_{(y)} + \mathcal{O}(h^\xi),
\end{aligned}
\tag{3.49}
$$

for a *Taylor expansion* of the integrand in the third term around y, defining $H(x) \equiv \int_\Omega W(x-y)\mathrm{d}\lambda(y)$ and $0 \leq \xi \leq 2$. This procedure is explained in more detail in Section 2.4. Nonetheless, the function ρ is unknown and the above is considered as a substitution:

$$
\delta\tilde{\rho} = \tilde{\rho}(x)\int_\Omega W(x-y)\Big(\delta x_\alpha - \delta y_\alpha\Big)\frac{\mathrm{d}\mu}{\tilde{\rho}}\Big|_{(y)} + \mathcal{O}(h^\xi),
\tag{3.50}
$$

introducing error terms. The implications related to the convergence of this scheme are discussed in Section 3.4, wherein it is shown that $\xi \geq 0$. We continue with the derivation of the scheme.

Notice that this density construct requires the definition of a volume around a particle, which is apparent in Equation 3.51. This is not a requirement of density constructs coming from the conserved quantities of mass or number of particles (as shown in the following section). We can actually conjecture that any variation of density coming from the smoothing of a variant quantity of the system, is bound to be approximate; e.g. the density estimators which Monaghan [2005] and Price [2012] review in the discrete setting. This detail is discussed in the following chapter.

Inarguably, for this scheme there only exists a differential form of mass conservation, which is given for a temporal variation of the particle positions:

$$
\frac{\mathrm{d}\tilde{\rho}}{\mathrm{d}t}\Big|_{(x)} = \tilde{\rho}(x)\int_\Omega \partial_\alpha W\Big(v_\alpha(x) - v_\alpha(y)\Big)\frac{\mathrm{d}\mu}{\tilde{\rho}}\Big|_{(y)}.
\tag{3.51}
$$

The variation of energy is:

$$
\delta e(x) = \frac{\partial e}{\partial\tilde{\rho}}\Big|_{(x)}\delta\tilde{\rho}(x) = \tilde{\rho}(x)\int_\Omega \partial_\alpha W(x-y)\left(\delta x_\alpha - \delta y_\alpha\right)\frac{\mathrm{d}\mu}{\tilde{\rho}}|_{(y)},
\tag{3.52}
$$

and consequently, the variation of the energy functional becomes:

$$
\begin{aligned}
\delta\mathcal{E}\Big|_{t_0}^{t_1} &= \int_{t_0}^{t_1}\int_\Omega \delta e\,\mathrm{d}\mu(x)\,\mathrm{d}t =\\
&= \int_{t_0}^{t_1}\int_\Omega \frac{P}{\tilde{\rho}}\Big|_{(x)}\int_\Omega \frac{1}{\tilde{\rho}(y)}\partial_\alpha W(x-y)\left(\delta x_\alpha - \delta y_\alpha\right)\mathrm{d}\mu(y)\,\mathrm{d}\mu(x)\,\mathrm{d}t\\
&= \int_{t_0}^{t_1}\int_{\Omega_0}\left(\int_\Omega \frac{P}{\tilde{\rho}}\Big|_{(x)}\frac{1}{\tilde{\rho}(y)}\partial_\alpha W(x-y)\,\mathrm{d}\mu(y)\right)\delta x_\alpha\,\mathrm{d}\mu(x)\mathrm{d}t\\
&\quad - \int_{t_0}^{t_1}\int_\Omega\int_\Omega \frac{P}{\tilde{\rho}}\Big|_{(x)}\frac{1}{\tilde{\rho}(y)}\partial_\alpha W(x-y)\,\delta y_\alpha\,\mathrm{d}\mu(y)\mathrm{d}\mu(x)\,\mathrm{d}t
\end{aligned}
$$

$$= \int_{t_0}^{t_1} \int_\Omega \left[\int_\Omega \left(\frac{P(x) + P(y)}{\tilde{\rho}(x)\,\tilde{\rho}(y)} \right) \partial_\alpha W(x-y) \mathrm{d}\mu(y) \right] \delta x_\alpha \,\mathrm{d}\mu(x)\,\mathrm{d}t. \tag{3.53}$$

In the second term, we swap y with x and use the antisymmetry property of ∂W. All in all, the acceleration of the particles is:

$$\frac{\mathrm{d}v_\alpha}{\mathrm{d}t}\Big|_{(x)} = -\int_\Omega \left(\frac{P(\tilde{\rho}(x)) + P(\tilde{\rho}(y))}{\tilde{\rho}(x)\,\tilde{\rho}(y)} \right) \partial_\alpha W(x-y)\,\mathrm{d}\mu(y), \tag{3.54}$$

and constitutes the *equation of motion for the volume-smoothed medium*. Obviously, the scheme which arrives from the volume-based smoothing has a clear description in the continuous setting. The derivation of this scheme is typically performed [Bonet and Lok, 1999; Monaghan, 2005] at the particle level and requires the continuity equation as a starting point. The present derivation starts from a more basic property of the medium, the measure of its volume and hence, from this point of view, the present derivation seems more general than older ones.

By introducing the discrete measure $\mu^N = \sum_i m(x_i)\,\delta_{x_i}$, we obtain:

$$\frac{\mathrm{d}\tilde{\rho}}{\mathrm{d}t}\Big|_{(x_i)} = \tilde{\rho}(x_i) \sum_j \partial_\alpha W\Big(v_\alpha(x_i) - v_\alpha(x_j)\Big) \frac{m(x_j)}{\tilde{\rho}(x_j)}, \tag{3.55}$$

$$\frac{\mathrm{d}v_\alpha}{\mathrm{d}t}\Big|_{(x_i)} = -\sum_j \left(\frac{P(\tilde{\rho}(x_i)) + P(\tilde{\rho}(x_j))}{\tilde{\rho}(x_j)\,\tilde{\rho}(x_j)} \right) \partial_\alpha W(x_i - x_j)\, m_j, \tag{3.56}$$

the discrete SPH scheme of the volume-smoothed medium.

3.3.3 Number-smoothed medium

As exhibited in Section 3.1.1, the number of the medium's particles is an invariant of the system and its number density n can be used to construct the mass density. Similarly to the smoothing of the measure of mass, the smoothing of the counting measure provides the smoothed number-density:

$$\tilde{n}(x) = \int_\Omega W(x-y)\,\mathrm{d}\nu(y). \tag{3.57}$$

This smoothed estimate is defined at all points x, in contrast to number density (2.18), which is defined only at specific points x_i, according to the partitioning of Ω. Eventually, the smoothed estimate of mass density becomes:

$$\tilde{\rho}(x_i) = m(x_i)\,\tilde{n}(x_i) = \int_\Omega W(x_i - y)\,\mathrm{d}\nu(y), \tag{3.58}$$

and it is also defined only at the discrete points x_i. In the form of sum, Equation 3.58 is:

$$\tilde{\rho}(x_i) = m(x_i) \sum_j W(x_i - x_j). \tag{3.59}$$

Hu and Adams [2006] worked on this estimate, without showing its precise relation to the classic mass-smoothed one. To highlight the difference of the previous estimate to the mass-smoothed estimate (3.38), consider the smoothing:

$$\widetilde{m\,n}\Big|(x_i) = \sum_j m(x_j)\, n(x_j)\, W(x_i - x_j) \int_{\Omega_j} \mathrm{d}\lambda$$
$$= \sum_j m(x_j)\, n(x_j)\, W(x_i - x_j) \frac{\int_{\Omega_j} \mathrm{d}\nu}{n(x_j)} = \sum_j W(x_i - x_j) \int_{\Omega_j} \mathrm{d}\mu. \tag{3.60}$$

Notice that in Equation 3.58 the smoothing appears for n, but not for m. The limiting behavior of the number-smoothed estimate is:

$$\lim_{N\to\infty} \tilde{\rho}(x_i) = \lim_{N\to\infty} m(x_i)\, \tilde{n}(x_i) = \lim_{N\to\infty} \sum_j W(x_i - x_j) \frac{m(x_i)}{m(x_j)} \int_{\Omega_j} \mathrm{d}\mu$$
$$= \lim_{N\to\infty} \sum_j W(x_i - x_j) \int_{\Omega_j} \mathrm{d}\mu = \rho(x_i). \tag{3.61}$$

Notice that the final sum is simply the density of the mass-smoothed medium, expressed in the discrete setting. To arrive at the previous result, recall that $W \equiv W_h$. Then, for a regular configuration of the points of the discrete space, $N \to \infty$ implies $n \to \infty$, which results in $h \to 0$, due to Equation 2.20. This means that the contributions of the terms $m(x_i)/m(x_j)$ from particles j around i decrease fast, and the term $m(x_i)/m(x_{j=i})$ dominates. The latter holds as far as $m(x_i)$ and $m(x_j)$ in the summation are not of extremely different scales.

Upon a variation of the trajectories, the constructed density becomes:

$$\delta\tilde{\rho}(x_i) = m(x_i) \sum_j \partial_\alpha W(x_i - x_j) \Big(\delta x_{\alpha,i} - \delta x_{\alpha,j} \Big), \tag{3.62}$$

keeping in mind that the variation of $m(x_i) = m_0(x_{0,i})$ is zero by construction, since it is not affected by a shift of the particle's position. For a temporal variation, the estimate above delivers the medium's continuity equation:

$$\frac{\mathrm{d}\tilde{\rho}}{\mathrm{d}t}\Big|_{(x_i)} = m(x_i) \sum_j \partial_\alpha W(x_i - x_j) \Big(v_\alpha(x_i) - v_\alpha(x_j) \Big), \tag{3.63}$$

furnishing the variation of the internal energy functional (3.23):

$$\delta\mathcal{E}\Big|_{t_0}^{t_1} = \int_{t_0}^{t_1} \int_\Omega \delta e \, \mathrm{d}\mu \, \mathrm{d}t$$
$$= \int_{t_0}^{t_1} \sum_i \left(\frac{m\,P}{\tilde{\rho}^2}\Big|_{(x_i)} \sum_j \partial_\alpha W(x_i - x_j) \right) \delta x_{\alpha,i}\, m(x_i) \mathrm{d}t$$
$$- \int_{t_0}^{t_1} \sum_i \sum_j \frac{m\,P}{\tilde{\rho}^2}\Big|_{(x_i)} \partial_\alpha W(x_i - x_j)\, \delta x_{\alpha,j}\, m(x_i)\, \mathrm{d}t$$

$$= \int_{t_0}^{t_1} \sum_i \left[\sum_j \left(\frac{m^2 P}{\tilde{\rho}^2}\Big|_{(x_i)} + \frac{m^2 P}{\tilde{\rho}^2}\Big|_{(x_j)} \right) \partial_\alpha W(x_i - x_j) \right] \delta x_{\alpha,i} \, \mathrm{d}t$$

$$= \int_{t_0}^{t_1} \sum_i \sum_j \left(\frac{m^2 P}{\tilde{\rho}^2}\Big|_{(x_i)} + \frac{m^2 P}{\tilde{\rho}^2}\Big|_{(x_j)} \right) \partial_\alpha W(x_i - x_j) \, \delta x_{\alpha,i} \frac{\int_{\Omega_i} \mathrm{d}\mu}{m(x_i)} \, \mathrm{d}t. \tag{3.64}$$

Similarly to the functional in the mass-based smoothing, we change x_i for x_j and use the antisymmetry of $\partial_\alpha W$.

Notice that the limit $N \to \infty$ of the latter relation equals $\int_{t0}^{t1} \delta e \, \delta x_\alpha \mathrm{d}\mu \, \mathrm{d}t$ and eventually, the variation of the energy functional is in the form of Equation 3.23. Thus Equation 3.22 delivers:

$$\frac{\mathrm{d}v_\alpha}{\mathrm{d}t}\Big|_{(x_i)} = -\frac{1}{m(x_i)} \sum_j \left(\frac{m^2 P}{\tilde{\rho}^2}\Big|_{(x_i)} + \frac{m^2 P}{\tilde{\rho}^2}\Big|_{(x_j)} \right) \partial_\alpha W(x_i - y_j), \tag{3.65}$$

the *equation of motion for the number-smoothed medium*.

3.3.4 Discussion

Bonet and Lok [1999], Monaghan [2005] and Price [2012] start from the (discrete) Lagrangian of a particle system under the constraint of the discrete version of the density estimate (3.10). The difference is that our approach starts from the continuum, derives the equations at a continuous setting and in the end discretizes the derived equations. Additionally, it shows the relation of the traditional SPH estimate to the estimate employing the number-density. This has two advantages. First, convergence properties of the schemes may be studied rigorously as in Evers et al. [2015] and DiLisio et al. [1998]. Second, it becomes clear that SPH is not only about a loose particle representation of the continuum as $N \to \infty$. There exists a strict and defined correspondence with processes taking place at the level of continuum. Moreover, it is evident that the SPH equations refer to a specific type of continuous medium: *the smoothed medium*. Thus, we can state that *SPH is the numerical method which solves the equations of continuum mechanics for the smoothed medium*. Another characteristic of SPH is that media are discretized with respect to their mass or by discretizing the continuum into a finite number of particles. This concept is in contrast to the Finite Element Method or the Finite Volume Method —either in their Eulerian or Lagrangian description of the flow field, which integrate over the medium's volume. Two significant properties arise from this feature. First, a mesh over the domain is redundant; SPH is a truly mesh-free method. Second, even for extreme changes of the domain, remeshing —which would correspond to redistribution of masses— is not necessary[3]. Additionally, in this way discontinuous media —predominantly occurring in free surface flows or fragmentation of solids— are handled with ease. Moreover, the integration with respect to the medium's mass, one of the system's

[3]This property is not universal, as there are non-standard SPH algorithms which employ redistribution of mass or particle splitting/merging techniques.

invariants, endows the property of exact mass conservation. Furthermore, having derived the equations consistently from the action principle, the method inherits the property of momentum conservation, at least without considering errors from time integration [Price, 2012]. The same holds true for energy if ideal media are considered. Finally, the advantages discussed do not come without any cost. The idealization of the smoothed medium raises the question: *under which circumstances does the smoothed medium behave the same as the classical one?* This question is discussed in the next section.

3.4 Convergence of the SPH schemes

The following analysis reveals how the derived smoothed equations of Section 3.3 converge to the classic ones of Section 3.2, in the limit $h \to 0$. Inarguably, such an analysis corresponds to a static case and disregards the system's dynamical evolution. Effectively, time is considered as a parameter. By this we mean that given the necessary function values at some time instance, the systems of smoothed equations in Section 3.3 may be interpreted as approximations of the equations in Section 3.2 at that time instance.

Our strategy is the following. We work out the derived equations of the smoothed medium so that we can write them in terms of the equations of the classic medium. Then, the conditions under which the two forms are equal give us the desired conditions for convergence as $h \to 0$. We follow the concepts developed in Monaghan [2005] and Price [2012] and we highlight the distinction between the smoothed density $\tilde{\rho}$ and the density $\rho = \mathrm{d}\mu/\mathrm{d}\lambda$. This remark allows us to trace a nonlinearity which is typically shunned in most SPH error analyses.

3.4.1 Mass-smoothed medium

The continuity equation of the mass-smoothed medium:

$$\begin{aligned}\frac{\mathrm{d}\tilde{\rho}}{\mathrm{d}t}\Big|_{(x)} &= \int_\Omega \partial_\alpha W(x-y)\Big(v_\alpha(x) - v_\alpha(y)\Big)\,\mathrm{d}\mu(y)\\ &= v_\alpha(x)\int_\Omega \partial_\alpha W(x-y)\,\mathrm{d}\mu(y) - \int_\Omega v_\alpha(y)\,\partial_\alpha W(x-y)\,\mathrm{d}\mu(y)\\ &= v_\alpha(x)\int_\Omega \rho(y)\,\partial_\alpha W(x-y)\,\mathrm{d}\lambda(y) - \int_\Omega \rho(y)\,v_\alpha(y)\,\partial_\alpha W(x-y)\,\mathrm{d}\lambda(y),\end{aligned}$$

is the up to $\mathcal{O}(h)$-terms approximation:

$$\begin{aligned}\frac{\mathrm{d}\tilde{\rho}}{\mathrm{d}t}\Big|_{(x)} &\approx v_\alpha\Big[\rho\,K_\alpha + \partial_\beta\rho\,\Lambda_{\beta\alpha}\Big] - \Big[\rho\,v_\alpha\,K_\alpha + \partial_\beta\Big(\rho\,v_\alpha\Big)\,\Lambda_{\beta\alpha}\Big]\\ &= \Big[v_\alpha\partial_\alpha\rho - \partial_\beta\Big(\rho\,v_\alpha\Big)\Big]\Lambda_{\beta\alpha} = -\rho\,\partial_\beta v_\alpha\,\Lambda_{\beta\alpha},\end{aligned} \tag{3.66}$$

according to Equation 2.49. In the same way, the corresponding equation of motion:

$$\begin{aligned}\frac{\mathrm{d}v_\alpha}{\mathrm{d}t}\Big|_{(x)} &= -\int_\Omega \Big(\frac{P}{\tilde\rho^2}\Big|_{(x)} + \frac{P}{\tilde\rho^2}\Big|_{(y)}\Big)\,\partial_\alpha W(x-y)\,\mathrm{d}\mu(y)\\ &= -\frac{P}{\tilde\rho^2}\Big|_{(x)}\int_\Omega \partial_\alpha W(x-y)\,\mathrm{d}\mu(y) - \int_\Omega \frac{P}{\tilde\rho^2}\Big|_{(y)}\partial_\alpha W(x-y)\,\mathrm{d}\mu(y)\\ &= -\frac{P}{\tilde\rho^2}\Big|_{(x)}\int_\Omega \rho(y)\partial_\alpha W(x-y)\,\mathrm{d}\lambda(y) - \int_\Omega \frac{P\rho}{\tilde\rho^2}\Big|_{(y)}\partial_\alpha W(x-y)\,\mathrm{d}\lambda(y),\end{aligned}$$

leads to the approximation of up to $\mathcal{O}(h)$-terms:

$$\begin{aligned}\frac{\mathrm{d}v_\alpha}{\mathrm{d}t}\Big|_{(x)} &\approx -\frac{P}{\tilde\rho^2}\Big[\rho\,K_\alpha + \partial_\beta\rho\,\Lambda_{\beta\alpha}\Big] - \Big[\frac{P\rho}{\tilde\rho^2}\,K_\alpha + \partial_\beta\Big(\frac{P\rho}{\tilde\rho^2}\Big)\,\Lambda_{\beta\alpha}\Big]\\ &= -\Big[\frac{P}{\tilde\rho^2}\partial_\beta\rho + \partial_\beta\Big(\frac{P\rho}{\tilde\rho^2}\Big)\Big]\Lambda_{\beta\alpha} - 2\frac{P\rho}{\tilde\rho^2}K_\alpha\\ &= -\Big[2\frac{P}{\tilde\rho^2}\partial_\beta\rho + \rho\,\partial_\beta\Big(\frac{P}{\tilde\rho^2}\Big)\Big]\Lambda_{\beta\alpha} - 2\frac{P\rho}{\tilde\rho^2}K_\alpha\\ &= -\Big[2\frac{P}{\tilde\rho^2}\partial_\beta\rho - 2\frac{P\rho}{\tilde\rho^3}\partial_\beta\tilde\rho + \frac{\rho}{\tilde\rho^2}\partial_\beta P\Big]\Lambda_{\beta\alpha} - 2\frac{P\rho}{\tilde\rho^2}K_\alpha.\end{aligned} \tag{3.67}$$

Let us simplify the problem by assuming $P = P(\tilde\rho)$, instead of $P = P(\tilde\rho, e)$. Additionally, we consider $P(\tilde\rho) = c\tilde\rho^\gamma$, with γ the ratio of heat coefficients, and we assume that the scheme delivers:

$$\tilde\rho = \rho + \mathcal{O}(h^\kappa), \quad \partial_\alpha\tilde\rho = \partial_\alpha\rho + \mathcal{O}(h^\xi). \tag{3.68}$$

For these approximations, the first two terms in the brackets of Equation 3.67 become:

$$\begin{aligned}&2\,\frac{c\,\tilde\rho^\gamma}{\tilde\rho^2}\partial_\beta\rho - 2\,\frac{\rho c\,\tilde\rho^\gamma}{\tilde\rho^3}\partial_\alpha\tilde\rho\\ &= 2\,c\,\rho^{\gamma-2}\Big(1+\mathcal{O}(h^\kappa)\Big)^{\gamma-2}\partial_\beta\rho - 2\,c\,\rho^{\gamma-2}\Big(1+\mathcal{O}(h^\kappa)\Big)^{\gamma-3}\partial_\beta\rho\Big(1+\mathcal{O}(h^\xi)\Big)\\ &= 2\,c\,\rho^{\gamma-2}\partial_\beta\rho\,\Big[\Big(1+\mathcal{O}(h^\kappa)\Big)^{\gamma-2} - \Big(1+\mathcal{O}(h^\kappa)\Big)^{\gamma-3}\Big(1+\mathcal{O}(h^\xi)\Big)\Big]\\ &\approx 2\,c\,\rho^{\gamma-2}\partial_\beta\rho\,\Big[\Big(1+(\gamma-2)\,\mathcal{O}(h^\kappa)\Big) - \Big(1+(\gamma-3)\,\mathcal{O}(h^\kappa)\Big)\Big(1+\mathcal{O}(h^\xi)\Big)\Big]\\ &= \mathcal{O}(h^{\min(\kappa,\xi)}).\end{aligned} \tag{3.69}$$

In the approximation involved above, we used the two first terms of the binomial series $(1+z)^\theta = 1 + \theta z + ...$, which converges for $|z| < 1$. The previous analysis also holds for the case that $P = c\rho^\gamma - 1$. The term involving unity is represented by considering $\gamma = 0$ and $c = 1$ in the equations above. It still gives the same result. The third term in the brackets of Equation 3.67 reads:

$$\begin{aligned}&\frac{\rho}{\tilde\rho^2}\frac{\partial P(\tilde\rho)}{\partial\tilde\rho}\tilde\partial_\beta\rho = c\,\gamma\,\rho\tilde\rho^{\gamma-3}\tilde\partial_\beta\rho = c\,\gamma\,\rho^{\gamma-2}\Big(1+\mathcal{O}(h^\kappa)\Big)^{\gamma-3}\partial_\beta\rho\Big(1+\mathcal{O}(h^\xi)\Big)\\ &\quad\approx c\,\gamma\,\rho^{\gamma-2}\partial_\beta\rho\,\Big(1+(\gamma-3)\mathcal{O}(h^\kappa)\Big)\,\Big(1+\mathcal{O}(h^\xi)\Big) = \frac{1}{\rho}\partial_\beta P(\rho) + \mathcal{O}(h^{\min(\kappa,\xi)}).\end{aligned} \tag{3.70}$$

Regarding the very last term of Equation 3.67:

$$\frac{P\,\rho}{\tilde{\rho}^2} = \frac{c\,\rho\,\tilde{\rho}^\gamma}{\tilde{\rho}^2} = c\,\rho^{\gamma-1}\Big(1+\mathcal{O}(h^\kappa)\Big), \tag{3.71}$$

and therefore we may deduce that:

$$-\int_\Omega \left(\frac{P}{\tilde{\rho}^2}\Big|_{(x)} + \frac{P}{\tilde{\rho}^2}\Big|_{(y)}\right)\partial_\alpha W(x-y)\,\mathrm{d}\mu(y) = -\frac{1}{\rho}\partial_\beta P(\rho)\,\Lambda_{\beta\alpha} - 2\frac{P}{\rho}K_\alpha, \tag{3.72}$$

for equations of state of the form $P(\rho) = c\rho^\gamma$ or $P(\rho) = c\rho^\gamma - 1$, up to $\mathcal{O}(h)$-terms.

3.4.2 Volume-smoothed medium

In the derivation of the corresponding equation of mass conservation (Section 3.3.2), a complication appears, which is resolved by assuming that $\delta\tilde{\rho} = \delta\rho + \mathcal{O}(h^\xi)$, for $\xi \geq 0$. Here, we prove the validity of this assumption.

Consider the continuity equation of the volume-smoothed medium (3.51):

$$\begin{aligned}
\frac{\mathrm{d}\tilde{\rho}}{\mathrm{d}t}\Big|_{(x)} &= \tilde{\rho}(x)\int_\Omega \partial_\alpha W(x-y)\Big(v_\alpha(x) - v_\alpha(y)\Big)\frac{\mathrm{d}\mu}{\tilde{\rho}}\Big|_{(y)} \\
&= \tilde{\rho}(x)\Big[\,v_\alpha(x)\int_\Omega \frac{\rho}{\tilde{\rho}}\Big|_{(y)}\partial_\alpha W(x-y)\,\mathrm{d}\lambda(y) \\
&\quad - \int_\Omega \frac{\rho\,v_\alpha}{\tilde{\rho}}\Big|_{(y)}\partial_\alpha W(x-y)\,\mathrm{d}\lambda(y)\Big],
\end{aligned}$$

which provides the up to $\mathcal{O}(h)$-terms approximation:

$$\begin{aligned}
\frac{\mathrm{d}\tilde{\rho}}{\mathrm{d}t}\Big|_{(x)} &\approx \tilde{\rho}\left\{v_\alpha\Big[\frac{\rho}{\tilde{\rho}}\,K_\alpha + \partial_\beta\Big(\frac{\rho}{\tilde{\rho}}\Big)\,\Lambda_{\beta\alpha}\Big] - \Big[\frac{\rho\,v_\alpha}{\tilde{\rho}}\,K_\alpha + \partial_\beta\Big(\frac{\rho\,v_\alpha}{\tilde{\rho}}\Big)\,\Lambda_{\beta\alpha}\Big]\right\} \\
&= \tilde{\rho}\left[v_\alpha\,\partial_\beta\Big(\frac{\rho}{\tilde{\rho}}\Big) - \partial_\beta\Big(\frac{\rho\,v_\alpha}{\tilde{\rho}}\Big)\right]\Lambda_{\beta\alpha} = -\rho\,\partial_\beta v_\alpha\,\Lambda_{\beta\alpha}.
\end{aligned} \tag{3.73}$$

Therefore, indeed the residual terms are at most $\mathcal{O}(h)$ and the convergence of $\delta\tilde{\rho}$ as well, considering time as a parameter. Regarding the corresponding equation of motion, the approximation is:

$$\begin{aligned}
\frac{\mathrm{d}v_\alpha}{\mathrm{d}t}\Big|_{(x)} &= -\int_\Omega\left(\frac{P(x)+P(y)}{\tilde{\rho}(x)\,\tilde{\rho}(y)}\right)\partial_\alpha W(x-y)\,\mathrm{d}\mu(y) \\
&= -\frac{P}{\tilde{\rho}}\Big|_{(x)}\int_\Omega \frac{1}{\tilde{\rho}}\Big|_{(y)}\partial_\alpha W(x-y)\,\mathrm{d}\mu(y) - \frac{1}{\tilde{\rho}(x)}\int_\Omega \frac{P}{\tilde{\rho}}\Big|_{(y)}\partial_\alpha W(x-y)\,\mathrm{d}\mu(y) \\
&= -\frac{P}{\tilde{\rho}}\Big|_{(x)}\int_\Omega \frac{\rho}{\tilde{\rho}}\Big|_{(y)}\partial_\alpha W(x-y)\,\mathrm{d}\lambda(y) - \frac{1}{\tilde{\rho}(x)}\int_\Omega \frac{P\,\rho}{\tilde{\rho}}\Big|_{(y)}\partial_\alpha W(x-y)\,\mathrm{d}\lambda(y),
\end{aligned}$$

and up to $\mathcal{O}(h)$-terms:

$$\begin{aligned}\frac{\mathrm{d}v_\alpha}{\mathrm{d}t}\Big|_{(x)} &\approx -\frac{P}{\tilde{\rho}}\Big[\frac{\rho}{\tilde{\rho}}K_\alpha + \partial_\beta\Big(\frac{\rho}{\tilde{\rho}}\Big)\Lambda_{\beta\alpha}\Big] - \frac{1}{\tilde{\rho}}\Big[\frac{P\rho}{\tilde{\rho}}K_\alpha + \partial_\beta\Big(\frac{P\rho}{\tilde{\rho}}\Big)\Lambda_{\beta\alpha}\Big] \\ &= -\Big[\frac{P}{\tilde{\rho}}\partial_\beta\Big(\frac{\rho}{\tilde{\rho}}\Big) + \frac{1}{\tilde{\rho}}\partial_\beta\Big(\frac{P\rho}{\tilde{\rho}}\Big)\Big]\Lambda_{\beta\alpha} - 2\frac{P\rho}{\tilde{\rho}^2}K_\alpha \\ &= -\Big[2\frac{P}{\tilde{\rho}}\partial_\beta\Big(\frac{\rho}{\tilde{\rho}}\Big) + \frac{\rho}{\tilde{\rho}^2}\partial_\beta P\Big]\Lambda_{\beta\alpha} - 2\frac{P\rho}{\tilde{\rho}^2}K_\alpha \\ &= -\Big[2\frac{P}{\tilde{\rho}^2}\partial_\beta\rho - 2\frac{P\rho}{\tilde{\rho}^3}\partial_\beta\tilde{\rho} + \frac{\rho}{\tilde{\rho}^2}\partial_\beta P\Big]\Lambda_{\beta\alpha} - 2\frac{P\rho}{\tilde{\rho}^2}K_\alpha. \end{aligned} \tag{3.74}$$

The result is the same as in the equation of motion of the mass-smoothed medium (3.72) and consequently:

$$-\int_\Omega \left(\frac{P(x)+P(y)}{\tilde{\rho}(x)\,\tilde{\rho}(y)}\right)\partial_\alpha W(x-y)\,\mathrm{d}\mu(y) = -\frac{1}{\rho}\partial_\beta P(\rho)\,\Lambda_{\beta\alpha} - 2\frac{P\rho}{\tilde{\rho}^2}K_\alpha, \tag{3.75}$$

so that they converge in the same way.

3.4.3 Number-smoothed medium

The number-smoothed medium uses the counting measure as the building block for the corresponding smoothed density. The continuity equation of the number-based smoothing is:

$$\begin{aligned}\frac{\mathrm{d}\tilde{\rho}}{\mathrm{d}t}\Big|_{(x_i)} &= m(x_i)\sum_j \partial_\alpha W(x_i-x_j)\Big(v_\alpha(x_i)-v_\alpha(x_j)\Big) \\ &= \sum_j \partial_\alpha W(x_i-x_j)\Big(v_\alpha(x_i)-v_\alpha(x_j)\Big)\,\frac{m(x_i)}{m(x_j)}\int_{\Omega_j}\mathrm{d}\mu, \end{aligned} \tag{3.76}$$

In Equation 3.61, it is argued that an integral similar to the ones appearing here, converges to the corresponding equation of the mass-smoothed medium. Due to the same reasons, in the limit $N\to\infty$, the previous behaves similarly to the corresponding equation of the mass-smoothed medium, that is:

$$\frac{\mathrm{d}\tilde{\rho}}{\mathrm{d}t}\Big|_{(x_i)} = \Big(v_\alpha(x_i)\int_\Omega \partial_\alpha W(x_i-y)\,\mathrm{d}\mu(y) - \int_\Omega v_\alpha(y)\,\partial_\alpha W(x_i-y)\,\mathrm{d}\mu(y)\Big). \tag{3.77}$$

Since in this Section we are interested in the limit $h\to 0$, a relevant question is whether the two processes, $N\to\infty$ and $h\to 0$, occur simultaneously. Recalling that $W\equiv W_h$, as $N\to\infty$ for a relatively regular configuration of particles, the definition of the smoothing length (2.20) provides: $h=\eta\,\overline{n}^{-1/d}\approx\eta(\nu(\Omega^N)/\lambda(\Omega^N))^{-1/d} = \eta(N/\lambda(\Omega^N))^{-1/d}\to 0$. Hence, we may pass directly from Equation 3.76 to the $\mathcal{O}(h)$-terms approximation of Equation 3.66, also for the continuity equation of the number-smoothed medium. Using the same technique, it is shown that the corresponding equation of motion converges similarly to the equation of motion of the mass-smoothed medium (3.72).

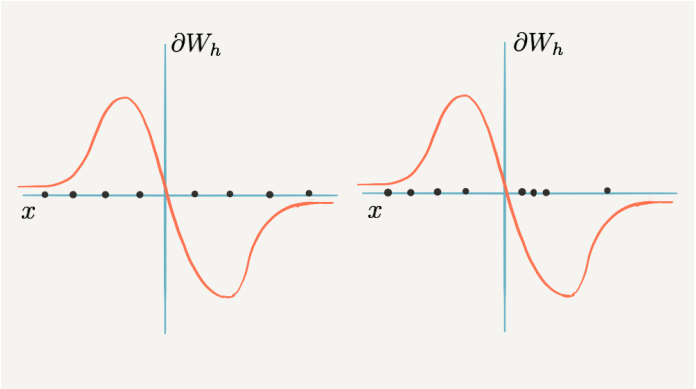

FIGURE 3.3: The effect of particle disorder in the calculation of the term Λ.

3.4.4 Discussion

The previous convergence analysis establishes that the equations of mass conservation of the smoothed media relate to the continuity equation of the classical medium as:

$$\frac{\mathrm{d}\tilde{\rho}}{\mathrm{d}t} = -\rho\,\partial_\beta v_\alpha\,\Lambda_{\beta\alpha}, \tag{3.78}$$

where $\tilde{\rho}$ is obtained with any of the three SPH schemes. The convergence is determined by the extent to which $\Lambda_{\alpha\beta} = \int_\Omega (x_\alpha - y_\alpha)\,\partial_\beta W(x-y)\,\mathrm{d}\lambda(y)$ takes its identity value $\delta_{\alpha\beta}$ in the discrete system, where

$$\Lambda^N_{\alpha\beta}(x_i) = \sum_j (x_{\beta,i} - x_{\beta,j})\,\partial_\alpha W(x_i - x_j)\,\lambda(\Omega_j) = \sum_j (x_{\beta,i} - x_{\beta,j})\,\partial_\alpha W(x_i - x_j)\frac{1}{n(x_j)}. \tag{3.79}$$

Obviously, in the discrete setting, the extent to which the identity holds relies on the particle configuration, via the terms $\|x_i - x_j\| \propto h$ and the local number density n. This is an evidence in support of [Monaghan, 2005], who concludes that the SPH error depends on the ordering of the particles, which in turn is an effect of the dynamics and therefore the equations themselves. The identity value of Λ is obtained due to the antisymmetry of the smoothing function. This is true in case of regular distributions, while for irregular distributions errors appear. In order to examine the scale of the errors, first consider the scale of Λ:

$$|\Lambda^N_{\alpha\beta}(x_i)| \approx \sum_j h\frac{1}{h^{d+1}}\frac{1}{n(x_j)} \approx \nu(\Omega_{h,i})\,h^{-d}\,\frac{1}{n} = h^{-d}\,\lambda(\Omega_{h,i}) = \mathcal{O}(1), \quad x_j \in \Omega_{h,i}, \tag{3.80}$$

with the help of Equation 2.19. From a qualitative point of view, this means that deviations from regularity in the particle configuration may induce errors of up to $\mathcal{O}(1)$. This behavior is expected for highly disordered configurations or close to

boundaries, where the support of the smoothing function is cut off. In order to envisage this scenario, consider a one-dimensional irregular particle configuration. These two cases are illustrated in Figure 3.3. The sum on the left of a particle is not equal to the opposite of the sum on the right of the particle and thus an imbalance occurs. This imbalance prevents Λ from taking its identity value.

Equivalently, for the motion equations of the smoothed media:

$$\frac{\mathrm{d}v_\alpha}{\mathrm{d}t} = -\frac{1}{\rho}\partial_\beta P(\rho)\,\Lambda_{\beta\alpha} - 2\frac{P}{\rho}K_\alpha, \tag{3.81}$$

where the identity value of K_α is zero, because of the antisymmetry of the kernel's derivative. Unlike the continuity equation, the K term remains and it scales as:

$$\begin{aligned} |K_\alpha^N(x_i)| &= \sum_j |\partial_\alpha W(x_i - x_j)|\lambda(\Omega_j) \approx \sum_j \frac{1}{h^{d+1}}\frac{1}{n(x_j)} \approx \nu(\Omega_{h,i})\,h^{-(d+1)}\,\frac{1}{\overline{n}} \\ &= h^{-(d+1)}\,\lambda(\Omega_{h,i}) = \mathcal{O}(h^{-1}), \quad x_j \in \Omega_{h,i}, \end{aligned} \tag{3.82}$$

recalling the average number density (2.19). Whence, for strongly disordered configurations or close to boundaries, errors may reach $\mathcal{O}(h^{-1})$. Therefore, in those cases the motion equation of the smoothed medium diverges locally from the equation of motion of the classical medium.

Note that the conservation properties of the scheme in the discrete setting are intact and as a matter of fact, they are guaranteed by the variational principle which they originate from.

For a comment on the dynamics of the situation above, let us consider an initial well-ordered particle configuration. If the neighbors of the particle i start moving closer to it, more particles enter within its h-neighborhood and thus the sampling increases and the estimate tends to be better; the ordering plays a less significant role. On the other hand, if the neighbors of the particle i start moving apart from it, less particles remain within the h-neighborhood and thus the estimate tends to worsen. Consequently, the ordering starts playing a very crucial role. This may explain why SPH is prone to instabilities when high tensile forces appear during the computation.

The relevant literature offers a way to counteract the effects of the K-term. Using Newtonian mechanics, one may develop the motion equation:

$$-\frac{1}{\rho(x)}\partial_\alpha P(x) = -\int_\Omega \left(\frac{P(x)-P(y)}{\tilde{\rho}(x)\,\tilde{\rho}(y)}\right)\partial_\alpha W(x-y)\,\mathrm{d}\mu(y) = -\frac{1}{\rho}\partial_\beta P(\rho)\,\Lambda_{\beta\alpha}, \tag{3.83}$$

based on a better approximation of $\partial_\alpha P$, according to Section 2.4. This estimate converges locally to the equations of the classical medium, since K is absent. However, it is not consistent with the variational framework and therefore, this equation of motion cannot guarantee the conservation of global momentum in the relevant processes. Price [2012] underlines that —provided a regular particle distribution— such formulations are going to be more accurate for linear or weakly non-linear problems,

as those run for a short time and/or are not involving strong shocks. Conversely, formulations based on variational methods are able to treat processes with strong non-linearites —such as shocks— and offer long-term stability, due to the global conservation of momentum and energy. Paradoxically, SPH defies local convergence to guarantee conservation.

3.5 Non-ideal media

The previous sections dealt with ideal media, according to $e = e(\rho)$ and assuming isentropic conditions. This behavior is typically encountered in gases, which respond to mechanical loading by changes of the volume of their infinitesimal parts. Liquid and solid media are more prone to respond with a change of the shape of their infinitesimal parts, which is described by the *distortions*:

$$x_{\alpha\beta} := \partial_{0\beta} x_\alpha. \tag{3.84}$$

They implicitly appear in the definition of the Jacobian (3.32) and they describe an affine deformation of the medium's shape in the neighborhood of x_0 [Berdichevsky, 2009, Ch.3].

3.5.1 General equations of motion

Considering $e = e(x_{\alpha\beta}, s)$, the conjugate thermodynamic tensions of the distortions are the total stresses, described by the elements $\pi_{\alpha\beta}$ of the *Piola-Kirchhoff stress tensor* [Berdichevsky, 2009, Ch.3]:

$$\left.\frac{\partial e}{\partial x_{\alpha\beta}}\right|_s := \frac{\pi_{\alpha\beta}}{\rho_0} = \frac{\sigma_{\alpha\gamma} J_{\gamma\beta}}{\rho_0}, \tag{3.85}$$

or alternatively with the help of the *Cauchy stress tensor*: $\sigma_{\alpha\gamma} = x_{\gamma\beta}\pi_{\alpha\beta}\,\rho/\rho_0$. Emphasis should be given to the second index of the Piola-Kirchhoff stress tensor, which pertains to the reference configuration of the medium, unlike the indices of the Cauchy stress tensor, which both refer to the current configuration [Berdichevsky, 2009, Ch.4]. The identity $x_{\gamma\theta} J_{\gamma\beta} = \delta_{\beta\theta} J$, so that $J_{\gamma\beta} = J/x_{\gamma\beta}$, proves useful for completing the transformation [Seliger and Whitham, 1968].

Distortions are the only way for the medium to respond mechanically. Let aside any other response of the system —chemical, electromagnetic etc.— and additionally assume that there is no heat conduction from one part of the medium to another. The latter assumption is true in two cases: either the heat produced within each of the medium's infinitesimal parts is uniform or the changes are so fast that there is no time for heat to conduct. Thus heat —created from internal friction due to the distortions— remains within the medium's infinitesimal parts and contributes exclusively to the increase of the local temperature.

The equation of motion is in any case the result of the distortions, while for the description of the medium's thermodynamic state, the calculation of changes in entropy are necessary as well. Thus, we first derive the equations under isentropic conditions, taking into account all distortions, and afterwards, we study how distortions trigger entropy changes in some specific cases.

Classical equations The variation of energy in Equation 3.85 is:

$$\delta e = \frac{\partial e}{\partial x_{\alpha\beta}} \delta x_{\alpha\beta} = \frac{\sigma_{\alpha\gamma} J_{\gamma\beta}}{\rho_0} \delta\Big(\partial_{0\beta} x_\alpha\Big) = \frac{\sigma_{\alpha\gamma} J_{\gamma\beta}}{\rho_0} \partial_\beta\Big(\delta x_\alpha\Big) = \frac{\sigma_{\alpha\gamma}}{\rho} \partial_\gamma\Big(\delta x_\alpha\Big). \tag{3.86}$$

It leads to the energy functional:

$$\begin{aligned}
\delta\mathcal{E}\Big|_{t_0}^{t_1} &= \int_{t_0}^{t_1} \int_\Omega \delta e \,\mathrm{d}\mu \,\mathrm{d}t = \int_{t_0}^{t_1} \int_\Omega \frac{\sigma_{\alpha\beta}}{\rho} \partial_\beta\Big(\delta x_\alpha\Big) \rho \,\mathrm{d}\lambda \,\mathrm{d}t = \\
&= \int_{t_0}^{t_1} \int_\Omega \partial_\beta\Big(\sigma_{\alpha\beta} \delta x_\alpha\Big) \,\mathrm{d}\lambda \,\mathrm{d}t - \int_{t_0}^{t_1} \int_\Omega \partial_\beta \sigma_{\alpha\beta} \delta x_\alpha \,\mathrm{d}\lambda \,\mathrm{d}t = \\
&= \int_{t_0}^{t_1} \int_{\partial\Omega} \Big[\sigma_{\alpha\beta} \delta x_\alpha\Big]_{\partial\Omega} \zeta_\beta \,\mathrm{d}\Gamma \,\mathrm{d}t - \int_{t_0}^{t_1} \int_\Omega \partial_\beta \sigma_{\alpha\beta} \delta x_\alpha \,\mathrm{d}\lambda \,\mathrm{d}t = \\
&= -\int_{t_0}^{t_1} \int_\Omega \frac{1}{\rho} \partial_\beta \sigma_{\alpha\beta} \delta x_\alpha \,\mathrm{d}\mu \,\mathrm{d}t,
\end{aligned} \tag{3.87}$$

taking into account that $\delta x_\alpha|_{\partial\Omega} = 0$ and $\delta x_\alpha|_{t_0}^{t_1} = 0$. Casting the result into Equation 3.23 delivers the equation of motion:

$$\frac{\mathrm{d}v_\alpha}{\mathrm{d}t} = \frac{\partial_\beta \sigma_{\alpha\beta}}{\rho}, \tag{3.88}$$

or in the equivalent form [Seliger and Whitham, 1968]:

$$\frac{\mathrm{d}v_\alpha}{\mathrm{d}t} = \frac{1}{\rho_0} \partial_\beta \pi_{\alpha\beta}, \tag{3.89}$$

which employs a derivative with respect to the initial configuration. The difference between the two formulations pertains to the reference configuration of the medium used. The former equation employs the updated Lagrangian description, while the latter used the total Lagrangian description (see Section 3.1).

Smoothed equations – Introduction The first effort to introduce deviatoric elastic stresses in SPH is by Libersky et al. [1993], albeit the resulting equations are variationally inconsistent. The problems tackled refer to high-strain deformation of solids and the updated Lagrangian description is then —naturally— incorporated. A variational approach is employed by Bonet and Kulasegaram [2000], which is applied to the discrete system and arrives to a formula which misses one of the two terms that are customary in the SPH equations for the deviatoric stresses. That second term guarantees the conservation of momentum. In a prior paper by Bonet and Lok [1999],

the second term appears, although the derivation details are not clear. Finally, the SPH equations for the total Lagrangian description are based on ideas of Rabczuk et al. [2004] and also employed by Vignjevic et al. [2006]. They are developed with conventional derivation strategies. In what follows we derive the SPH equations for the deviatoric stresses, based on the framework developed in Chapter 3.

Notably, we see that the classical equations for both descriptions —updated and total Lagrangian— are derived from the same formula of the variation of energy. For the smoothed equations, the equations for the two descriptions follow from the construction of two different estimates.

Smoothed equations – Total Lagrangian description In Section 3.1, we point out that the variation of energy for the smoothed equations involves the smoothing of the thermodynamic substate variables. Additionally, the total Lagrangian description typically employs the first Piola-Kirchhoff stress tensor. Therefore, the variation of the internal energy of media with total stress response (3.85):

$$\delta e = \frac{\pi_{\alpha\beta}}{\rho_0}\delta x_{\alpha\beta}, \tag{3.90}$$

requires the construction of the *smoothed distortions* in order to calculate $\delta\hat{x}_{\alpha\beta}$. The smoothings pertain to the reference domain Ω_0 and therefore we retrieve the notation $\hat{x}_{\alpha\beta}$ from Section 2.3 and continue accordingly with the smoothed distortions:

$$\hat{x}_{\alpha\beta} = \int_{\Omega_0} (y_\alpha - x_\alpha)\partial_\beta \hat{W}(x_0 - y_0)\,\mathrm{d}\lambda(y_0), \tag{3.91}$$

and their variations:

$$\delta\hat{x}_{\alpha\beta} = \int_{\Omega_0} (\delta y_\alpha - \delta x_\alpha)\partial_\beta \hat{W}(x_0 - y_0)\,\mathrm{d}\lambda(y_0). \tag{3.92}$$

Note that in the reference domain, $\mathrm{d}\lambda$ does not involve an approximation; it is the result of the initial partitioning of the domain. The energy functional:

$$\begin{aligned}
\delta\mathcal{E}|_{t_0}^{t_1} &= \int_{t_0}^{t_1}\int_\Omega \delta e\,\mathrm{d}\mu\,\mathrm{d}t = \int_{t_0}^{t_1}\int_{\Omega_0} \frac{\pi_{\alpha\beta}(x)}{\rho_0(x_0)}\delta\hat{x}_{\alpha\beta}\,\mathrm{d}\mu_0(x)\,\mathrm{d}t = \\
&= \int_{t_0}^{t_1}\int_\Omega \frac{\pi_{\alpha\beta}(x)}{\rho_0(x_0)}\int_{\Omega_0}(\delta y_\alpha - \delta x_\alpha)\partial_\beta\hat{W}(x_0 - y_0)\,\mathrm{d}\lambda(y_0)\,\mathrm{d}\mu_0(x_0)\,\mathrm{d}t = \\
&= \int_{t_0}^{t_1}\int_{\Omega_0} \pi_{\alpha\beta}(x)\int_{\Omega_0}(\delta y_\alpha - \delta x_\alpha)\partial_\beta\hat{W}(x_0 - y_0)\,\frac{\mathrm{d}\mu_0(y_0)}{\rho_0(y_0)}\,\frac{\mathrm{d}\mu_0(x_0)}{\rho_0(x_0)}\,\mathrm{d}t = \\
&= \int_{t_0}^{t_1}\int_\Omega\int_{\Omega_0} \frac{1}{\rho_0(x_0)}\Big(\pi_{\alpha\beta}(x) + \pi_{\alpha\beta}(y)\Big)\partial_\beta\hat{W}(x_0 - y_0)\,\mathrm{d}\lambda(y_0)\,\delta x_\alpha\,\mathrm{d}\mu(x)\,\mathrm{d}t,
\end{aligned} \tag{3.93}$$

provides the equation of motion:

$$\frac{\mathrm{d}v_\alpha}{\mathrm{d}t}\Big|_{(x)} = \frac{1}{\rho_0(x_0)}\int_{\Omega_0}\Big(\pi_{\alpha\beta}(x) + \pi_{\alpha\beta}(y)\Big)\partial_\beta\hat{W}(x_0 - y_0)\,\mathrm{d}\lambda(y_0), \tag{3.94}$$

and the evolution of internal energy:

$$\frac{\mathrm{d}e}{\mathrm{d}t}\Big|_{(x)} = \frac{\pi_{\alpha\beta}(x)}{\rho_0(x_0)}\frac{\mathrm{d}\hat{x}_{\alpha\beta}}{\mathrm{d}t}. \tag{3.95}$$

In the previous, $\mathrm{d}\hat{x}_{\alpha\beta}/\mathrm{d}t$ is constructed from Equation 3.92, considering a temporal variation. Notice that in all the equations above, the use of the Piola-Kirchhoff stress tensor can be bypassed in favor of the Cauchy stress tensor, by employing the smooth estimates of the Jacobian elements $\pi_{\alpha\beta} \approx \sigma_{\alpha\gamma}\hat{J}_{\alpha\gamma}$.

Smoothed equations – Updated Lagrangian description In case the problem is described in the current frame of reference, another SPH scheme is developed. For the classical equation we wrote:

$$\delta e = \frac{\sigma_{\alpha\beta}}{\rho}\partial_\beta\Big(\delta x_\alpha\Big). \tag{3.96}$$

The construction of the corresponding gradient starts by considering the smoothed variation:

$$\widetilde{\Big(\delta x_\alpha\Big)} = \int_\Omega \Big(\delta y_\alpha - \delta x_\alpha\Big) W(x-y)\frac{\mathrm{d}\mu(y)}{\tilde{\rho}(y)}, \tag{3.97}$$

which obtains the gradient:

$$\widetilde{\partial_\beta\Big(\delta x_\alpha\Big)} = \int_\Omega \Big(\delta y_\alpha - \delta x_\alpha\Big)\partial_\beta W(x-y)\frac{\mathrm{d}\mu(y)}{\tilde{\rho}(y)}, \tag{3.98}$$

and results in the variation of energy:

$$\begin{aligned}
\delta\mathcal{E}\big|_{t_0}^{t_1} &= \int_{t_0}^{t_1}\int_\Omega \delta e\,\mathrm{d}\mu\,\mathrm{d}t = \int_{t_0}^{t_1}\int_\Omega \frac{\sigma_{\alpha\beta}}{\rho}\delta\tilde{x}_{\alpha\beta}\,\mathrm{d}\mu\,\mathrm{d}t = \\
&= \int_{t_0}^{t_1}\int_\Omega \frac{\sigma_{\alpha\beta}}{\rho}\bigg|_{(x)}\int_\Omega \Big(\delta x_\alpha - \delta y_\alpha\Big)\partial_\beta W(x-y)\frac{\mathrm{d}\mu(y)}{\tilde{\rho}(y)}\,\mathrm{d}\mu(x)\,\mathrm{d}t = \\
&= \int_{t_0}^{t_1}\int_\Omega\int_\Omega \left(\frac{\sigma_{\alpha\beta}(x)}{\rho(x)\,\rho(y)} + \frac{\sigma_{\alpha\beta}(y)}{\rho(y)\,\rho(x)}\right)\partial_\beta W(x-y)\,\mathrm{d}\mu(y)\,\delta x_\alpha\,\mathrm{d}\mu(x)\,\mathrm{d}t.
\end{aligned} \tag{3.99}$$

Apparently, the density comes from a smoothing and thus:

$$\frac{\mathrm{d}v_\alpha}{\mathrm{d}t}|_{(x)} = \int_\Omega \frac{1}{\tilde{\rho}(x)\,\tilde{\rho}(y)}\Big(\sigma_{\alpha\beta}(x) + \sigma_{\alpha\beta}(y)\Big)\partial_\beta W(x-y)\,\mathrm{d}\mu(y) \tag{3.100}$$

is the equation of motion for the medium, with reference to the current configuration. Finally, the evolution of energy:

$$\frac{\mathrm{d}e}{\mathrm{d}t} = \frac{\sigma_{\alpha\beta}}{\tilde{\rho}}\partial_\beta\tilde{v}_\alpha \tag{3.101}$$

is readily available by introducing a temporal variation.

Discussion Given the relation:

$$\frac{\partial e(x_{\alpha\beta})}{\partial x_{\alpha\gamma}} = \frac{\sigma_{\alpha\beta} J_{\beta\gamma}}{\rho_0}, \tag{3.102}$$

it becomes evident that $\sigma_{\alpha\beta}$ is not a freely chosen function. Any model for $\sigma_{\alpha\beta}$, which is coupled to the derived equation of motion, should respect that $\sigma_{\alpha\beta} = \sigma_{\alpha\beta}(x_{\alpha\beta})$. If this is not the case, the system obtains a *pseudo-variational structure*. By that, we refer to schemes for which the equation of motion is derived via the variational procedure of the previous section, based on the functional relation $e = e(x_{\alpha\beta})$. The stresses are calculated autonomously without necessarily abiding to the functional relation $\sigma_{\alpha\beta} = \sigma_{\alpha\beta}(x_{\alpha\beta})$. As it is exhibited in the preceding section, these schemes only take a truly variational form for elastic media.

3.5.2 Elastic media

Regarding elastic media, the functional relation $e = e(x_{\alpha\beta})$ upon which the general equation of motion is based, is deceptive. That is because it implies changes in the internal energy even for rigid rotations of the medium [Seliger and Whitham, 1968]. It is, then, more appropriate to consider $e = e(\epsilon_{\alpha\beta})$, where for the *infinitesimal* or *linear strain theory* [Berdichevsky, 2009, Ch.6], the *displacements* u_α define the *strains*:

$$\epsilon_{\alpha\beta} = \frac{1}{2}\left(\frac{\partial u_\alpha}{\partial x_{0\beta}} + \frac{\partial u_\beta}{\partial x_{0\alpha}}\right) \approx \frac{1}{2}\left(\frac{\partial u_\alpha}{\partial x_\beta} + \frac{\partial u_\beta}{\partial x_\alpha}\right), \quad u_\alpha := x_\alpha - x_{0\alpha}, \tag{3.103}$$

and additionally, for isotropic materials $\epsilon_{\alpha\beta} = \epsilon_{\beta\alpha}$. Since $\epsilon_{\alpha\beta} = x_{\alpha\beta} - \delta_{\alpha\beta}$, it follows that:

$$\delta e = \frac{\partial e}{\partial \epsilon_{\alpha\beta}} \frac{\partial \epsilon_{\alpha\beta}}{\partial x_{\alpha\beta}} \delta x_{\alpha\beta} = \frac{\partial e}{\partial x_{\alpha\beta}} \delta x_{\alpha\beta} = \frac{\sigma_{\alpha\beta}}{\rho}\Big(\delta x_\alpha\Big) \tag{3.104}$$

and the resulting equation of motion coincides with the one of the previous section.

In light of the previous discussion, about $\sigma_{\alpha\beta}$ not being a freely chosen function, the stresses are modeled as:

$$\sigma_{\alpha\beta} = \lambda \epsilon_{\gamma\gamma} \delta_{\alpha\beta} + 2\mu \epsilon_{\alpha\beta}, \tag{3.105}$$

and hence they indeed are functions of $x_{\alpha\beta}$. This is not true for general models of $\sigma_{\alpha\beta}$ and attention should be paid on the stress models used, so that the final system of equations is variationally consistent.

3.5.3 Dissipative media

All equations of motion derived above only correspond to isentropic conditions, neglecting dissipative processes, such as viscous stresses in fluid media or plastic

stresses in solid media. According to the thermodynamic modeling of Section 3.1, when dissipative effects appear, in addition to distortions, entropy s is required for the description of the thermodynamic state of the medium.

In this case the equation of motion cannot be derived from a variational principle, but a *variational equation* instead. Berdichevsky [2009], Ch.3, explains this procedure for the static case; the extension to the dynamic case is straightforward. After introducing the dissipation potential $D = D(t, v_\alpha)$, the variational equation:

$$\frac{\delta L}{\delta x_\alpha} = -\frac{\delta D}{\delta v_\alpha}, \tag{3.106}$$

delivers the equation of motion:

$$\frac{\mathrm{d}v_\alpha}{\mathrm{d}t} - \frac{\delta e}{\delta x_\alpha} = -\frac{\partial D}{\partial v_\alpha}. \tag{3.107}$$

A variational equation is different from a variational principle in the sense that it does not describe a *law of nature*, "but rather a way to obtain a model with simply controlled mathematical features" [Berdichevsky, 2009, Ch.3]. Rather than looking for a stationary point of the action $\mathcal{S} = \int_T L\,\mathrm{d}t$, we are setting a constraint to the minimization of the action $\mathcal{S}$, by asking for the two processes to follow paths of the same steepness, each one according to their variables. What remains, is to define a dissipative potential[4] describing the desired properties of the medium.

For the definition of the internal energy e of the ideal medium, $\tilde{\rho}$ replaces ρ in Section 3.3. In the same way, the dissipative potential $D = D(\mathrm{e}_{\alpha\beta})$ employs the smooth estimates of the velocity components $\tilde{v}_\alpha$, in order to define the strain rate:

$$\mathrm{e}_{\alpha\beta} \equiv \frac{1}{2}\Big(\partial_\beta \tilde{v}_\alpha + \partial_\alpha \tilde{v}_\beta\Big). \tag{3.108}$$

For an isotropic medium ($\partial_\beta \tilde{v}_\alpha = \partial_\alpha \tilde{v}_\beta$), the latter provides:

$$\frac{\partial D}{\partial v_\alpha} = \frac{\partial D}{\partial \mathrm{e}_{\alpha\beta}} \frac{\partial \mathrm{e}_{\alpha\beta}}{\partial v_\alpha} = \partial_\beta \left(\frac{\partial D}{\partial \mathrm{e}_{\alpha\beta}} \right). \tag{3.109}$$

In the following, this modeling choice is specified for the description of the viscous response of fluid media and the plastic response of solid media.

Viscous compressible medium Regarding the viscous response of fluid media, the usual assumption is that the dissipative potential defines the viscous stresses $\tau_{\alpha\beta}$, which in turn are functions of the strain rates:

$$\frac{\partial D}{\partial \mathrm{e}_{\alpha\beta}} \equiv \frac{\tau_{\alpha\beta}}{\lambda} = \mathrm{e}_{\gamma\gamma}\delta_{\alpha\beta} + 2\frac{\mu_{\mathrm{vsc}}}{\lambda}\mathrm{e}_{\alpha\beta}, \tag{3.110}$$

[4] [Berdichevsky, 2009, Ch.3] makes a distinction between the dissipative potential and the dissipation function. In the cases studied here, they only differ by the multiplication with a constant.

for the viscosity μ_{vsc} and the bulk viscosity λ. It follows that:

$$\frac{\partial D}{\partial v_\alpha} = \partial_\beta \mathrm{e}_{\gamma\gamma}\delta_{\alpha\beta} + 2\frac{\mu_{\text{vsc}}}{\lambda}\partial_\beta \mathrm{e}_{\alpha\beta} = \partial_{\gamma\alpha} v_\gamma \delta_{\alpha\beta} + 2\frac{\mu_{\text{vsc}}}{\lambda}\partial_{\beta\beta} v_\alpha, \tag{3.111}$$

and therefore the equation of motion is complete, according to Equation 3.107.

Therefore, based on v_α, it is necessary to construct smoothed estimates of the Laplacian $\partial_{\beta\beta}\tilde{v}_\alpha$ and the gradient of the divergence $\partial_{\gamma\alpha}\tilde{v}_\gamma$. Price [2012] discusses various options.

Elastic-plastic medium Solid media respond elastically only up to a certain strain and then plastic deformation starts. The following covers the *linear strain theory*, where strains are considered to be small so that the deformation rates equal the strain rates ($\dot{\epsilon}_{\alpha\beta} \approx \mathrm{e}_{\alpha\beta}$). This is typically connected to the updated Lagrangian formulation, for deformation states which are "close" to each other.

Plastic deformation has two main characteristics: first, it is a dissipative process and second, it is a history-dependent process. The latter implies that the deformations producing it are not unique. Nevertheless, the strain rates (equivalent to the deformation rates in the linear regime) leading to the deformed state can be considered as unique and therefore the decomposition:

$$\mathrm{e}_{\alpha\beta} = \mathrm{e}^{(e)}_{\alpha\beta} + \mathrm{e}^{(p)}_{\alpha\beta}, \tag{3.112}$$

holds. Additionally, in the *theory of perfect plasticity* it is assumed that $\mathrm{e}_{\alpha\beta} \approx \mathrm{e}^{(p)}_{\alpha\beta}$. Eventually, the dissipative potential is defined as:

$$D = \begin{cases} 0, & \mathcal{G}(\sigma_{\alpha\beta}) < Y_0, \\ D(\mathrm{e}^{(p)}_{\alpha\beta}), & \mathcal{G}(\sigma_{\alpha\beta}) \geq Y_0. \end{cases} \tag{3.113}$$

The internal energy becomes the branched function:

$$e = \begin{cases} e(\epsilon_{\alpha\beta}), & \mathcal{G}(\sigma_{\alpha\beta}) < Y_0, \\ e(\epsilon_{\alpha\alpha}, s), & \mathcal{G}(\sigma_{\alpha\beta}) \geq Y_0, \end{cases} \tag{3.114}$$

where $\mathcal{G} = \mathcal{G}(\sigma_{\alpha\beta})$ is the *yield function*, a criterion for the transition from the elastic regime to the plastic regime, and Y_0 the material's yield strength. The *Von Mises* plasticity model [Berdichevsky, 2009, Ch.3] assumes that plastic deformation is an incompressible process, implying that $D = D(\mathrm{e}'^{(p)}_{\alpha\beta})$, where the deviatoric part of the strain rate is:

$$\mathrm{e}'_{\alpha\beta} = \mathrm{e}_{\alpha\beta} - \frac{1}{3}\mathrm{e}_{\gamma\gamma}\,\delta_{\alpha\beta}. \tag{3.115}$$

Furthermore, it postulates that $D = Y_0\sqrt{\mathrm{e}'^{(p)}_{\alpha\beta}\,\mathrm{e}'^{(p)}_{\alpha\beta}}$ and consequently:

$$\frac{\partial D}{\partial \mathrm{e}'^{(p)}_{\alpha\beta}} \equiv \frac{\tau_{\alpha\beta}}{\lambda} = \frac{Y_0^2}{\sqrt{\mathrm{e}'^{(p)}_{\gamma\delta}\,\mathrm{e}'^{(p)}_{\gamma\delta}}}\,\mathrm{e}'^{(p)}_{\alpha\beta}, \tag{3.116}$$

usually for $\lambda = 1$. According to Equation 3.109, this definition of the differential leads to:

$$\frac{\partial D}{\partial v_\alpha} = \partial_\beta \left(\frac{\partial D}{\partial e'^{(p)}_{\alpha\beta}} \right), \tag{3.117}$$

and requires a smooth estimate of the derivative of the deviator (3.116). This way of constructing the plasticity terms is not common in the SPH literature and possible merits or difficulties are yet to be discovered.

In the context of SPH, plasticity is typically introduced in another way. The deformation of the medium is described by the equations for elastic media and at each time step the yield criterion ($\mathcal{G} > 0$) is examined for each particle. If plastic flow is detected, the deviatoric stresses of that particle are assigned with the fixed limiting value. This procedure was pioneered by Libersky et al. [1993] and a detailed description follows in Chapter 6.

CHAPTER 4

The discrete SPH equations

The previous chapters deal with the derivation of the equations of smoothed media from principles of continuum mechanics and additionally, they delineate how these equations relate to the equations of classic media. The present chapter develops all the ingredients necessary to integrate the discretized equations in time, such that a long term stability is achieved. To this end, we discuss the following subjects: spatial adaptivity of the schemes, symplectic time integrators and dissipative terms for the accurate description of propagating discontinuities. Finally, we present novel numerical evidence of convergence of the SPH schemes as they approach the continuous equations.

4.1 Adaptive smoothing

In order to introduce variable resolution in the smoothing procedure, Equation 2.31 suggests a methodology based on the local number density, so that:

$$h(x_i) := \eta\, \tilde{n}(x_i)^{-1/d}. \tag{4.1}$$

Hence, the smoothing length changes in time and space, growing larger for sparsely populated regions and reducing in denser regions. Moreover, η is a scalar parameter[1]. Considering that the objective of turning h into a variable is to relate it to the local

[1] A vector-valued η can also offer advantages, not to be discussed in the present study; the reader is referred to Owen et al. [1998].

length scale in the neighborhood of a particle, another kind of adaptivity is devised:

$$h(x_i) = \eta\Big(\frac{m(x_i)}{\tilde{\rho}(x_i)}\Big)^{1/d}, \tag{4.2}$$

based on the definition of a volume around the particle. For the discrete system $\int_{\Omega_i} \mathrm{d}\lambda = \int_{\Omega_i} \mathrm{d}\mu/\rho(x_i) = m(x_i)/\rho(x_i) \approx m(x_i)/\tilde{\rho}(x_i)$, where m is the mass-per-particle density, which remains constant in time. Due to the definition of the number density (becomes infinite for the continuous system), this is a procedure only defined in the discrete system. Therefore, in the following we employ the discrete forms of the conservation equations.

The two formulae, (4.1) and (4.2), coincide if the number-density smoothing $\tilde{\rho}(x_i) = m(x_i)\,\tilde{n}(x_i)$ is used. Although the numerical tests in Chapter 5 reveal that the former relation is more appropriate, the latter one may be combined with any of the three types of smoothing.

In the following, on grounds of concise notation, all magnitudes appear with the index of the corresponding particle i, rather than writing them as functions of x_i.

For the mass smoothing (3.38), the calculation of density is coupled to the smoothing length:

$$\tilde{\rho}_i = \sum_j W(x_i - x_j, h_i)\, m_j, \quad h_i = \eta\Big(\frac{m_i}{\tilde{\rho}_i}\Big)^{1/d}, \tag{4.3}$$

and gives the variation:

$$\begin{aligned}\delta\tilde{\rho}_i &= \sum_j \partial_\alpha W(x_i - x_j, h_i)\,\Big(\delta x_{\alpha,i} - \delta x_{\alpha,j}\Big)\, m_j \\ &= \sum_j \partial_\alpha W(x_i - x_j, h_i)\,\Big(\delta x_{\alpha,i} - \delta x_{\alpha,j}\Big)\, m_j + \sum_j \frac{\partial W(x_i - x_j, h_i)}{\partial h_i}\frac{\partial h_i}{\partial \tilde{\rho}_i}\,\delta\tilde{\rho}_i\, m_j,\end{aligned} \tag{4.4}$$

which turns out to be an explicit function:

$$\begin{aligned}\delta\tilde{\rho}_i &= \frac{1}{\omega_i}\sum_j \partial_\alpha W(x_i - x_j, h_i)\,\Big(\delta x_{\alpha,i} - \delta x_{\alpha,j}\Big)\, m_j, \\ \omega_i &:= 1 - \sum_j \frac{\partial W(x_i - x_j, h_i)}{\partial h_i}\frac{\partial h_i}{\partial \tilde{\rho}_i}\, m_j.\end{aligned} \tag{4.5}$$

Similarly, the volume-based regularization (3.48) delivers the coupled equations:

$$\tilde{\rho}_i = \tilde{\rho}_i \sum_j W(x_i - x_j, h_i)\, m_j, \quad h_i = \eta\Big(\frac{m_i}{\tilde{\rho}_i}\Big)^{1/d}, \tag{4.6}$$

which result in:

$$\delta\tilde{\rho}_i = \frac{\tilde{\rho}_i}{\omega_i}\sum_j \partial_\alpha W(x_i - x_j, h_i)\,\frac{m_j}{\tilde{\rho}_j}, \qquad \omega_i := 1 - \tilde{\rho}_i \sum_j \frac{\partial W(x_i - x_j, h_i)}{\partial h_i}\frac{\partial h_i}{\partial \tilde{\rho}_i}\,\frac{m_j}{\tilde{\rho}_j}, \tag{4.7}$$

the corresponding variation. Finally, the number smoothing (3.61) becomes:

$$\tilde{\rho}_i = m_i \sum_j W(x_i - x_j, h_i), \quad h_i = \eta \left(\frac{m_i}{\tilde{\rho}_i}\right)^{1/3} = \eta\, \tilde{n}_i^{-1/d}, \tag{4.8}$$

and varies as:

$$\delta\tilde{\rho}_i = \frac{m_i}{\omega_i} \sum_j \partial_\alpha W(x_i - x_j, h_i) \left(\delta x_{\alpha,i} - \delta x_{\alpha,j}\right),$$

$$\omega_i := 1 - m_i \sum_j \frac{\partial W(x_i - x_j, h_i)}{\partial h_i} \frac{\partial h_i}{\partial \tilde{\rho}_i}. \tag{4.9}$$

Like the equations derived in the previous section, the continuity equation is derived by considering $\delta(\cdot)$ to be a temporal variation $\mathrm{d}(\cdot)/\mathrm{d}t$. Equivalently, the variation of the medium's internal energy becomes:

$$\delta e_i = \frac{\mathrm{d}e_i}{\mathrm{d}\tilde{\rho}_i}\, \delta\tilde{\rho}_i = \frac{P_i}{\tilde{\rho}_i^2}\, \delta\tilde{\rho}_i. \tag{4.10}$$

In order to avoid lengthy mathematical writing, one should observe that ω_i may be treated similarly to the term $P_i/\tilde{\rho}_i^2$ in the equation above. Additionally, the $\partial_\alpha W(x_i - x_j, h_i)$ term is also a function of x_i through $h = h_i$ and should be treated likewise. Therefore, the continuity and motion equations for each type of regularization are the following, for the mass-smoothed medium:

$$\frac{\mathrm{d}\tilde{\rho}_i}{\mathrm{d}t} = \frac{1}{\omega_i} \sum_j \partial_\alpha W(x_i - x_j, h_i) \left(v_{\alpha,i} - v_{\alpha,j}\right) m_j, \tag{4.11}$$

$$\omega_i = 1 - \sum_j \frac{\partial W(x_i - x_j, h_i)}{\partial h_i} \frac{\partial h_i}{\partial \tilde{\rho}_i}\, m_j, \quad h_i = \eta \left(\frac{m_i}{\tilde{\rho}_i}\right)^{1/d}, \tag{4.12}$$

$$\frac{\mathrm{d}v_{\alpha,i}}{\mathrm{d}t} = -\sum_j \left(\frac{P_i}{\omega_i\, \tilde{\rho}_i^2}\, \partial_\alpha W(x_i - x_j, h_i) + \frac{P_j}{\omega_j\, \tilde{\rho}_j^2}\, \partial_\alpha W(x_i - x_j, h_j) \right) m_j. \tag{4.13}$$

For the volume-smoothed medium the equations become:

$$\left.\frac{\mathrm{d}\tilde{\rho}}{\mathrm{d}t}\right|_i = \frac{\tilde{\rho}}{\omega} \left| \sum_j \partial_\alpha W(x_i - x_j, h_i) \left(v_{\alpha,i} - v_{\alpha,j}\right) \frac{m}{\tilde{\rho}} \right|_j, \tag{4.14}$$

$$\omega_i = 1 - \tilde{\rho}_i \sum_j \frac{\partial W(x_i - x_j, h_i)}{\partial h_i} \frac{\partial h_i}{\partial \tilde{\rho}_i} \left.\frac{m}{\tilde{\rho}}\right|_i, \quad h_i = \eta \left(\frac{m_i}{\tilde{\rho}_i}\right)^{1/d}, \tag{4.15}$$

$$\left.\frac{\mathrm{d}v_\alpha}{\mathrm{d}t}\right|_i = -\frac{1}{\tilde{\rho}_i} \sum_j \left(\left.\frac{P}{\omega}\right|_i \partial_\alpha W(x_i - x_j, h_i) + \left.\frac{P}{\omega}\right|_j \partial_\alpha W(x_i - x_j, h_j) \right) \left.\frac{m}{\tilde{\rho}}\right|_j. \tag{4.16}$$

Finally, for the number-smoothed medium the equations of continuity and motion are:

$$\frac{\mathrm{d}\tilde{\rho}_i}{\mathrm{d}t} = \frac{m_i}{\omega_i} \sum_j \partial_\alpha W(x_i - x_j, h_i) \left(v_{\alpha,i} - v_{\alpha,j}\right), \tag{4.17}$$

$$\omega_i = 1 - m_i \sum_j \frac{\partial W(x_i - x_j, h_i)}{\partial h_i} \frac{\partial h_i}{\partial \tilde{\rho}_i}, \quad h_i = \eta\, \tilde{n}_i^{-1/d}, \tag{4.18}$$

$$\frac{\mathrm{d}v_{\alpha,i}}{\mathrm{d}t} = -\frac{1}{m_i} \sum_j \left(\frac{m_i^2\, P_i}{\omega_i\, \tilde{\rho}_i^2}\, \partial_\alpha W(x_i - x_j, h_i) + \frac{m_j^2\, P_j}{\omega_j\, \tilde{\rho}_j^2}\, \partial_\alpha W(x_i - x_j, h_j) \right). \tag{4.19}$$

Due to the thermodynamic relation (3.26), an internal energy evolution equation of the form:

$$\frac{\mathrm{d}e_i}{\mathrm{d}t} = \frac{P_i}{\tilde{\rho}_i^2} \frac{\mathrm{d}\tilde{\rho}_i}{\mathrm{d}t}, \tag{4.20}$$

corresponds to each set of the smoothed equations above.

4.2 Dissipative terms

In the context of SPH, dissipative terms are used for the modeling of dissipative media and additionally in order to accurately model the propagation of shocks through ideal media. In the latter case, this special treatment is necessary in order to dampen out spurious effects near shocks. Having derived SPH directly from the Lagrangian of the discrete system, Price [2008, 2012] notes that dissipative terms in the equation of motion of the ideal medium compensate for errors caused by the subtle assumption of a differentiable Lagrangian function; in the continuous setting this is Equation 3.18.

The dissipative terms of Monaghan [1997] are heuristically shown to have a structure similar to the structure of approximate Riemann solvers. They try to bridge the jumps of the conservative variables from "left" to "right" states of the Riemann problem, multiplied by eigenvalues that can be interpreted as signal velocities [Price, 2012].

Following Price [2008], a generic term of artificial dissipation for a scalar variable ψ is:

$$\left.\frac{\mathrm{d}\psi_i}{\mathrm{d}t}\right|_{\mathrm{diss}} = \sum_j m_j \frac{a_{\{\psi\}}\, v'_{\{\psi\}ij} (\psi_i - \psi_j)}{\overline{\rho}_{ij}} r_{\alpha,ij} \overline{\partial_\alpha W}_{ij}, \tag{4.21}$$

with the signal velocity:

$$v'_{\{\psi\}ij} \equiv \overline{c}_{ij} - \frac{1}{2} b_{\{\psi\}} v_{\alpha,ij} r_{\alpha,ij}, \tag{4.22}$$

defined via the relative particle velocity $v_{\alpha,ij} \equiv v_{\alpha,i} - v_{\alpha,j}$, and the unit vector:

$$r_{\alpha,ij} \equiv \begin{cases} \dfrac{x_{\alpha,i} - x_{\alpha,j}}{\|x_i - x_j\|}, & i \neq j, \\ 0, & i = j, \end{cases} \tag{4.23}$$

and the mean values $\overline{\rho}_{ij} = \frac{1}{2}(\tilde{\rho}_i + \tilde{\rho}_j)$, $\overline{c}_{ij} = \frac{1}{2}(c_i + c_j)$ and $\overline{\partial_\alpha W_{ij}} = \frac{1}{2}(\partial_\alpha W_{ij}(h_i) + \partial_\alpha W_{ij}(h_j))$, for the parameters $a_{\{\psi\}}$ and $b_{\{\psi\}}$. The notation $a_{\{\psi\}ij}$ highlights that each parameter refers to a conserved variable ψ and can have its own value. This formula for the signal velocity is typically augmented [Monaghan, 2005; Price, 2012] for SPH schemes, as an approximation of the signal-velocity term derived by Monaghan [1997]:

$$v'_{\{\psi\}ij} = \left(c_i^2 + b_{\{\psi\}}\,(v_{\alpha,ij}r_{\alpha,ij})^2\right)^{1/2} + \left(c_j^2 + b_{\{\psi\}}\,(v_{\alpha,ij}r_{\alpha,ij})^2\right)^{1/2} - v_{\alpha,ij}r_{\alpha,ij}. \tag{4.24}$$

In the following we preserve the original form rather than the approximate. Regarding the dissipative term, Price [2008] argues that it corresponds to the approximation:

$$\frac{\mathrm{d}\psi_i}{\mathrm{d}t}\Big|_{\text{diss}} \approx -2\sum_j \left(\psi_i - \psi_j\right)\overline{\partial_\alpha W}_{ij} r_{\alpha,ij}\frac{m_j}{\rho_j} \approx \lambda\frac{\partial^2\psi_i}{\partial x_{\alpha\alpha}}, \tag{4.25}$$

with $\lambda \propto a_{\{\psi\}}v'_{\{\psi\}}\|x_{ij}\|$. Additionally, Price [2012] suggests that dissipation should be added to every conservation equation and thus to the evolution of the variables $\psi = \{\tilde{\rho}, v_\alpha, e^*\}$, where $e^* = \frac{1}{2}v_\alpha^2 + e$. When the integral form of mass conservation is used, there is no need for artificial dissipation in mass evolution, since there is no differential involved.

Finally, modern astrophysical SPH solvers are equipped with dissipation switches [Monaghan, 2005; Price, 2008], which turn on and off artificial dissipation when necessary, by evolving in time the parameters $\alpha_{\{\psi\}}$. We found their use non-critical for the successful completion of the tests presented in this thesis. Therefore, to keep things simple and generic, the preset study chooses not to discuss them.

Dissipative mass-flux In order to accurately describe propagating jumps in density we construct an artificial diffusive mass-flux term, inspired by the structure of Equation 4.21. However, since density discontinuities are natural characteristics of inhomogeneous materials, smoothing these is ruled out. An expression in the same manner as Equation 4.21 needs to account for pressure differences. From dimensional analysis point of view, changing density differences into pressure differences in the general form of diffusive terms (4.21) needs to be complemented with a division by a characteristic velocity $v_{\{\rho\}ij}$. Thus, we suggest the following structure:

$$\frac{\mathrm{d}\tilde{\rho}_i}{\mathrm{d}t}\Big|_{\text{diss}} = \sum_j m_j \frac{a_{\{\rho\}}(P_i - P_j)}{\overline{\rho}_{ij}v_{\{\rho\}ij}} r_{\alpha,ij}\overline{\partial_\alpha W}_{ij}, \quad v'_{\alpha,ij}r_{\alpha,ij} \leq 0, \tag{4.26}$$

The optimal values for the parameters are discussed along with the numerical experiments in the next chapter. Note that for $v_{\alpha,ij}r_{\alpha,ij} \leq 0$, $v_{\{\rho\}ij} > 0$, since $\overline{c}_{ij} > 0$.

Viscosity Similarly to Price [2012], diffusion in the momentum equation is added in the form of (4.21):

$$\frac{\mathrm{d}v_{\alpha,i}}{\mathrm{d}t}\Big|_{\text{diss}} = \sum_j m_j \frac{a_{\{v\}}v'_v(v_{\alpha,i} - v_{\alpha,j})r_{\alpha,ij}}{\overline{\rho}_{ij}}\,\overline{\partial_\alpha W}_{ij}, \quad v_{\alpha,ij}r_{\alpha,ij} \leq 0, \tag{4.27}$$

and zero otherwise.

Thermal conductivity For problems involving thermal effects, artificial thermal conductivity is added to the evolution of specific internal energy [Monaghan, 2005; Price, 2012], as:

$$\frac{\mathrm{d}e_i}{\mathrm{d}t}\Big|_{\mathrm{diss}} = -\sum_j \frac{m_j}{\overline{\rho}_{ij}}\Big(\frac{1}{2}a_{\{v\}}v'_{\{v\}ij}(v_{\alpha,ij}r_{\alpha,ij})^2 + \alpha_{\{e\}}v'_{\{e\}ij}(e_i - e_j)\Big)r_{\alpha,ij}\overline{\partial_\alpha W}_{ij}, \quad v_{\alpha,ij}r_{\alpha,ij} \leq 0, \tag{4.28}$$

and zero otherwise. The above form refers to the physically appropriate conservation of the total energy e^*, rather than the internal energy e. Note that Price [2008] introduces the signal velocity term: $v'_{\{e\}ij} = \sqrt{|P_i - P_j|/\overline{\rho_{ij}}}$, so that artificial conductivity is applied only in order to eliminate spurious pressure gradients across contact discontinuities

In the literature of SPH, a similar approach of adding diffusive terms in all evolution equations appears [Libersky et al., 1997; Randles and Libersky, 1996], termed *conservative smoothing*. The most noteworthy differences are the following: 1) the present dissipative terms belong to a generic form and are designed such that they complement schemes coming from a variational SPH framework [Monaghan, 2005; Price, 2008, 2012], 2) they come from a framework which incorporates the W–h–ρ coupling, 3) the dissipative terms are directly related to approximate Riemann solutions Monaghan [1997] and finally 4) the new dissipative mass flux term is precisely designed to treat spurious spikes on the internal interface of inhomogeneous materials.

4.3 Time integration

Properties of the Lagrangian formulation are better preserved using *symplectic integrators* and Monaghan [2005] states that they should be used for SPH. Accordingly, in all following tests, time integration is achieved with a *leap-frog scheme*, which initiates as:

$$\{\mathrm{d}\tilde{\rho}/\mathrm{d}t, \mathrm{d}v_\alpha/\mathrm{d}t, \mathrm{d}e/\mathrm{d}t\}_i^0 = f(x_{\alpha,i}^0, v_{\alpha,i}^0, \rho_i^0, e_i^0) \tag{4.29}$$

$$\{\tilde{\rho}, v_\alpha, e\}_i^{1/2} = \{\tilde{\rho}, v_\alpha, e\}_i^0 + \{\mathrm{d}\tilde{\rho}/\mathrm{d}t, \mathrm{d}v_\alpha/\mathrm{d}t, \mathrm{d}e/\mathrm{d}t\}_i^0 \Delta t|^1/2, \tag{4.30}$$

and continues from any subsequent timestep $k > 0$ to timestep $k+1$ as:

$$\{\mathrm{d}\tilde{\rho}/\mathrm{d}t, \mathrm{d}v_\alpha/\mathrm{d}t, \mathrm{d}e/\mathrm{d}t\}_i^k = f(x_{\alpha,i}^k, v_{\alpha,i}^k, \rho_i^k, e_i^k) \tag{4.31}$$

$$\{\tilde{\rho}, v_\alpha, e\}_i^{k+1/2} = \{\tilde{\rho}, v_\alpha, e\}_i^{k-1/2} + \{\mathrm{d}\tilde{\rho}/\mathrm{d}t, \mathrm{d}v_\alpha/\mathrm{d}t, \mathrm{d}e/\mathrm{d}t\}_i^k \Delta t|^k \tag{4.32}$$

$$x_{\alpha,i}^{k+1} = x_{\alpha,i}^k + v_{\alpha,i}^{k+1/2}\Delta t|^k \tag{4.33}$$

$$\{\tilde{\rho}, v_\alpha, e\}_i^{k+1} = \{\tilde{\rho}, v_\alpha, e\}_i^{k+1/2} + \{\mathrm{d}\tilde{\rho}/\mathrm{d}t, \mathrm{d}v_\alpha/\mathrm{d}t, \mathrm{d}e/\mathrm{d}t\}_i^k \Delta t|^k/2. \tag{4.34}$$

The timestep criterion is according to the Courant-Friedrichs-Lewy criterion $\Delta t^k = \xi_{CFL} \min\{v_i + c_i)/h_i\}$, with $\xi_{CFL} \in [0.1, 0.3]$ and specified in tests. A maximum timestep due to artificial dissipation was not necessary.

4.4 Initial particle configuration

In general, for SPH computations two different initial configurations of particles are possible: particles of equal masses placed in a non-uniform manner or particles of uniform spacing and unequal masses, as discussed in Section 3.1.1. These two options are depicted in Figure 4.1, where the same medium, comprising of regions of constant density (red and green regions), is discretized with particles in a uniform spacing (*left*) and particles in a non-uniform spacing (*right*). No matter which one is used, it should be able to reproduce the initial density ρ_0, and for that, unequal particle masses are necessary in the first case, while the latter case can be also constructed with particles of equal masses. Mathematically, they correspond to two different building procedures. First, the *empirical measure*:

$$\mu_0 = \overline{m} \sum_i \delta_{x_{0,i}}, \quad \overline{m} \equiv \frac{\int_{\Omega_0} \mathrm{d}\mu_0}{N}, \tag{4.35}$$

is constructed in a probabilistic manner [Evers et al., 2015]. Effectively, the density ρ_0 of the medium is the corresponding probability density function. Second, the measure:

$$\mu_0 = \sum_i m(x_{0,i})\, \delta_{x_{0,i}}, \quad m(x_{0,i}) := \int_{\Omega_{0,i}} \mathrm{d}\mu_0 = \rho_0(x_i) \int_{\Omega_{0,i}} \mathrm{d}\lambda, \tag{4.36}$$

is constructed in a deterministic way, using a discretization of the domain Ω_0.

Consequently, the three derived schemes may be combined with two initial configurations of the particle system. Notice that for particle systems of equal masses, the mass-based smoothing (3.38) and the number-based smoothing (3.61) are equivalent. The same holds, in case the adaptive schemes of Section 4.1 are used, where additionally, they are endowed with the same form of adaptivity $h = h(\tilde{n})$. Alternatively, if particles of unequal masses are to be used, the only scheme which respects this type of adaptivity, is the number-smoothed.

Usually, particles of equal masses are used for shock problems [Borve and Price, 2009; Monaghan and Gingold, 1983; Price, 2008], although there appears no clear motivation for this choice in the literature. Indeed, this subtlety is discussed in the tests of Chapter 5 and its effects appear.

Regarding the practical aspects of each construction, let us examine the discretization of a simple one-dimensional domain, with regions L and H, of densities $\rho_{0,H} > \rho_{0,L}$. For the empirical measure, a uniform discretization per specie is chosen, such that each line increment in the low density region is $D_L \equiv \int_{\Omega_{0,i\in A}} \mathrm{d}\lambda$. Consequently, particles of

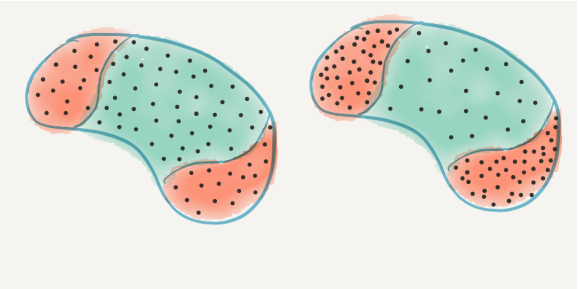

FIGURE 4.1: Two different ways to construct the density profile of an inhomogeneous medium: particles in uniform spacing (*left*) and particles in a non-uniform spacing (*right*).

this region are separated by interparticle distances D_L and obtain a mass $m_L = D_L \rho_{0,L}$. Particles of the same masses are placed at $D_H = D_L(\rho_{0,L}/\rho_{0,H})$ interparticle distances in the higher density region H. As a result, the largest discretization length is dictated by the region with the lowest density $\rho_{0,L}$ in the system. Alternatively, in order to achieve uniform partitioning overall the domain, a discretization length D is selected and one particle is placed in the middle of each domain partition. The mass of each particle is assigned according to the initial density distribution, as: $m(x_{0,i}) = \rho_0(x_{0,i})D$.

For spatial dimensions $d = \{2, 3\}$, the procedures above lead to rectangular packings of the particles, while other denser configurations such as hexagonal packings may be advantageous. Diehl et al. [2015] discuss various options. In any case, the discretization lengths D_L and D_H, which are necessary to initiate the filling of the particles in the domain, are obtained with the above procedure. As discussed in Chapter 2, a centroidal Voronoi tessellation can be used in order to furnish a uniform partitioning.

4.5 Numerical evidence of convergence

The *Wasserstein distance* of two measures μ_1 and μ_2 in the space of probability measures is defined as:

$$\mathcal{W}(\mu_1, \mu_2) = \inf_{\Pi \in \Pi(\mu_1, \mu_2)} \int_{R^d \times R^d} |\chi - \psi| \, \Pi(d\chi, d\psi) \tag{4.37}$$

and it is a way to assign a cost-function to any admissible configuration of the system. We denote by $\Pi(\mu_1, \mu_2)$ the set of all *joint representations* of μ_1 and μ_2. Joint representations are also called *couplings* and are defined such that for each $i = 1, 2$:

$$\int_{R^d \times R^d} f(\chi_i) \, \Pi(d\chi_1, d\chi_2) = \int_{R^d} f(\chi) \, \mu_i(d\chi), \tag{4.38}$$

for all measurable, bounded functions f on $\mathbb{R}^d$. For an exposition on the Wasserstein distance and the related concept of optimal transport, we refer to Evers et al. [2015] and the related references therein.

Considering the mass-smoothed system of (3.38), written with respect to the continuous measure μ, and the corresponding system written for the discrete measure μ^N, the proof in Evers et al. [2015] establishes that:

$$\sup_{t\in[0,T]} \mathcal{W}(\mu_t^N, \mu_t) \to 0, \text{ as } N \to \infty. \tag{4.39}$$

Note that in the expression above we explicitly write the dependence of μ on t. The proof is an extension of an older result of DiLisio et al. [1998]. The discussion about the differences between the two approaches and a comprehensive comparison of the equations treated in each case can be found in Evers et al. [2015].

The paradigms of the numerical illustration, which follow, are performed for a series of increasing particle numbers N_k. For each computation, after normalizing the total mass of the system, at each time instance $t \in I := \{\phi T/10, \phi = \{0, ..., 10\} \subset \mathbb{N}\}$, we solve a linear programming problem to calculate:

$$M_{k,k+1} := \max_{t\in I} \mathcal{W}(\mu_t^{N_k}, \mu_t^{N_{k+1}}) \approx \sup_{t\in[0,T]} \mathcal{W}(\mu_t^{N_k}, \mu_t^{N_{k+1}}), \tag{4.40}$$

and furnish the convergence rate:

$$C_{k+1}^{(d)} := \log_{\frac{N_{k+1}}{N_k}} \Big(\frac{M_{k+1,k+2}}{M_{k,k+1}}\Big). \tag{4.41}$$

The theoretically predicted $C_{k+1}^{(d)}$ is the same as for the initial measure, i.e. $O(N^{-1/d})$, whence we expect that it tends to the value $-1/d$.

A critical point of the theoretical result of Evers et al. [2015] (and previously of DiLisio et al. [1998]) is that it makes no conclusion on the smoothing length h. The convergence proof is achieved for h fixed with the number of particles, and the dependence of h on N is not investigated. It is known that in order for the regularized equations of hydrodynamics to approximate the real physics well, h should be sufficiently small. As discussed in Chapter 2, in the SPH literature this is achieved by taking $h = \eta\, N^{-1/d}$, with $1.2 \leq \eta \leq 1.5$, for Gaussian-like kernels. By extension, cases of spatially and temporally varying h, like those used in shock problems Monaghan [2005], are not covered by the theoretical result.

The theoretical proof of convergence Evers et al. [2015] covers cases broader than the equations of the ideal medium discussed in the previous section. First and foremost, the form of the potential energy covered by the theoretical proof of convergence is:

$$e^* = e^*(\rho(x), x) = e(\rho(x)) + u(x), \tag{4.42}$$

with e the internal energy of the medium given by $\partial e/\partial\rho = P(\rho)/\rho^2$, and u an external field, such as gravity. A limitation of the theoretical proof is that the admissible equations of state are of the form:

$$P(\rho) = c\,\rho^\gamma, \tag{4.43}$$

where c is a parameter and γ, the so-called *polytropic exponent*, which needs to satisfy $\gamma > 1$. It should be underlined that the theoretical proof is not conclusive about equations of state in the form $P(\rho) = B \cdot ((\rho/\rho_0)^\gamma - 1)$, which are typically employed in SPH computations for the modeling of liquids or solids Monaghan [2005].

Apart from the ideal system of the mass-smoothed medium —discussed in Section 3.3.1, the proof of convergence covers processes described by the problem:

$$\delta\mathcal{S}|_0^T = -\int_0^T \int_\Omega \Big(-\mu_{\text{vsc}}(x)\, v_\alpha(x) + \int_\Omega K(x-y)\, \mathrm{d}\mu(y) \Big)\, \delta x_\alpha\, \mathrm{d}\mu(x)\, \mathrm{d}t, \tag{4.44}$$

so that in the resulting acceleration of the ideal medium, the terms $-\partial_\alpha u(x) - \mu_{\text{vsc}}(x)\, v_\alpha(x) + \int_\Omega K(x-y)\, \mathrm{d}\mu(y)$ need to be added. In the general case K can be an anisotropic kernel, $K(x-y) \neq K(\|x-y\|)$, describing non-local interactions within the system. The term $\mu_{\text{vsc}} = \mu_{\text{vsc}}(x)$ is a model for dissipation without non-local characteristics. It should be stressed that this is in contrast to the non-locality of the dissipative term:

$$\sim \int_\Omega \Big(v_\alpha(x) - v_\alpha(y) \Big) \partial_{\beta\beta} W(x-y)\, \frac{d\mu}{\tilde{\rho}}\Big|_{(y)}, \tag{4.45}$$

typically constructed (via approximation of $\partial_{\beta\beta} W$) in SPH, to model viscosity (e.g. Monaghan [2005]). Note that this construction further assumes the approximation: $\mathrm{d}\lambda = \mathrm{d}\mu/\rho \approx \mathrm{d}\mu/\tilde{\rho}$, which characterizes the volume-smoothed medium of Section 3.3.2.

We construct the initial measure μ_0^N, corresponding to the N-particle approximation of μ_0, according to a partitioning of the initial domain in N subdomains of incremental volume V_i. Masses are assigned as $m_i = \rho_0(x_i)\, V_i$ for each $i = 1, \ldots, N$. In Section 3.1.1 (and in Evers et al. [2015] formally) two ways of constructing the sequence μ_0^N are shown, such that it converges to μ_0 at rate $\mathcal{O}(N^{-1/d})$; they correspond to particle initialization strategies typically used in the SPH literature. The theoretical convergence result Evers et al. [2015] establishes that the corresponding solutions μ^N converge at the same rate.

In Evers *et al.* Evers et al. [2015], test cases which conform to the assumptions of the proof are examined. The cases that follow here and which are also presented in Zisis et al. [2016a], suggest that the same theoretical results may be expected to hold also for cases that are typically used for benchmarking SPH algorithms, but do not satisfy all the assumptions of the convergence theorem in Evers et al. [2015].

4.5.1 Evolution of elliptical drop

The evolution of an elliptical drop is a benchmark problem for weakly compressible flows, which admits an analytical solution [Monaghan, 1994]. It refers to an initially circular water drop (of unit radius) which attains an elliptical shape under the shearing velocity field $(v_{0,x_1}, v_{0,x_2}) = (-100x_{0,1}, 100x_{0,2})$. The problem involves a conservative part, with $P(\rho) = B \cdot ((\rho/\rho_0)^7 - 1)$, and a dissipative part. The numerical recipe

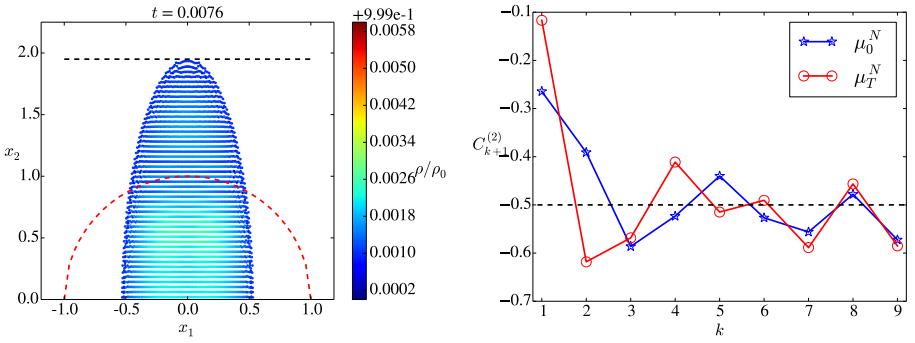

FIGURE 4.2: Droplet test; final-to-initial density at t=0.0076 and convergence rates of the initial (*blue*) and the final (*red*) measures.

is considered standard in the current SPH literature. For the motion due to the hydrodynamic conservative part we use the equation of motion of the mass-smoothed medium of Section 3.3.1 and dissipation is modeled with the analogous term of Monaghan and Rafiee [2013], which pertains to Equation 4.45. Additionally, the Wendland C2 kernel [Monaghan and Rafiee, 2013], and a leapfrog time integrator —preferred for its symplectic nature— are used, with $h = 1.5N^{-1/2}$ assigned to all particles. Furthermore, we employ the artificial mass-flux term of Zisis et al. [2015b] with the corresponding parameters $\alpha = 0.5$ and $\beta = 0$, to counteract oscillations in the density profile. We examined two different systems: 1) the mass-smoothed medium of Section 3.3.1; 2) the volume-smoothed medium of Section 3.3.2, which is also employed by Monaghan and Rafiee [2013]. Results are practically indistinguishable. Additionally, note that in this problem of a single homogeneous medium, the former approach is equivalent to the number-smoothed medium. The left plot of Figure 4.2 shows the upper half plane of the problem for $N = 7232$ at normalized time $t = 0.0076$, when Monaghan [1994] records the height of the semi-major axis. He finds the latter height to be 1.91, compared to 1.95 for the analytical result (black dashed horizontal line in Figure 4.2) and our 1.93. We follow the process until normalized final time $t = 0.01$, achieved with a time step $\Delta t = 10^{-6}$. The right plot of Figure 4.2 shows the convergence rates $C^{(2)}_{k+1}$ of the initial measure μ^N_0 and the final one μ^N_T, with respect to the Wasserstein distance between particle systems of successive particle numbers $N_k \in \{2, 12, 32, 52, 112, 208, 448, 812, 1804, 3228, 7232\}$. The convergence rates oscillate around the theoretically predicted value $-1/2$, and they tend to become identical. Computing the Wasserstein distance for higher N_k becomes computationally too expensive for our brute-force algorithm. In order to fill the initial circle (red dashed circle in Figure 4.2) with N_k particles, we use $\ell_k = \{2, 4, 6, 8, 12, 16, 24, 32, 48, 64, 96\}$ particles per unit length to pack particles within a larger square and then disregard all particles falling outside. Recall that the theoretical result (Sections 3 and 4) does not support the current form of dissipation, the equation of state, or the specific functional dependence of h on N, in the proof h is assumed to be a fixed parameter for all examined N_k. Moreover, we obtained indistinguishable results using the SPH-approximation of the continuity equation [Monaghan and Rafiee, 2013], for which

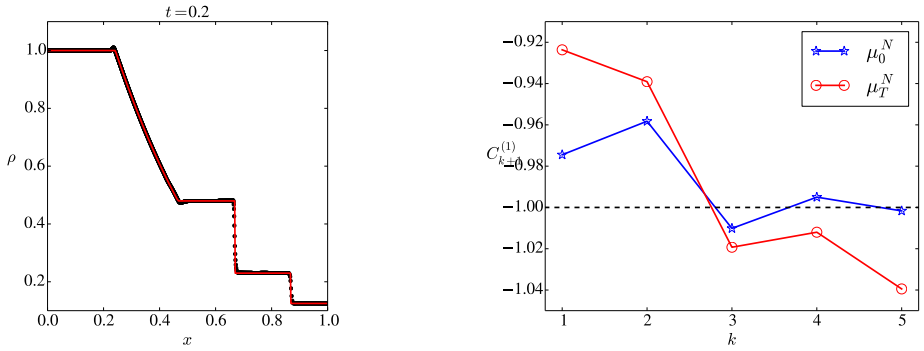

FIGURE 4.3: Shock-tube test; density at t=0.2 and convergence rates of the initial (*blue*) and the final (*red*) measures.

the theoretical result is not applicable. Yet, our numerical results provide evidence that typically used weakly compressible SPH schemes converge with respect to the Wasserstein distance. Rigorous proofs are left for future work. Our conjecture that the scaling $h \sim N^{-1/d}$ is the correct one, may serve as a guideline.

4.5.2 Shock tube

The *shock tube test* is a classic one-dimensional test, frequently employed for the validation of fully compressible SPH schemes [Monaghan, 2005; Price, 2012; Zisis et al., 2015b]. It is also discussed in more detail in Section 5.2. In this test, there is a discontinuity in the density profile of the medium, with $\rho_0(x_0 < 0.5) = 1$ and $\rho_0(x_0 \geq 0.5) = 0.125$. We construct the initial density profile with particles of equal masses and solve the system of Equations 4.11, for the mass-smoothed medium with a varying smoothing length $h_i := 1.2\, n_i^{-1}$. The complete solution strategy is further discussed in Section 5.2 (also found in Zisis et al. [2015b]) and falls within the standard SPH framework [Monaghan, 2005; Price, 2012]. The typical resolution is 450 particles in total [Price, 2012; Zisis et al., 2015b] and therefore, we examine convergence with respect to the Wasserstein distance for $N_k \in \{18, 45, 90, 225, 450, 900, 1800\}$, to the theoretical value $C^{(1)}_{k+1} = -1$. The distinct characteristic of this case is that h varies spatially and temporally. This is not supported by the theoretical result of convergence [Evers et al., 2015], neither are the —necessary for the solution— artificial dissipative terms in all equations, as described in Section 4.2. Nonetheless, in Figure 4.3 the system is shown to converge in a manner similar to the prediction of the theoretical result. The density profile for the highest resolution is also presented in Figure 4.3, against the analytical solution (red solid line) at final normalized time $t = 0.2$.

4.5.3 Discussion

A limitation of the theoretical proof is that it is not conclusive regarding the number of particles going to infinity and the smoothing length going to zero at the same time. It rather holds for examining a fixed value of smoothing length as the number of particles goes to infinity. Additionally, open problems are the inclusion of the following features: dissipation with a non-local character, similar to the one typically used in SPH to mimic viscosity of fluids; equation of states for liquids and solids; spatially varying smoothing length.

The presented convergence study introduces an innovation, by supporting the theoretical proof with numerical evidence. More specifically, we calculate the convergence rates of the SPH system corresponding to two problems typically employed in the SPH literature, however with formulations not covered by the theoretical result. One refers to the schemes used in weakly compressible SPH computations and another to fully compressible SPH schemes, where h is varying in space and time. For both test cases we observe the theoretically predicted convergence rate with respect to the Wasserstein distance as the number of particles increases.

CHAPTER 5

Hydrodynamical validation tests

The following tests concern the propagation of shocks through media. Consequently, the chosen scheme is required to resolve the spatially varying length scale in the problem domain. To this end, adaptivity of the smoothing length is necessary and the methods described in Section 4.1 provide the framework for this task. As the following numerical experiments show, coupling the smoothing length with the local number density seems to be the sole correct option. This is conjectured by Price [2012].

In general, two different initial configurations of the SPH particles can be applied: particles of equal masses or particles of uniform spacing (see Section 4.4). Consequently, the three derived schemes may be combined with two initial configurations of the particle system. For particle systems of equal masses the mass-smoothing approach (4.11) and the number-smoothing approach (4.17) are equivalent and hence adaptivity is indeed in the form $h = h(\tilde{n})$. Alternatively, if particles of unequal masses are to be used, the only scheme which respects this type of adaptivity, is the number-based smoothing.

In the related literature, fully compressible problems are typically solved with particles of unequal masses [Borve and Price, 2009; Monaghan and Gingold, 1983; Price, 2012]. Due to the geometric restrictions of this method, as discussed in Section 4.4, the following tests aim at answering how well fully compressible SPH computations can perform, using particles of unequal masses and, chiefly, the number-based smoothing.

We focus only on the differential forms of Section 4.1, for three reasons. First, according

to Section 3.4, they guarantee zeroth order discrete approximation by construction and thus they are appropriate for bounded domains, like those of the problems in Chapter 6. Second, they do not require the solution of a system of equations (like Equation 4.3 or 4.8), when adaptive schemes are used and the smoothing length becomes a local variable. Third, the integral forms of mass conservation abruptly smooth out contact discontinuites, even though such an effect is not predicted by all equations of state (e.g. the barotropic Equation 5.1) or problem setups. On the other hand, the differential forms of mass conservation require a velocity difference to trigger the variation of density and this is an attractive feature for the problems in Chapter 6, as well as for many problems in the present Chapter.

5.1 Isothermal shock-bar tests

The first test is the Riemann problem which is solved analytically in Section 1.1.4 and refers to the isothermal impact of a homogeneous projectile onto an inhomogeneous target. The main assumption is that due to the high kinetic energy involved, materials respond hydrodynamically and only normal stresses develop, following the barotropic equation of state:

$$P(\rho) = c_0^2 \, (\rho - \rho_0), \tag{5.1}$$

also introduced in Section 1.1.3. The isothermal conditions imply constant speeds of sound. More importantly, this test is the closest model to the impacts which are discussed in Chapter 6 and admits closed form solution as well. Starting from left to right, the domain comprises the *projectile* and the three different regions of the *target*, which model three distinct materials, according to:

$$\{\rho, v, \rho_0, c_0\} = \begin{cases} \{1, 1, 1, 1\}, & 0 \leq x < 0.6; \\ \{1, 0, 1, 1\}, & 0.6 \leq x < 0.8; \\ \{0.25, 0, 0.25, 0.5\}, & 0.8 \leq x < 1.2; \\ \{1, 0, 1, 1\}, & 1.2 \leq x \leq 1.4. \end{cases}$$

The initial conditions (for $x > 0.4$) are presented in Figure 5.1. There exist two contact discontinuities which are not affected until a wave reaches them.

The parameters ρ_0 and c_0 of each state are the reference density and the constant speed of sound respectively. The problem is solved with a constant time-step of $\Delta t = 5 \times 10^{-5}$ towards observation time $t = 0.4$. This time is enough for the right-moving shock wave which emanates from the initial discontinuity in velocity to reach the interface of the two-phased target. It splits into a reflected rarefaction wave and a transmitted shock wave (Section 1.1.4). We focus on ρ and P, since they are the most sensitive variables to instabilities, rather than velocity. In both cases, we use the dissipation parameters $a_\rho = 0.2$, $b_\rho = 2.0$ and the standard artificial viscosity parameters $a_v = 1.0$, $b_v = 2.0$.

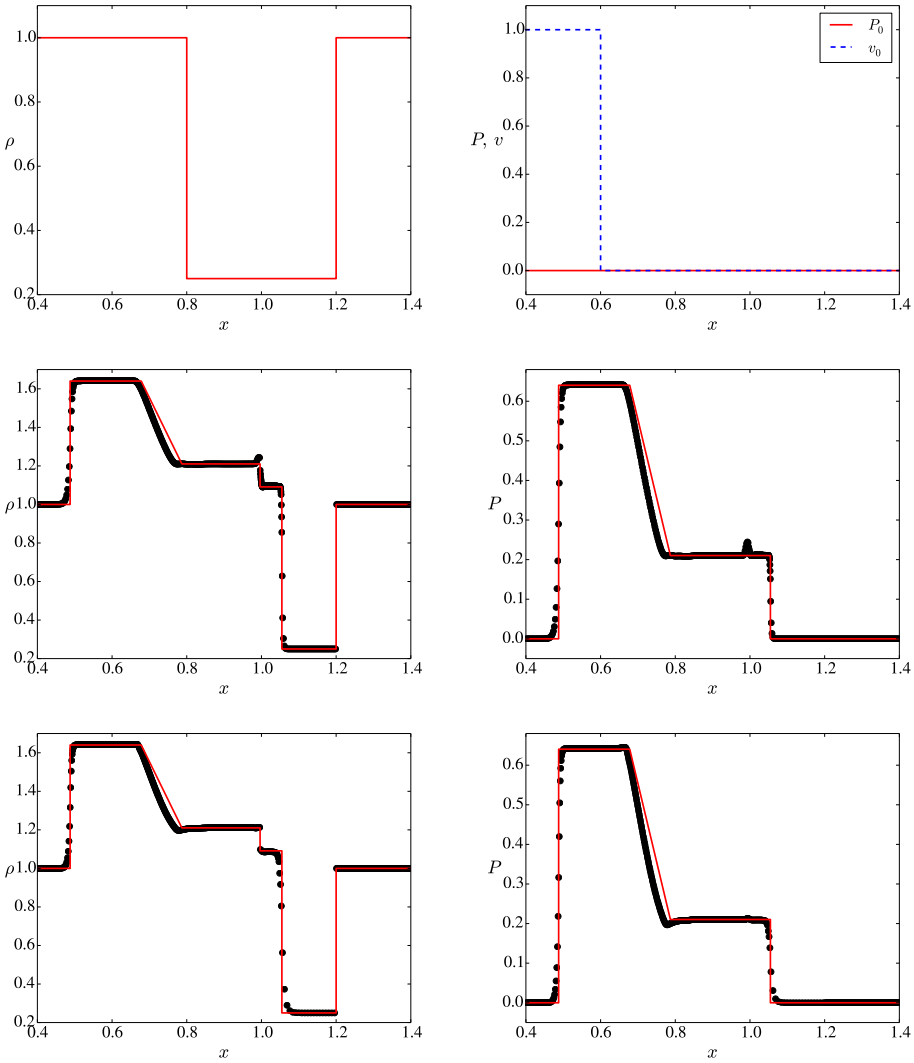

FIGURE 5.1: The isothermal shock-bar test at $t = 0$ (*upper plots*), and at $t = 0.4$ for the number density scheme, with particles of unequal masses (*middle plots*) and equal masses (*lower plots*).

In the upper plots of Figure 5.1, particles of unequal masses are employed to solve the problem with the number-density scheme. The SPH solution for $N_\ell = 400$ particles per unit of length is shown with black dots and the analytical solution with the red continuous line. The left running rarefaction is approximated with a line. In the lower plots of Figure 5.1, a distance $D_L = 0.005$ in the low-density region creates particles of equal masses. The results show that the solution using the latter strategy offers a nearly flat pressure profile around the contact discontinuity, as expected by the exact solution. A small hump appears at the same place for the system of unequal masses. Besides this, both numerical solutions accurately follow the wave pattern of

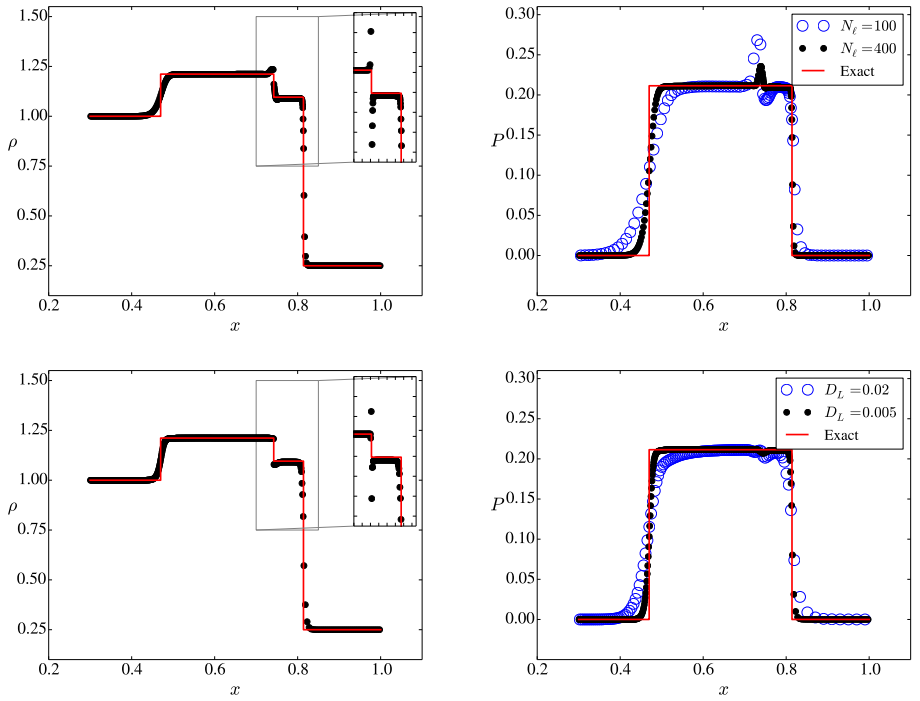

FIGURE 5.2: The asymmetric impact test for initial density ratio 1/4 and speed-of-sound ratio 1/2, at $t = 0.3$, for the number-density scheme with particles of unequal masses (*upper plots*) and equal masses (*lower plots*). For comparison, results without dissipative mass flux appear in the inset plots.

the analytical solution.

For a closer examination of the various schemes, the *asymmetric impact* test of Davison [2008], Ch.3, seems more appropriate. In $x \in [0, 0.5)$, the state of the moving material is $\{\rho_{left}, v_{left}\} = \{\rho_{0,left}, c_{0,left}\} = \{1, 1\}$, while on the right side $x \in [0.5, 1.0]$ the material is described by $\{\rho_{right}, v_{right}\} = \{\rho_{0,right}, 0\}$. In each test-case studied below $\rho_{0,right}$ and $c_{0,right}$ take different values, while the barotropic equation of state (5.1) is employed.

In Figure 5.2, the convergence of the test-case with $\rho_{0,right} = 0.25$ and $c_{0,right} = 0.5$ appears, employing a crude discretization (blue dots) and a four times finer one (black dots). The upper plots refer to particles of unequal masses for $N_\ell = \{100, 400\}$ particles per unit length and the lower ones, to particles of equal masses with initial distances $D_L = \{0.02, 0.005\}$ in the low density region. Respectively, the time steps $\Delta t = \{10^{-4}, 5 \cdot 10^{-5}\}$ are used until time $t = 0.3$. In the inset plots, the density around the contact discontinuity is presented for the finer discretization, when no artificial mass flux is used.

By and large, the two systems converge to the exact solution as the number of particles

increases. The main difference is located at the contact discontinuity, where the system of unequal masses is unable, for the given number of particles, to provide a sharp discontinuity in density and thus, diminish the hump in the pressure profile. This effect is attributed to the way the number-smoothed density is constructed. To see this, consider Equation 3.61, and write:

$$m(x_i)\,\tilde{n}(x_i) = m(x_i)\sum_j W(x_i - x_j) = \sum_j W(x_i - x_j)\frac{m(x_i)}{m(x_j)}\int_{\Omega_j} \mathrm{d}\mu. \tag{5.2}$$

For a regular configuration of particles, $N \to \infty$ implies $n \to \infty$ and by virtue of $h \propto n^{-1/d}$, $h \to 0$. The latter means that in this limiting case the contribution of the terms $m(x_i)/m(x_j)$ from particles j around i decreases fast, and the term $m(x_i)/m(x_{j=i}) \equiv 1$ dominates and we arrive to $\rho(x_i)$. Note that the observation holds as far as the $m(x_i)$ and $m(x_j)$ involved in the summation are not of extremely different scales. Regarding problems of finite number of particles —as the numerical paradigm— terms $m(x_i)/m(x_j)$, which are not unity, remain in the previous sum. Thus, they make the result around the contact discontinuity worse than the one obtained from the mass-smoothed medium: $\sum_j W(x_i - x_j)\int_{\Omega_j} \mathrm{d}\mu$.

Note that this effect is to not be confused with the singularity appearing in the inset plots of density (Figure 5.2) for both particle systems. This is the result of neglecting the boundary terms in the variation of the integral operator Price [2008]; Zisis et al. [2015b] and it occurs for any of the smoothed density estimates. Therefore, the use of the artificial mass-flux is crucial in removing the singularity in both cases.

Another difference is that the system of unequal-masses smears out the left running wave in a larger region than the equal-mass system. Effectively, the left-running and the right-running waves appear to be the same for the equal-mass system. Last but not least, we report that in case a large time-step is used, the value of density in the region between the right-moving shock and the contact discontinuity is underestimated. This is precisely the region of the highest changes of density in the system. We may infer that the time-step is bounded by the maximum time-variation of density and thus the time-step should be governed by a corresponding criterion, besides the CFL criterion. In Figure 5.3, there appears some evidence that in problems of varying h not all the developed schemes are wise choices. The left subplot shows the region around the contact discontinuity for schemes employing particles of unequal masses, while the right subplot depicts the solutions of schemes with equal-mass particles. The profile of density on the right of the contact discontinuity is overestimated for the volume-smoothed approach (Equation 4.14) in both particle configurations and the mass-smoothed approach for the unequal-mass system (Equation 4.11). This is a spatial error and it persists after reduction of the time-step. In conclusion, for systems with particles of unequal masses and varying h, the number-density scheme appears to be the only choice.

The following tests explore the generality of the number-density scheme and its limitations for isothermal problems. In Figure 5.4 the plots of pressure refer to the problem of initial data $\rho_{0,right} = 0.5$, $c_{0,right} = 0.5$, at $t = 0.3$. The number-density scheme is used with $N = 400$ particles placed at uniform initial spacing (right plot)

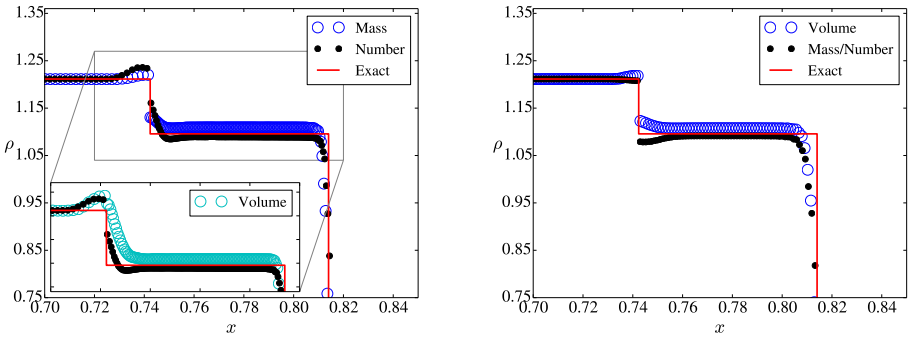

FIGURE 5.3: The asymmetric impact test for initial density ratio 1/4 and speed-of-sound ratio 1/2, at $t = 0.3$, in the region of the shock and the contact discontinuity. Particles of unequal masses (*left*) and particles of equal masses (*right*). Recall that number-smoothing and mass-smoothing deliver identical schemes.

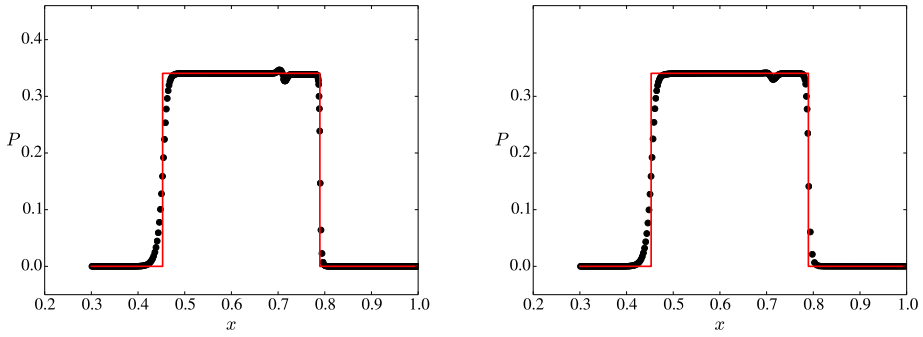

FIGURE 5.4: The asymmetric impact test at $t = 0.3$, for density and soundspeed ratios 1/2. The number-density scheme with (*left*) particles of equal masses and (*right*): unequal masses.

and a system of $N = 500$ equally-massed particles (left plot). Recall that the different number of particles is due to the restrictions of the particle-filling procedure for equal masses. A more demanding case occurs for the data $\rho_{0,right} = 0.25$, $c_{0,right} = 0.25$, primarily due to the high speed-of-sound ratio. It is for this purpose that an increased value of $a_\rho = 1.0$ is necessary to suppress the singularity in the pressure profile at the contact discontinuity. Additionally, a finer resolution is required, leading to a higher amount of particles. The corresponding pressure profiles of Figure 5.5 are for $N = 800$ particles of uniform initial spacing (left plots) and $N = 1250$ particles of equal masses (right plots). The inset plots show the solution for $a_\rho = 0.2$ around the contact discontinuity, which can be considered as a standard value for density ratios up to 1/4 and speed-of-sound ratios up to 1/2. Apparently, the latter ratio plays a critical role.

Thus, a preliminary conclusion and a suggestion follows the asymmetric impact test. Whenever density ratios are small, say $\rho_{0,left}/\rho_{0,right} < 1/4$, the equally-massed particles should be the primary choice, since they offer results of better quality around

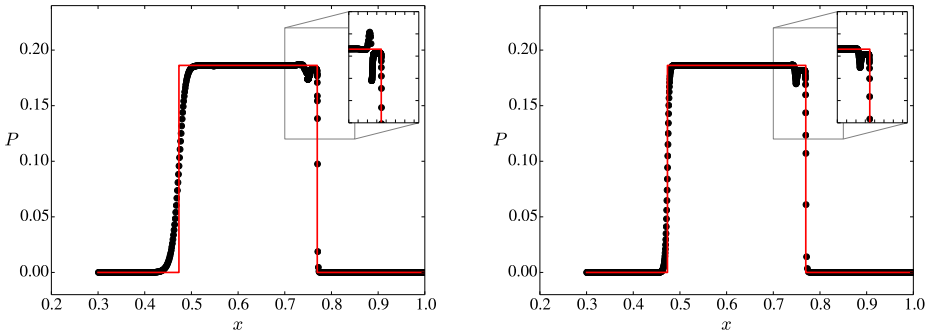

FIGURE 5.5: The asymmetric impact test at $t = 0.3$, for density and soundspeed ratios $1/4$, using the number-density scheme with particles of equal (*left*) and unequal masses (*right*).

	ρ_0	v_0	P_0	P_{ref}	γ
Gas	1	0	1	0	5/3
Gas	0.125	0	0.1	0	5/3
Liquid	1	20	1×10^3	6×10^8	4.4
Liquid	1	20	1	6×10^8	4.4
Liquid	1	0	1	0.6	4.4
Gas	0.05	0	0.01	0	1.4

TABLE 5.1: Initial data and parameters

the contact discontinuity. When computations become heavy due to high density ratios which dictate large numbers of particles to create an acceptable resolution in the low density regions, the use of unequal-mass particles becomes the unique choice, albeit, at the cost of errors in pressure around contact discontinuities. The same suggestion holds in more spatial dimensions for complex geometries, where it is easier to fill the domain with uniformly spaced particles than choosing the spacing in each part of the domain according to the density distribution.

5.2 Shock-tube tests

Three shock-tube tests allow for the evaluation of the developed schemes in describing the propagation of shocks vis-à-vis analytical solutions, which are found via procedures described in Toro [2009] and Plumerault [2009]. In all problems, the

stiffened-gas equation of state delivers the pressure:

$$P(\rho, e) = (\gamma - 1)\rho e - \gamma P_{ref}, \quad c^2 = \frac{\gamma(P_{ref} + P)}{\rho}, \tag{5.3}$$

using the appropriate ratio of heat coefficients γ and reference pressure P_{ref} for each fluid. The ideal-gas equation of state is recovered for $P_{ref} = 0$.

Regarding the optimal parameters for the artificial dissipation terms, we find the following values working well in all examined test cases. An increased —compared to the previous isothermal tests— artificial mass-flux term $a_\rho = 0.5$ is used in all three tests, while $b_\rho = 2.0$ as previously. For the energy conservation equation $a_e = 0.1$ and $b_e = 2.0$ is applied.

5.2.1 Air-Air shock tube

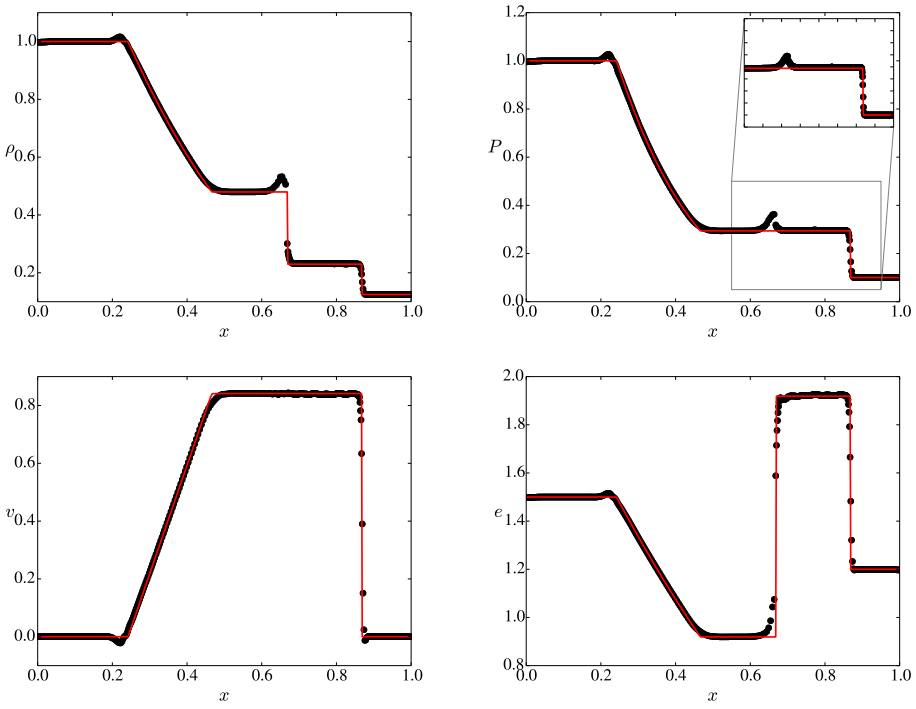

FIGURE 5.6: The Air-Air shock-tube test at $t = 0.2$ for the number-smoothed approach and particles of unequal masses.

The first test is the classic shock-tube benchmark of Sod [1978], which has been addressed since the early development of SPH [Monaghan and Gingold, 1983], for density ratios of $1/4$. Its solution within the standard variational SPH framework is extensively examined by Price [2008] for density ratios of $1/8$, where the use of

the integral equation for mass conservation is flavored along with a system of equal particle masses. There, the differential form of mass conservation is shown to suffer from a singularity at the contact discontinuity, which in our tests is turned into a hump due to the artificial mass-flux term. In Figure 5.6, the solution at $t = 0.2$ is presented using $N = 400$ particles of uniform initial spacing, while in Figure 5.7 $D_L = 0.001$ in the low density region, resulting in 450 particles. A constant time-step of $\Delta t = 5 \cdot 10^{-5}$ is used in both cases. The analytical solution (red solid line) shows a constant pressure through the contact discontinuity and the suggested artificial dissipation terms work towards achieving this fairly well for the SPH solution by suppressing the singularities. For the system of equal masses the singularity is turned into a flat pressure profile around the contact discontinuity, while for the system of unequal masses a hump appears in that region. Obviously, the solution of the former system is closer to the analytical, nevertheless at the cost of extra particles.

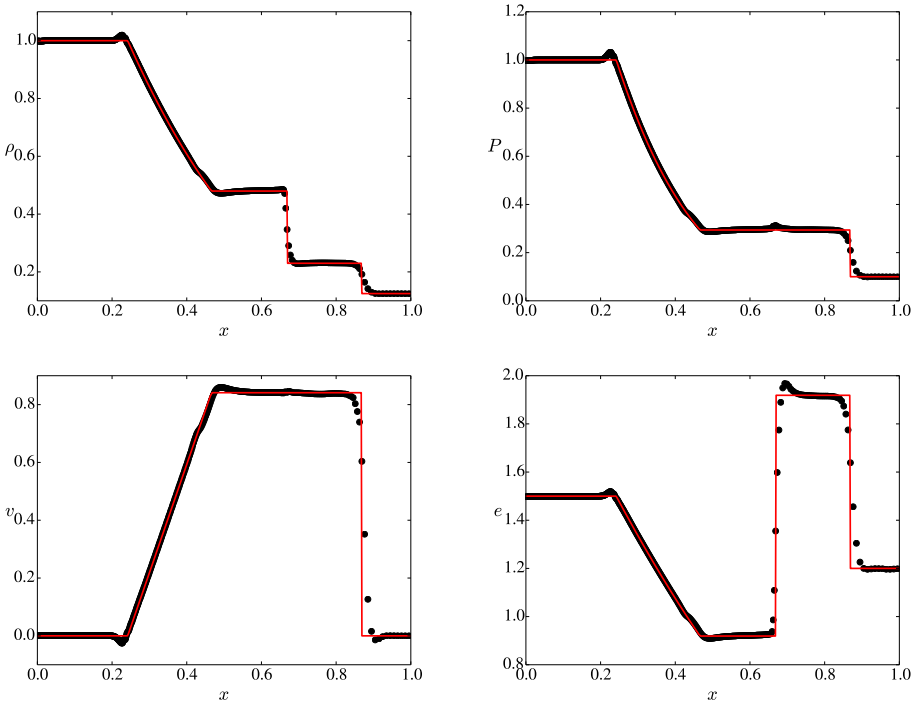

FIGURE 5.7: The Air-Air shock-tube test at $t = 0.2$ for the number-smoothed approach and particles of equal masses.

5.2.2 Liquid-Liquid shock tube

Hosono et al. [2013] concentrate on problems related to mixing and show that standard SPH with only artificial viscosity added gives poor results in their Liquid-Liquid benchmark. This leads them to choose the more complicated variational framework

of Hopkins [2013] for SPH schemes and obtain particle volumes as a function of the internal energy density, rather than mass density (see the related discussion in the Introduction).

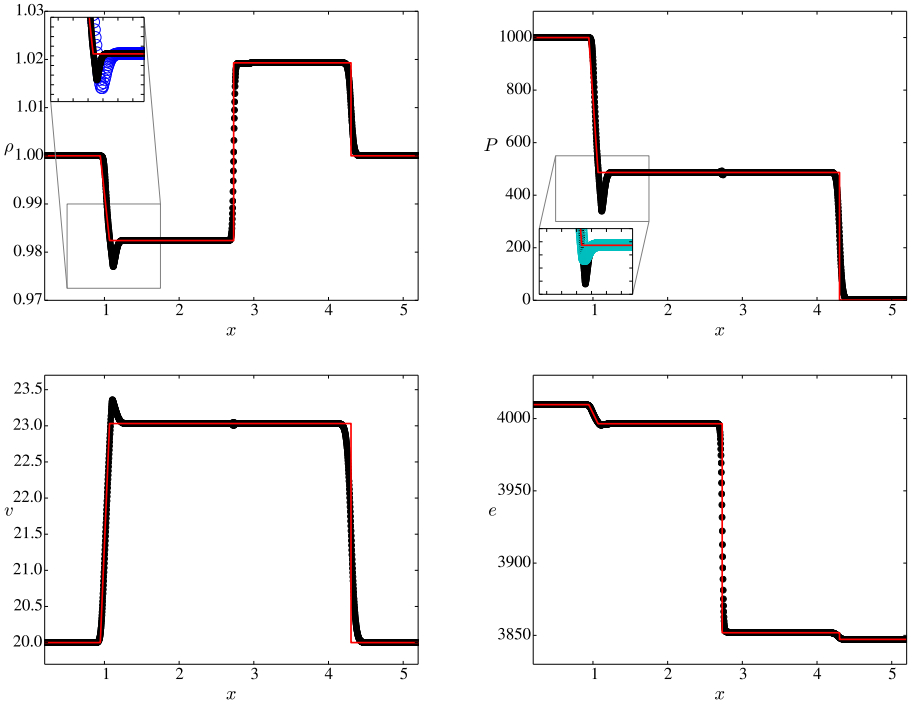

FIGURE 5.8: The Liquid-Liquid shock-tube test at $t = 0.01$ for the number-smoothed approach and particles of unequal masses. In the inset plot of density, convergence with the number of particles is shown and in the inset plot of internal energy, the effect of an increased dissipation parameter in the corresponding variable (more details are provided in the text).

Note that due to the equal "left" and "right" initial densities, the number-smoothed and the mass-smoothed approaches coincide. As it may be seen in Figure 5.8, the scheme is able to capture properly the physics described by the semi-analytical solution. More importantly, the instabilities observed by Hosono et al. [2013] at the contact discontinuity (nearly in the middle of the domain) are canceled. Diffusion in mass proves tantamount to obtaining the observed flat pressure profile. In the inset plot of density, the convergence of the scheme is shown for $N_\ell = 100$ particles per unit length with a constant time-step $\Delta t = 5 \cdot 10^{-5}$ (blue circles) and for a four times finer discretization of $N_\ell = 400$, with $\Delta t = 5 \cdot 10^{-5}$ (black dots). An issue is the error which appears on the left-running wave, which can be lowered using the increased value $a_\rho = 1$. Zisis et al. [2014a] mention that it is completely eliminated if artificial dissipation is added to approaching particles and particles moving apart, instead of only particles moving closer as suggested in Section 4.2. The applicability of that choice in two spatial dimensions has not been confirmed.

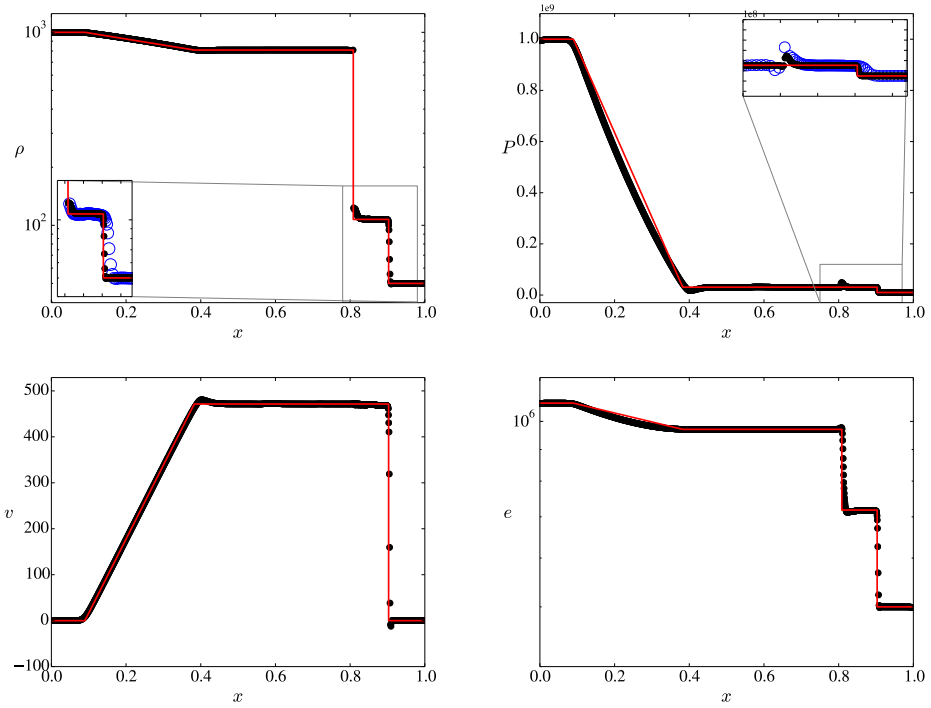

FIGURE 5.9: The Liquid-Gas shock-tube test at $t = 0.0023$ for the number density scheme and particles of unequal masses.

5.2.3 Liquid-Gas shock tube

This test involves a truly multiphase medium in the sense that the initial density profile is discontinuous and the fluid parameters as well. It is a Liquid-Gas shock tube and involves an initial density ratio of $1/20$ and a pressure ratio of $1/100$. In Figure 5.9, the results at $t = 0.0023$ are given, as obtained with $\Delta t = 10^{-8}$ and 800 particles of uniform initial spacing. Of course the minuscule time-step poses restrictions to the use of the algorithm. Similarly to the Air-Air shock-tube, the solution for pressure suffers from the appearance of a hump. This effect is magnified by a factor two in the inset plots of pressure. The inset plot of density zooms in the right-running shock by a factor two. Therein, the convergence of the solution is shown for 200 and 800 particles with blue circles and black dots, respectively. Notice that as the number of particles increases, not only does the steepness of the numerical wave increase, but the numerically predicted wave also comes closer towards the true shock position. Finally, it is evident that the SPH solution manages to capture the left-running rarefaction and the shock which propagates through the low-density fluid.

5.3 Isentropic shock-bar test

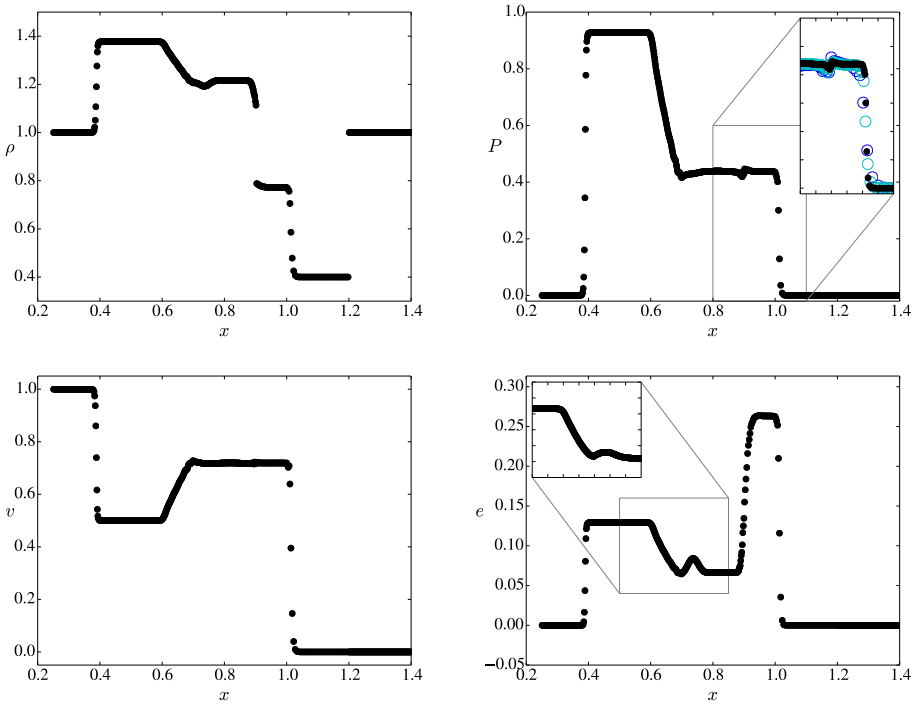

FIGURE 5.10: The isentropic shock-bar test at $t = 0.25$ for the number-density scheme and particles of equal masses.

The last test comprises an ideal —also termed isentropic— hypervelocity impact into an inhomogeneous structure using the nonlinear equation of state:

$$P = \mathrm{K}_1\mu + \mathrm{K}_2\mu^2 + \mathrm{K}_3\mu^3 + \mathrm{B}_0\rho_0 e, \quad \mu = \frac{\rho - \rho_0}{\rho_0}, \tag{5.4}$$

for the parameters defined as:

$$\mathrm{K}_1 = \rho_0\, c_0^2, \quad \mathrm{K}_2 = \mathrm{K}_1(1 + 2(S_0 - 1)), \quad \mathrm{K}_3 = \mathrm{K}_1(2(S_0 - 1) + 3(S_0 - 1)^2). \tag{5.5}$$

Normal stresses in metals during hypervelocity impacts are typically modeled with this type of equations [Hiermaier, 2008]. The main assumption is that the changes of the internal energy take place much faster than the changes of entropy, which are therefore neglected. Parameters and initial conditions are described by:

$$\{\rho_0, v_0, P_0, c_0, S_0, \mathrm{B}_0\} = \begin{cases} \{1, 1, 0, 1, 1.338, 2.0\}, & 0 \leq x < 0.6; \\ \{1, 0, 0, 1, 1.338, 2.0\}, & 0.6 \leq x < 0.8; \\ \{0.4, 0, 0, 0.484, 1.470, 0.67\}, & 0.8 \leq x < 1.2; \\ \{1, 0, 0, 1, 1.338, 2.0\}, & 1.2 \leq x \leq 1.4. \end{cases} \tag{5.6}$$

Values of the projectile's material are reported for Aluminum [Hiermaier, 2008], while the values of the projectile's medium layer material are approximately those reported for a pure epoxy resin [Millett et al., 2005].

No exact solution exists in order to validate the numerical results. However, the purpose of this test is to highlight the importance of the dissipative mass flux term and examine whether its interplay with the artificial heat conduction coefficient a_e delivers a flat pressure distribution across shocked material interfaces. We are interested in the behavior of the number-smoothed approach with particles of equal initial volumes and especially in its ability to suppress any spurious kinks in the distribution of computed variables.

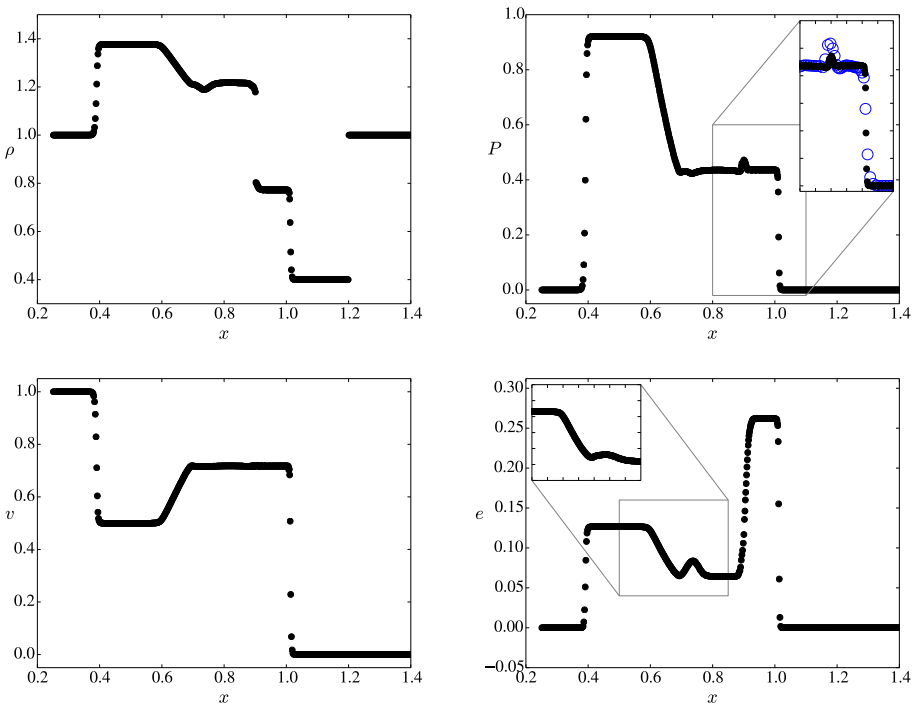

FIGURE 5.11: The isentropic shock-bar test at $t = 0.25$ for the number-density scheme and particles of unequal masses.

In Figure 5.11, results at $t = 0.25$ are shown, using $N_\ell = 400$ particles per unit length. Artificial mass flux ($a_\rho = 0.5$) and artificial conductivity with $a_e = 0.5$ are used.

Similarly to the isothermal impact test, the use of dissipative mass flux smoothens out spurious kinks on the shocked interface and provides continuous and almost uniform pressure distribution through the contact discontinuity. A flat pressure distribution in that region is expected due to the Riemann structure of the problem. Regarding the early stages of the impact, the dissipative heat term removes the energy which is

localized at the impact site. This localization is due to the abrupt change of kinetic energy into internal energy during an impact of velocity as high as the material's speed of sound. Actually, the result of the localized energy is apparent in the later stages of the experiment; notice a wave succeeding the rarefaction wave in the plots of e, in both Figures 5.10 and 5.11. In the inset plot of internal energy, a substantially increased value of $a_e = 2.0$ is used and it achieves to diminish the wave. Lacking an analytical solution, we cannot safely conclude whether this wave is an artefact. Nevertheless, there is a major argument against the existence of this wave. For $a_e = 0$ and normal $a_\rho = 0.5$, the wave is suppressed in the density profile, however not for the internal energy. By increasing the artificial dissipation of the internal energy, the wave is increasingly suppressed. The localized internal energy is smoothed out to a broader region, does not affect the strength of the shock and works independently of the dissipative mass term. Therefore, increased values of a_e should be used with caution, if at all.

At this point a comment regarding the choice of the artificial dissipation parameters is necessary, especially in cases where there is no reference solution. We aim at arriving to a set of optimal parameters, which can be used universally, or at least in a large set of problems. To this end, we examine different parameter values. In specific, we keep the artificial viscosity parameter the same as in the literature ($a_v = 1$) and in the first two experiments (Section 5.1 and 5.2.1), we examine different values for the artificial dissipative mass a_ρ. The one performing the best is recorded and used in the following experiment, to verify that it delivers good results as well. In the latest test, the isentropic shock-bar, we discarded a higher value for the artificial conductivity a_e, exactly because it produced over-smoothing of waves. Upon verifying that the parameter values also work well in two-dimensional geometries (Section 5.4), the problems of Section 5.5 and Chapter 6 are successfully solved with the single set of parameters. Certainly, artificial dissipation parameters are not a panacea and one could consider Riemann solvers. That is, of course, at the expense of more involved solution strategies and more computational effort.

5.4 Shock-chamber tests

Apart from the one-dimensional experiments, the ability of the developed SPH schemes to describe the propagation of shocks is also examined in a domain of two spatial dimensions. To this end, both previous tests are performed in two-dimensional setups, in what can be referred to as *shock-chamber tests*.

Initially, fluid of high density and high pressure is at rest in the square $\mathcal{G}_{\text{in}} = \{x_1, x_2 : \{|x_1| < 0.5\} \cap \{|x_2| < 0.5\}\}$ and it is encapsulated within a fluid of lower density and pressure. The whole problem domain is the square $\mathcal{G}_{\text{box}} = \{x_1, x_2 : \{|x_1| < 3\} \cap \{|x_2| < 3\}\}$, where particles outside the square $\mathcal{G} = \{x_1, x_2 : \{|x_1| < 2.5\} \cap \{|x_2| < 2.5\}\}$ are boundary particles and at every time-step their velocity is kept fixed at zero. The use of the square geometry instead of a smooth circular one, makes the test more demanding, due to the concentration of stresses on the corners.

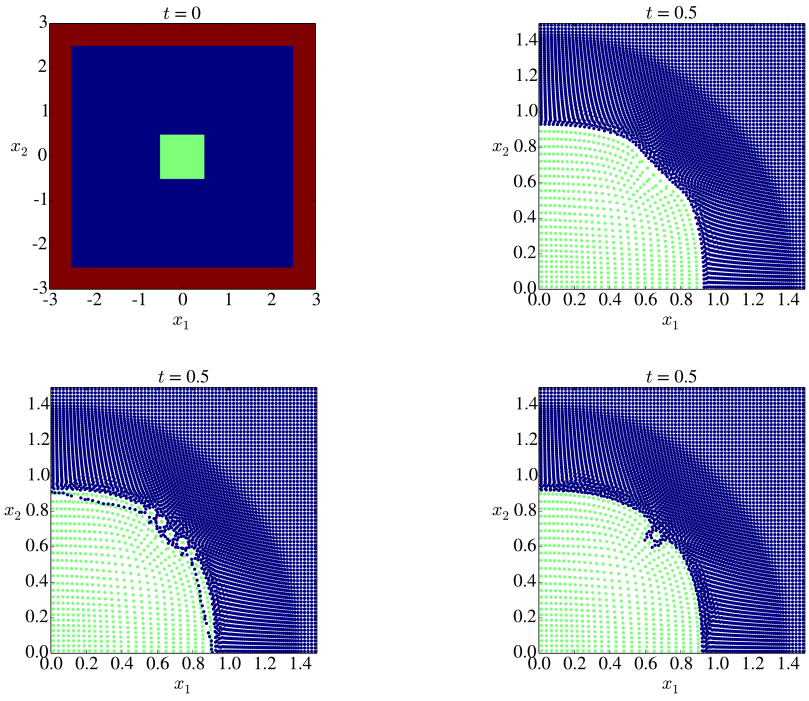

FIGURE 5.12: The whole computational domain at $t = 0$ and the configurations of the number, mass and volume-smoothed media at $t = 0.5$ for the Air-Air shock chamber.

The abrupt expansion of the high-density fluid generates a shock which propagates through the low-density fluid and a rarefaction wave which moves towards the center of the chamber. After the expansion wave collapses to the center of the chamber, it reverses its direction and starts moving towards the boundaries of the chamber. Thus, it provides a distinct wave pattern, which we investigate at $t = 0.5$. Lacking the analytical solution and following Zisis et al. [2015a], we consider as reference numerical solution, the solution obtained using the Arbitrary Lagrangian Eulerian (ALE) multi-material methodology of Aquelet et al. [2005], implemented in the LS-DYNA code, using 1000 elements.

In order to realize the SPH initial particle configuration, a number of particles per unit length N_ℓ is chosen. This number defines a Cartesian grid for the square problem domain. Particles are placed in the middle of the grid's cells. The initial configuration appears in the upper left subplot of Figure 5.12, with the colors marking the species of the particles: high density gas (green), low density gas (blue) and boundaries (red). Note that boundaries of finite thickness are typical in SPH. The three spatial resolutions, which are examined, correspond to $N_\ell \in \{25, 50, 100\}$ particles per unit length. The values $a_\rho = 0.5$, $a_v = 1$ and $a_e = 0.1$ are used, unless mentioned differently.

5.4.1 Air-Air

The upper right and the lower subplots of Figure 5.12 show the computations for $N_\ell = 50$, at time $t = 0.5$, using the three different schemes derived from the number-smoothed (upper right), the mass-smoothed (lower left) and the volume-smoothed (lower right) media.

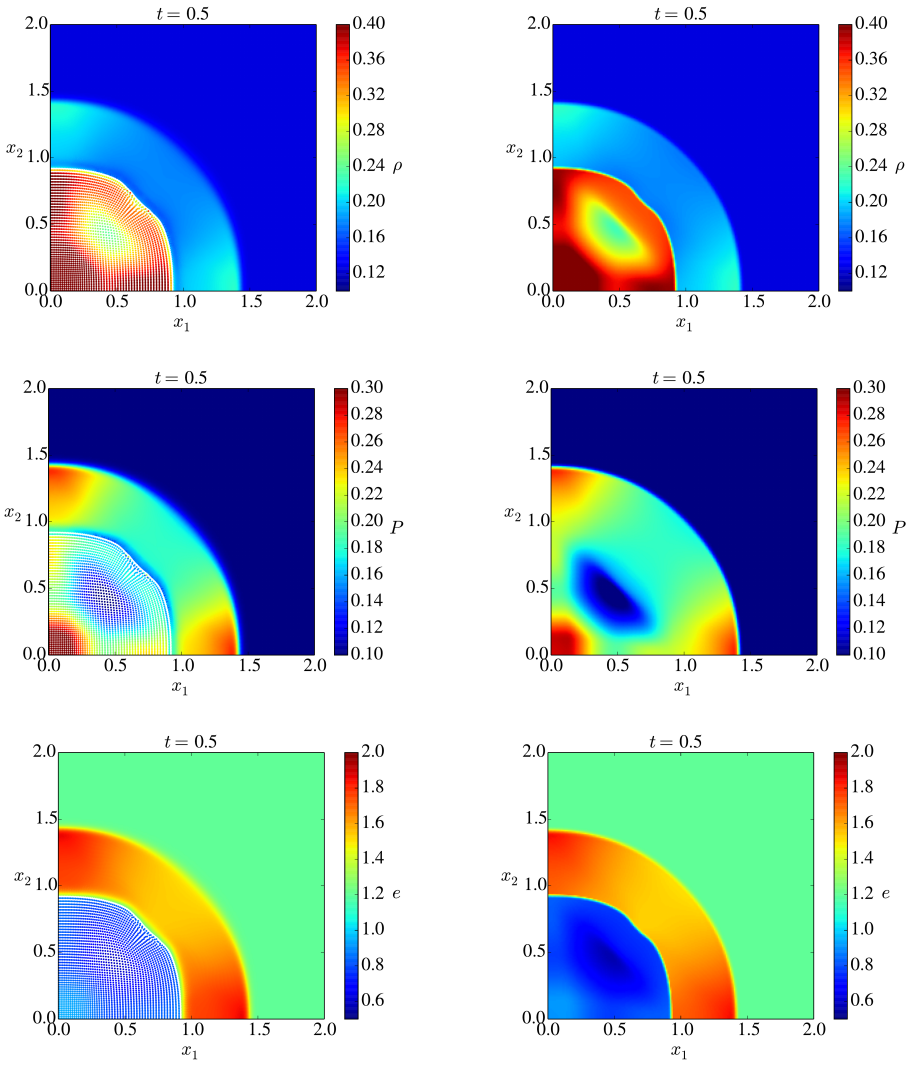

FIGURE 5.13: The Air-Air shock-chamber at $t = 0.5$, solved by SPH (*left*) and ALE (*right*).

With the colors referring to the species of each particle, it can be observed that for the mass-smoothed and the volume-smoothed media particles of initially low-density

gas infiltrate the region of high-density gas. There are two issues connected to this instability. First and foremost, it is not consistent to the corresponding continuum model, also apparent in the ALE solution presented later, which dictates that the high-density gas expands following a smooth topology and that no mixing occurs. Second, there is a direct computational consequence. The number of neighbors in that region increases significantly leading to increased number density $\tilde{n}(x_i)$ and thus leading to smaller smoothing lengths $h(n_i) = 1.2n_i^{-1/2}$. Subsequently, the smaller smoothing length reduces the time-step (see Section 4.3) and thus, for the mass-smoothed medium, twice as many time-steps are necessary to arrive at $t = 0.5$.

The described instability presents some evidence of the superiority of the number-smoothed medium, as compared to when particles of unequal masses are used for fully compressible multiphase computations. In support of this argument, recall the erroneous results of the other two schemes in the one-dimensional impact in Section 5.1. For these reasons, the following tests exclusively concern the behavior of the number-density scheme.

In Figure 5.13, the left triad of plots present the SPH solution for density, pressure and internal energy respectively, with the finest resolution of $N_\ell = 100$ particles per unit length. The right triad of plots show the ALE solution for the same quantities. By and large, the SPH solution captures the wave pattern described by the ALE solution. The SPH solution tends to overestimate the zones of high pressure downstream the contact discontinuity.

For closer examination of the previous issue, we plot the problem's solution along the positive x_1 semi-axis of the domain, in Figure 5.14. For the SPH solution, we choose the particles found within a maximal distance of h_i from the x_1 axis. The magnitudes of density, pressure and internal energy appear from top to bottom respectively and they are compared to the corresponding magnitudes of the ALE reference solution. Convergence is examined on the left column and the influence of the artificial dissipation parameters on the right. The legends for each column are in the plots of internal energy.

Regarding the left triad of plots in Figure 5.14, they show that the SPH solution converges as the number of particles per unit length $N_\ell = \{25, 50, 100\}$ increases. Besides this observation, we note that although the SPH solution follows the behavior of the ALE solution, there is an overestimation of all quantities to the left of the contact discontinuity (found approximately at $x_1 = 1.0$). This overestimation appears only after the rarefaction wave passed that region and increased the interparticle distances. This difference in the interparticle distances within the two regions is also visible in the left plots of Figure 5.13. It is reasonable to assume that this effect can possibly be treated with a particle generation algorithm, like the one of Vacondio et al. [2012, 2016]. In the inset plots, the solution refers to the use of the approximate signal velocity from Equation 4.24 instead of the Riemann-like term. In that case, notice in the plot of density that the SPH solution runs ahead the shock, an effect which is not observed when the Riemann-like term is used. Moreover, the pressure plot focuses on the region around the contact discontinuity, and makes obvious that the approximate signal velocity is unable to successfully treat the instability at the contact

discontinuity.

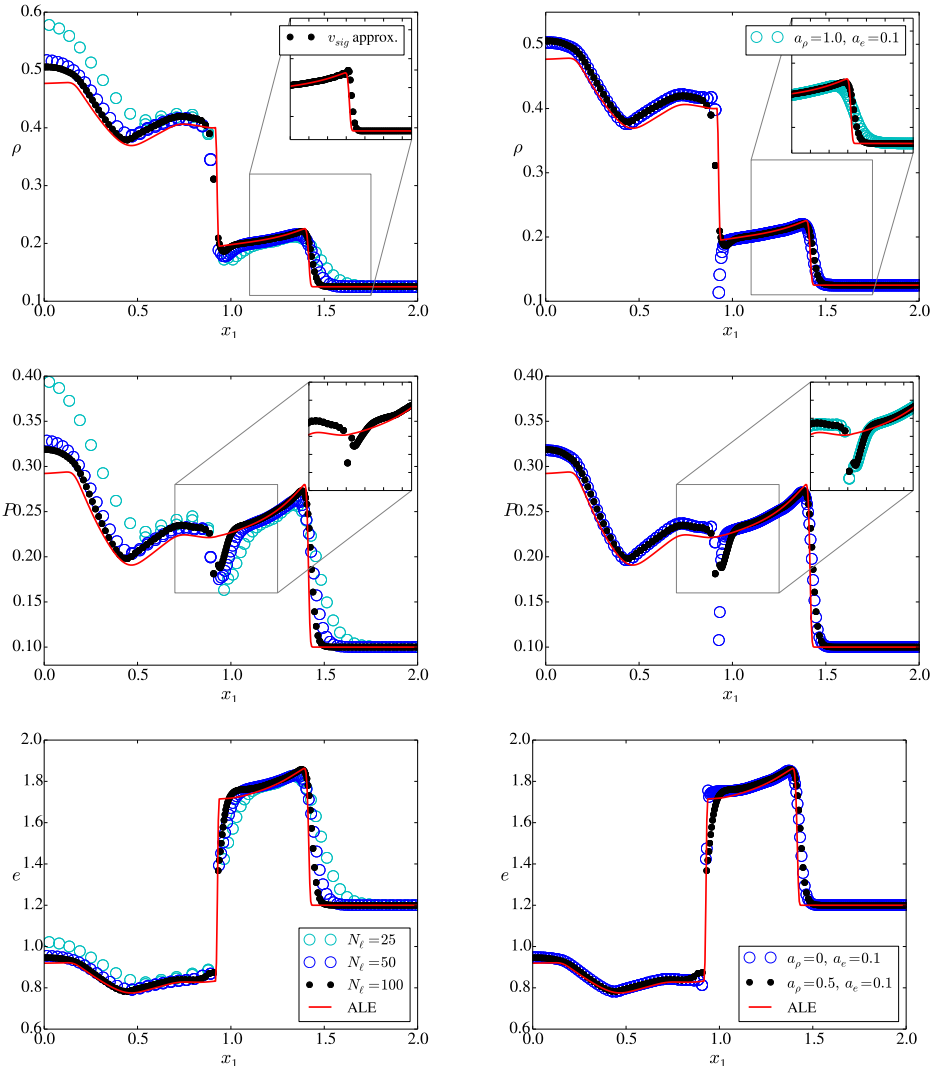

FIGURE 5.14: Convergence (*left*) and influence of the dissipative terms (*right*) for the Air-Air shock chamber at $t = 0.5$.

The effect of the artificial mass-flux term is studied in the right triad of plots in Figure 5.14. The reason for this investigation is that the addition of the artificial mass-flux term to the evolution of density, influences the calculated speed of sound $c_s = (\partial P/\partial \rho)_s = (\gamma - 1)\, e$ via the computed thermal energy. A large value for a_ρ might lead to misprediction of the sound speed. For $N_\ell = 100$, we examine the chosen values $a_\rho = 0.5$ and $a_e = 0.1$ (black dots), against the values $a_\rho = a_e = 0$ (blue circles). One may recognize the healing effect of dissipation, by looking at the plots of

density and pressure around the contact discontinuity in the absence of dissipation, where kinks appear. In the inset plots (cyan circles), we examine possible merits of increasing the dissipation parameter to $a_\rho = 1$. The results in density suggest that the shock is smoothed further. The predicted position of the shock is independent of the value of a_ρ. With respect to the contact discontinuity, the plot of pressure shows that the increased value of a_ρ offers no advantage.

5.4.2 Liquid-Gas

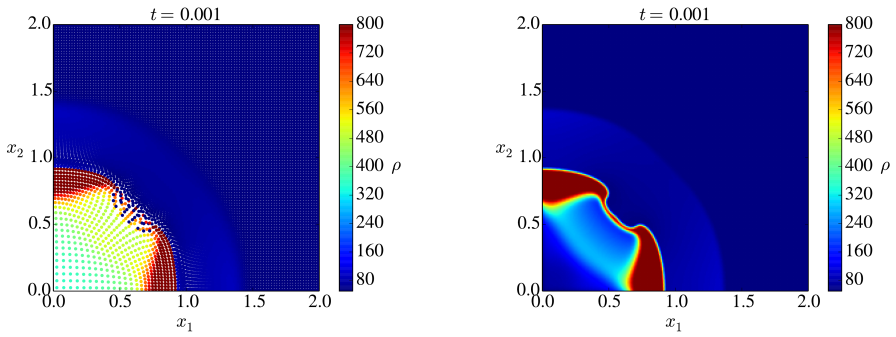

FIGURE 5.15: The Liquid-Gas shock chamber at $t = 0.001$, using SPH (*right*) and ALE (*left*).

In the same non-smooth geometry (upper left plot of Figure 5.12), the number-smoothed SPH algorithm is employed for the Liquid-Gas problem, with the initial conditions shown in Table 5.1. For $N_\ell = 50$, the density plot at $t = 0.001$ appears in the left subplot of Figure 5.15, and is compared to the ALE solution (right subplot). Although it can be argued that the SPH solution is in overall accordance with the ALE solution, a certain kind of instability is observed around the point $(x_1, x_2) = (0.6, 0.6)$. Some lower density particles (blue dots) appear to neighbor with high density particles (yellow and red dots). Indeed, looking at the left subplot of Figure 5.16, particles of Air (blue dots) infiltrate the Water region (green dots) for $N_\ell = 50$. As a direct consequence, the number of neighbors of the infiltrated air particles increases extremely, making the processing of each time-step dramatically slow and making it implausible to collect results for $N_\ell = 100$ at $t = 0.001$. Indicatively, in that latter case, there are particles with the number of neighbors exceeding $13,000$.

Recall that in the Air-Air problem, the instability of low-density particles migrating to the high-density region only appears for schemes other than the number-smoothed. The present test shows that the number-smoothed scheme is not a panacea for instabilities of this kind. The instabilities appear due to a synergy of non-smooth geometries, high density ratios and schemes not respecting the smoothing length coupling to the number density.

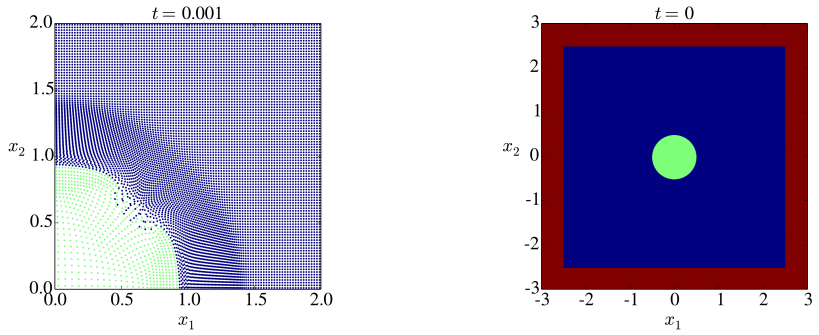

FIGURE 5.16: Particle species for the Liquid-Gas shock-chamber at $t = 0.001$ on the left and the problem domain in the Liquid-Gas shock-chamber with circular inner geometry.

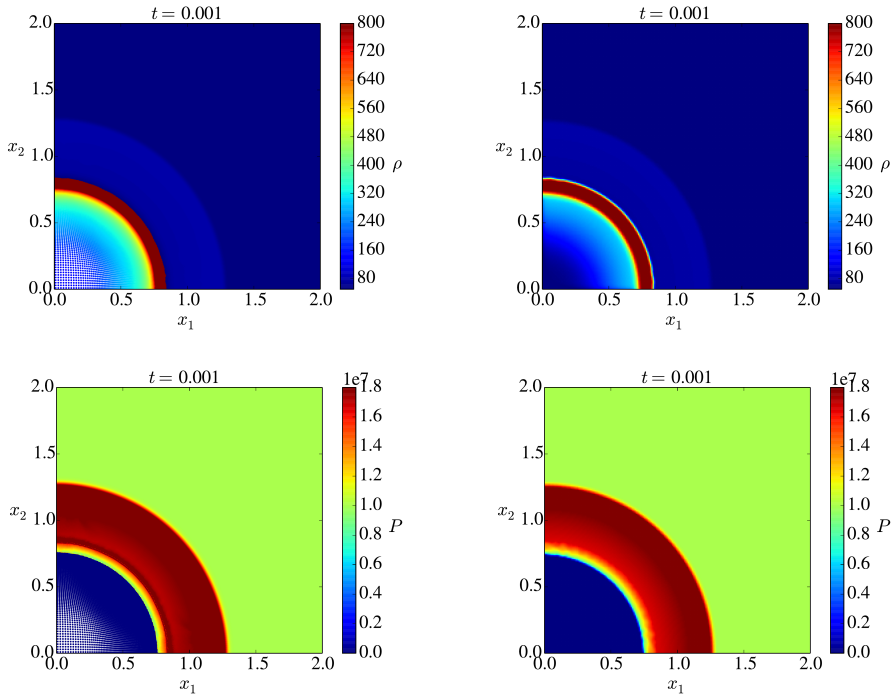

FIGURE 5.17: The SPH solution (*left*) and the ALE solution (*right*) for the Water-Air shock chamber with the circuar inner geometry, at $t = 0.001$.

To clarify the last statement, let us examine the problem with the same initial data, but with a smooth geometry. Instead of a rectangular water region, the circular one shown in the right subplot of Figure 5.16 is used, corresponding to $\mathcal{G}_{\text{in}} = \{x_1, x_2 : \{(x_1^2 + x_2^2)^{1/2} < 0.5\}\}$.

The left column of Figure 5.17, shows the SPH solution for density, pressure and internal energy profiles, at $t = 0.001$, regarding $N_\ell = 200$ particles per unit length. Since the problem is successfully solved for $N_\ell > 50$, we infer that the instability, which appears in the corresponding problem of non-smooth geometry, is due to the geometry rather than being an inherent problem of the algorithm with high-density ratios.

5.5 Shock-bubble interaction test

We now concentrate on the experimental work of Haas and Sturtevant [1987], against which we validate our computational results. They experimented with several cases of single spherical or cylindrical bubbles hit by a shock wave, according to the following configuration. In the low-density compartment of a wind tunnel, a bubble filled with another gas rather than air and of different density, rests in equilibrium with the surrounding air. The shock wave travels through the air and upon hitting the bubble, several wave reflections and transmissions occur, followed by the creation of complex interfaces, since the two fluids hardly mix. The latter effect is due to the high velocity of the shock wave; the bubble is overpassed in almost 100 μs only.

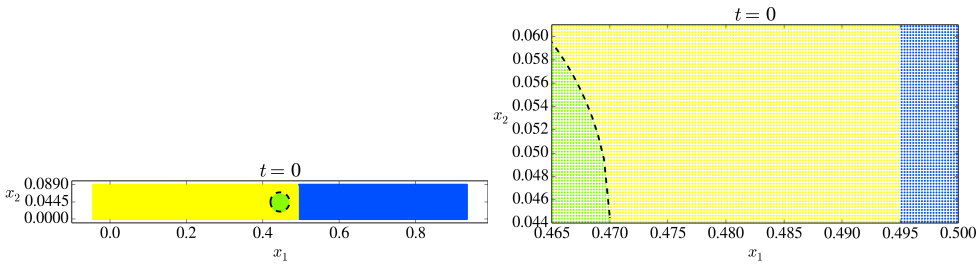

FIGURE 5.18: The computational domain and a detail of the particle configuration.

The experiments of Haas and Sturtevant [1987] also exhibit that the resulting wave patterns and bubble deformations strongly depend on the gas inside the bubble. They used Helium (slightly contaminated with air) and Refrigerant 22 (R22, a refrigerator gas). The former has a speed of sound higher than that of air, the latter a lower.

As the shock sweeps over the inhomogeneity, the bubble's volume changes because of compression and the induced differential motions. The latter, if they are normal to the axis of symmetry, also lead to compression, while oblique and tangential off-axis interactions lead to shear. From this point of view, vorticity is produced because of the misalignment of the gradients in pressure and density (or entropy). The initial deformation of the inhomogeneity can also be interpreted in terms of the Rayleigh-Taylor instability of accelerated, curved interfaces separating fluids of different density; the acceleration is caused by the shock wave. The shock-induced Rayleigh-Taylor instability of a sinusoidally perturbed plane interface is referred to

	ρ_0	$v_{0,1}$	$v_{0,2}$	P_0	γ
Air 1	1.4	0	0	1.0	1.4
Air 2	1.92691	-0.33361	0	1.5698	1.4
R22	4.41540	0	0	1.0	1.249

TABLE 5.2: Initial data and parameters

as the Richtmyer-Meshkov instability. The latter instabilities, also play a role in the process described further on.

Several computational studies use the aforementioned experiments for the purpose of validating numerical schemes, typically focusing on the cases of the cylindrical bubbles. One of the earliest and perhaps the most detailed is the study of Quirk and Karni [1996], who focus on the magnitude of the gradient of density; thus, their computational images resemble the Schlieren images of the experimental study. In the present study, we take into account the results of Kreeft and Koren [2010], who plot the density and pressure fields. Thus, in addition to the primary comparison, that is the SPH results *vis-á-vis* the experimental result, a secondary comparison is made, with respect to the differences in the density field between the SPH result and those reported by Kreeft and Koren [2010]. It should be noted, that they solve a five-equation model for inviscid, non-heat-conducting, compressible two-fluid flow, using a Finite Volume scheme equipped with an approximate Riemann solver. Some comments regarding their different solution strategy are necessary. First, using an Eulerian description of the flow field makes the detection of each species challenging, a problem which their algorithm treats. On the other hand, this comes with ease for SPH. Second, they use a Riemann solver, which inevitably makes their shock description superior to the one obtained with our artificial-dissipation approach. All ideal gas parameters used in the present study are from Kreeft and Koren [2010] and can be found in Table 5.2, with all values of the velocity components scaled with 343 m/s, the nominal speed of sound of air. Therefore, the normalized time t^* of the computation refers to the time scale $\tau = L/c_{\text{air}} = 1\,\text{m}/343\,\text{m/s} = 2.915\,452\,\text{ms}$. Note that the length scale is comparable to the total length of the wind tunnel, which is 0.89m. The width is 0.089m and the bubble diameter $D = 0.05$m, as is shown in Figure 5.18.

In order to replicate the solid boundaries of the experimental configuration, following Quirk and Karni [1996], we enforce reflective boundary conditions along the lines $y = 0$ and $y = 0.089\,\text{m}$. This is achieved by creating at every time-step on the upper and lower edges, a layer of ghost particles of thickness three times the maximum smoothing length of all particles. Two additional sets of fixed boundary particles are constructed to the left of $x = 0$ and to the right of $x = 0.89\,\text{m}$. In any case, these latter boundaries do not affect the computational result, since no waves arrive there within the examined time period.

The presented results refer to $N_\ell = 4000$ particles per unit length placed in the

computational domain with a rectangular particle formation, leading to around 1.4×10^6 particles. A fixed time-step $\Delta t^* = 5 \times 10^{-6}$ s is used until the final observation time $t^* = 4 \times 10^{-1}$ s. Note that for this specific test, artificial conductivity is switched off ($a_\rho = 0$), because it otherwise produces an abrupt smoothing of the bubble, due to the imbalance of its internal energy and the internal energy of the surrounding air. A choice, which is not examined, is to use the signal velocity of Price [2008], which works only for pressure differences and is discussed in Section 4.2.

Haas and Sturtevant [1987] produced a series of Schlieren images for a time span of almost 1000 μs after impact (that is 370τ) and these are the images to which we compare our results. In the computational setup, the initial distance of the shock front from the bubble's surface is such that the shock arrives there at $t^* = 7.5\tau$, still as uncurved, normal shock, so that "start effects" in the smearing of the shock easily appear before any interaction, as suggested by Quirk and Karni [1996]. Note that the latter study uses an extreme initial distance of $4.5D$, while the distance used in our study corresponds to $1D$, in order to save computational time.

Figures 5.19-5.21, depict the evolution of the shock-bubble interaction as captured at the same post impact time instances by: 1) the Schlieren images of the experiment by Haas and Sturtevant [1987] on the left, 2) the density profile from the FV scheme of Kreeft and Koren [2010] in the middle and, 3) the density profile of the number-smoothed SPH scheme on the right. The colors appearing in the latter two results are scaled in approximately the same way and thus a qualitative comparison can be made. For the Schlieren images, the end of the cylindrical bubble coincides with the observation window and thus the outline of initial position of the bubble is visible. The T-shaped structure at the bottom supports the bubble. On the SPH plots, the black dashed line marks the initial position of the bubble.

When the shock arrives at the R22-air interface, it is refracted inside the bubble, while a reflected wave is created upstream the bubble. At the same time, the incident shock sweeps over the bubble. Notice that all three waves appear in the computational results for t =55 μs, with slightly different patterns. Additionally, there is a distinct feature for each of the two computational methods. The FV scheme, equipped with an approximate Riemann-solver, seems to predict a thin slice of nominal-R22 density upstream the shock (green-colored region between blue and orange in the FV plot). Kreeft and Koren [2010] attribute it to numerical spreading. This region plays a role in mixing, which becomes obvious in later time. Moreover, the incident and the refracted shocks are represented as sharp discontinuities. On the contrary, the number-smoothed SPH scheme offers a sharp upstream air-R22 interface and tends to over-smooth the two shocks.

At the next two observation instances, t =115 μs and t =135 μs after impact, the reflected wave is already out of the observation window. In the later time instance, the experimental image shows that there are two symmetric waves arriving as reflections on the solid boundaries, from the top and bottom wall of the wind tunnel. The shock wave through the bubble starts curving and converging to the downstream interface of the bubble, while it should be noticed that the incident and the refracted shocks remain connected. Haas and Sturtevant [1987] consider this to be the reason

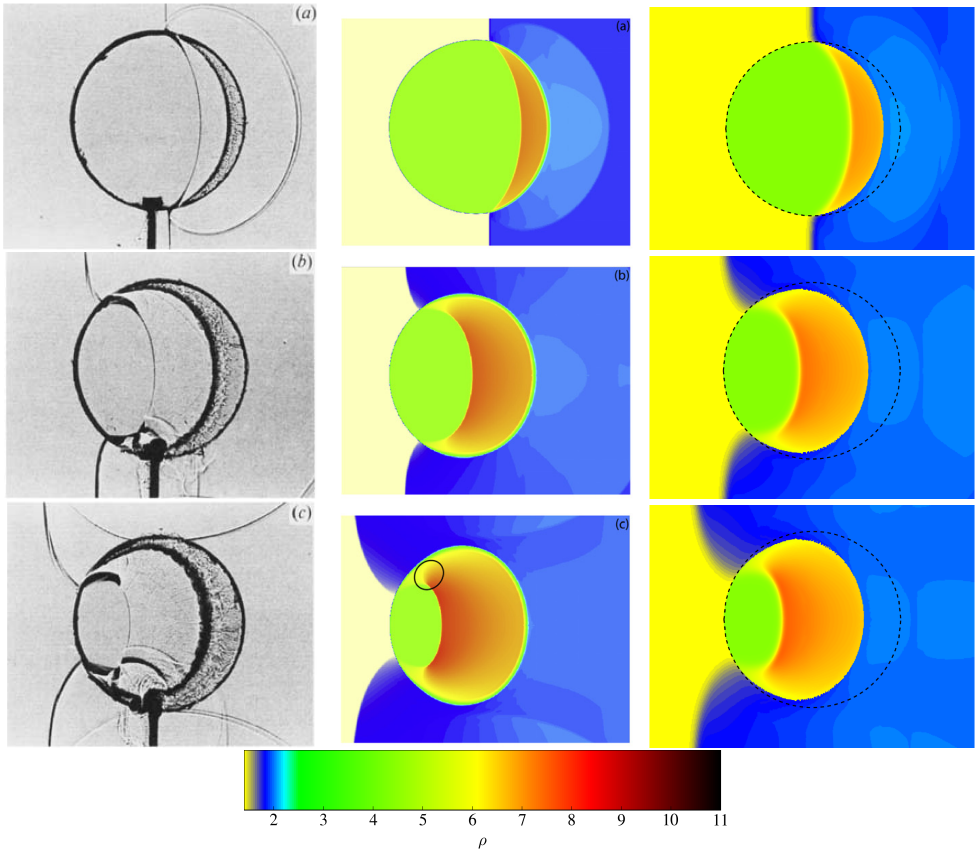

FIGURE 5.19: Shock-bubble R22 interaction 55, 115 and 135 μs after impact.

of a striking contrast between the thickness of the shock front in the curved regions and the shock front in the middle of the bubble. Effectively, as Kreeft and Koren [2010] mention, pressure waves arise there. The fact that the two shocks remain connected is evident in both the computational results, being rather proclaimed by the FV computation and quite smoothed in the SPH result.

In the next post-impact experimental image, at t =187 μs, the refracted wave, curved at the top and the bottom of the bubble, finally focuses on the downstream air-R22 interface. The thick black lines imply high densities. These high density spots are finely resolved in the computational results of the FV scheme and are rather smoothed out in the SPH results. Furthermore, the experimental image shows that the two reflected waves from the top and the bottom of the wind tunnel have crossed each other, creating a distinct wave pattern, which is resolved by both computational methods.

Until this stage of the process, the bubble is not set in motion as a whole, but it rather experienced a reduction of its volume, due to shock compression. Upon focusing, the refracted shock sets the whole bubble in motion, which can be seen displaced

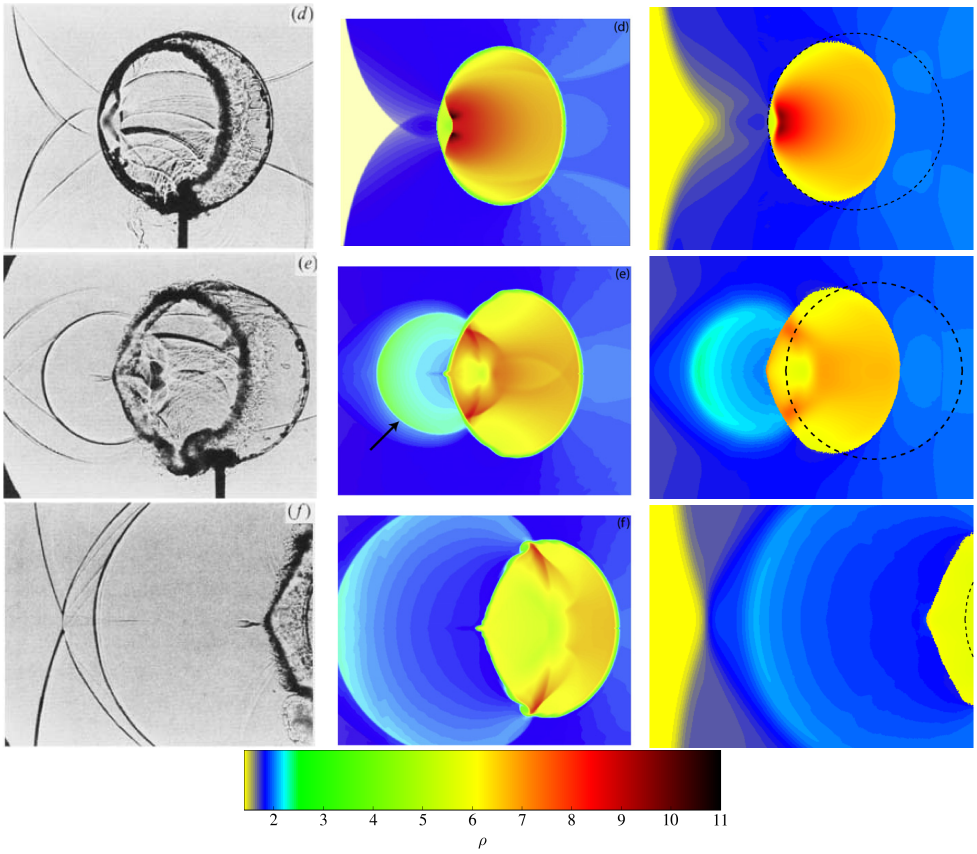

FIGURE 5.20: Shock-bubble R22 interaction 187, 247 and 318 μs after impact.

from its initial position at t =247 μs. At the same time, the focused shock creates a radial expansion wave outside the bubble, and a rather complex wave structure moving to the right, inside the deformed bubble. Notice that the overall wave pattern is very well captured by both numerical methods, with the FV scheme producing sharper wave surfaces. It should be underlined that the top-bottom asymmetries in the experiment are due to the T-shaped support structure.

At time t =318 μs after impact, the radially expanding wave almost catches up with the incident shock front and creates a crossed wave pattern on the left part of the experimental image. Note that this wave pattern is accurately described by the SPH solution. Regarding the computational results with FV, the surrounding region of the bubble is clearly perturbed (recall from the first instance that it is recognized as a region where mixing takes place) and Richtmyer-Meshkov instabilities start forming.

In the following observation instance, t = 342 μs post-impact, the internal back-reflected wave is visible in the experimental image and is reproduced by the computational results. Additionally, the computational results are able to capture the waves outside the bubble. This is especially portrayed by the FV scheme. With respect to

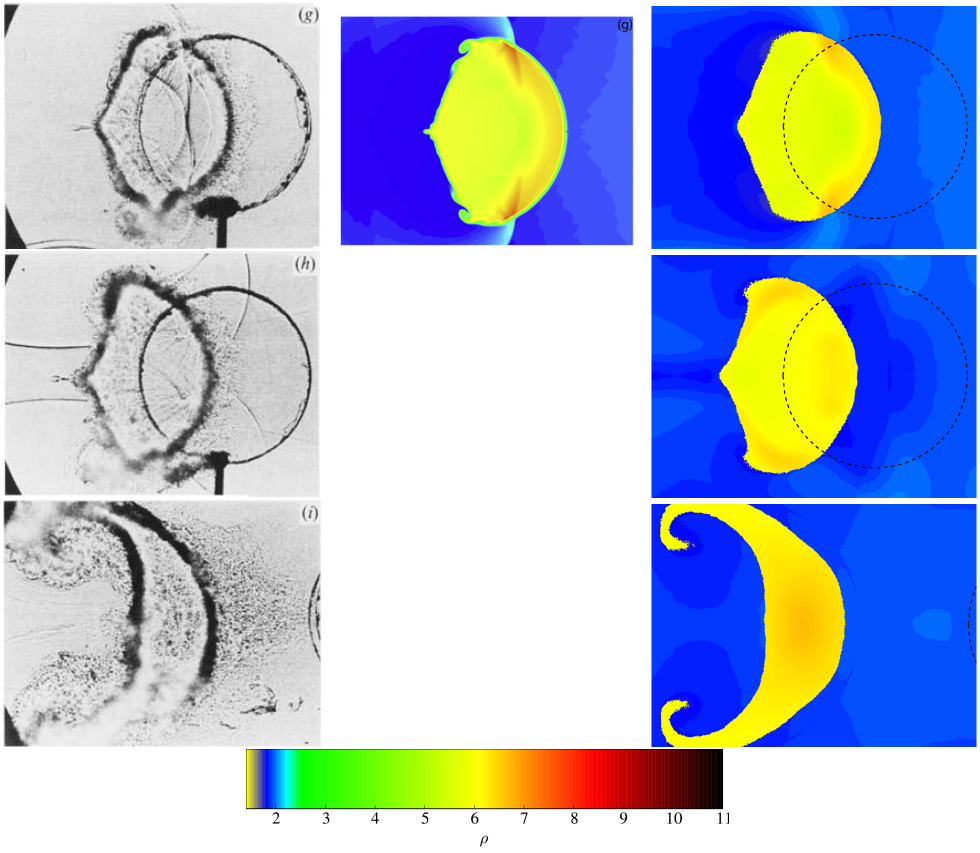

FIGURE 5.21: Shock-bubble R22 interaction 342, 417 and 1020 μs after impact.

the Richmyer-Meshkov instabilities, they can be seen growing on the interface of the bubble in the experiment, while they are pronounced in the FV results and absent in the SPH results.

At $t = 417\,\mu$s after impact, the wave pattern in the experiment is quite descriptive regarding the exterior transmission of the back-scattered wave. The corresponding waves are also visible in the SPH results. Here, there are no data available for the FV scheme.

The last observation instance, $t = 1020\,\mu$ s following the impact, finds the bubble deformed into a vortex pair. Compared to its shape in the previous instances, the bubble expanded in width during the formation of vortices by engulfing fluid across its way to the left. Furthermore, it is evident that the process of breakup initiated. The SPH result is able to resolve the strongly deformed shape.

The SPH scheme coming from the number-smoothed medium, with particles of unequal masses, simulates the evolution of the shock-bubble interaction very well. Compared to the results obtained with the FV scheme with Riemann solver of Kreeft

and Koren [2010], the SPH scheme produces sharper interfaces, but more smeared shock fronts. Comparison of the SPH result with the Schlieren images shows that the developed SPH scheme can accurately resolve the complex wave patterns of the physical process until its latest stages. More importantly, it achieves this in a straightforward manner —that is without using any additional special treatments of the flow— and in a relatively easy computational setup.

There are two effects which appear in the experiment, however not in the SPH solution. First, the experiment shows that Richtmyer-Meshkov instabilities grow on the interface of the two fluids while these are not observed in the SPH solution. These instabilities are reproduced by the FV scheme. Second, in the last image of the experiment, the deformed bubble breaks up; an effect which does not occur in the SPH solution. All in all, results imply that SPH suppresses mixing.

The ability of SPH to resolve instabilities of this type (Kelvin-Helmholtz, Rayleigh-Taylor or Richtmyer-Meshkov) and mixing is debated in the literature of SPH. The most prominent study is the one by Agertz et al. [2007]. Using various SPH algorithms and grid-based methods, they run a test involving a cold cloud engulfed in a hot wind; by and large, it is similar to the shock-bubble interaction problem. They observe good agreement of all approaches in the early stages of the process. However, as soon as the large-scale instabilities have grown, the SPH results diverge by suppressing mixing.

Agertz et al. [2007] attribute this effect to an inherent vice of SPH. They continue that SPH, at least in the standard usage and formulation, inaccurately handles situations where density gradients are present. In these situations, SPH particles of low density close to high-density regions suffer erroneous pressure forces due to the asymmetric density within the smoothing kernel. This causes a gap between regions of high-density contrast, essentially decoupling the different phases of the fluid.

Examining the details of the final SPH result in Figure 5.21, we see that for our approach there is no gap between the phases. Having excluded this possibility, we turn to the study of Price [2008] who concentrates on Kelvin-Helmholtz instabilities — mixing due to shearing motion of fluid with different densities— and exhibits that this problem relates to the inaccurate description of pressure across contact discontinuities, where a flat profile is expected. Similar conclusions appear for Richtmyer-Meshkov instabilities [Borve and Price, 2009]. As a treatment, it is advised to use: 1) particles of equal masses, 2) the integral form of mass conservation, $\tilde{\rho}_i = m \sum_j W_{ij}(h_i)$ solved simultaneously with $h_i = \eta(m/\tilde{\rho})^{1/d}$), and 3) Riemann-like artificial dissipation terms as in Monaghan [1997] and 4) artificial dissipation for the evolution of the total energy (which is the conserved quantity rather than the internal energy).

From the four stated ingredients, our algorithm accommodates the latter two, while it cannot use the former two, due to the following specific reasons. In Section 4.4, we argued that the use of equal masses imposes a serious geometrical restriction and the particle filling of complex domains, including inhomogeneous media, cannot be a generic procedure in that case. Additionally, the use of the integral equation for mass is problematic for bounded domains, since it leads to zeroth order errors *a priori*, as it

is pointed out in Section 3.4. This is not critical for the shock-bubble interaction, where the computational domain is extended to enforce boundary conditions. However, it becomes a serious limitation in the problems of the next chapter which exclusively involve free boundaries.

Furthermore, Price [2008] uses the accurate pressure results in the Air-Air shock tube to decide on the ability of his algorithm to describe mixing. By doing the same, our results of Figures 5.6 and 5.7 imply that the equality of masses seems to be the limitation of our algorithm, rather than the differential form of mass conservation. Finally, it should be underlined that the coupling of the smoothing length with the local number-density is tantamount to capturing correctly the physics around discontinuities.

CHAPTER 6

Hypervelocity impacts

Perhaps the most exotic processes involving shock propagation through solid media, are hypervelocity impacts. They are characterized by a violent deformation with the continuous creation of new surfaces. Undoubtedly, when inhomogeneous media are encountered these processes become increasingly interesting. Ergo, this final chapter is devoted to the computational simulation of hypervelocity impacts with the developed fully compressible multiphase SPH algorithm.

6.1 Fully compressible multiphase SPH for hypervelocity impacts

The fully compressible multiphase scheme is based on the equations for ideal media of the adaptive number-smoothed approach, from Equation 4.17. In total, the scheme writes:

$$\frac{\mathrm{d}\tilde{\rho}_i}{\mathrm{d}t} = \frac{m_i}{\omega_i} \sum_j \Big(v_{\alpha,i} - v_{\alpha,j} \Big) \partial_\alpha W_{ij}(h_i) + \frac{\mathrm{d}\tilde{\rho}_i}{\mathrm{d}t}\Big|_{\mathrm{diss}}, \tag{6.1}$$

$$\frac{\mathrm{d}v_{\alpha,i}}{\mathrm{d}t} = -\frac{1}{m_i} \sum_j \left(\frac{m_i^2\, P_i}{\omega_i\, \tilde{\rho}_i^2}\, \partial_\alpha W_{ij}(h_i) + \frac{m_j^2\, P_j}{\omega_j\, \tilde{\rho}_j^2}\, \partial_\alpha W_{ij}(h_j) \right) + \frac{\mathrm{d}\tilde{v}_{\alpha,i}}{\mathrm{d}t}\Big|_{\mathrm{diss}} + F_{\alpha,i}, \tag{6.2}$$

$$\frac{\mathrm{d}e_i}{\mathrm{d}t} = \frac{P_i}{\tilde{\rho}_i^2} \frac{\mathrm{d}\tilde{\rho}_i}{\mathrm{d}t} + \frac{\mathrm{d}e_i}{\mathrm{d}t}\Big|_{\mathrm{diss}} + Y_i, \tag{6.3}$$

with a preliminary run over the j particles being necessary at every timestep to calculate the terms:

$$\omega_i = 1 - m_i \sum_j \frac{\partial W_{ij}(h_i)}{\partial h_i} \frac{\partial h_i}{\partial \tilde{\rho}_i}, \quad h_i = \eta \left(\frac{m_i}{\tilde{\rho}_i} \right)^{1/d}, \tag{6.4}$$

which account for the adaptivity of the scheme. Note that $P_i = P(\tilde{\rho}_i, e_i)$ and by $F_{\alpha,i}$ we denote the effects of the deviatoric stresses to the acceleration, while by R_i their contribution to the evolution of internal energy. According to Chapter 5, there is a unique description for them, no matter which scheme is used for the evaluation of density. In case of ideal media, modeled as $e = e(\tilde{\rho}, P(\tilde{\rho}))$, they identify as $F_{\alpha,i} = 0$ and $Y_i = 0$. For media with deviatoric response the discretized equations in updated Lagrangian description are (see Section 3.5.1):

$$F_{\alpha,i} = \frac{1}{\tilde{\rho}_i} \sum_j \left(\tau_{\alpha\beta,i}\, \partial_\beta W_{ij}(h_i) + \tau_{\alpha\beta,j}\, \partial_\beta W_{ij}(h_j) \right) \frac{m_j}{\tilde{\rho}_j}, \tag{6.5}$$

$$Y_i = -\frac{\tau_{\alpha\beta,i}}{\tilde{\rho}_i} \sum_j \Big(v_{\alpha,i} - v_{\alpha,j} \Big) \partial_\beta W_{ij}(h_i) \frac{m_j}{\tilde{\rho}_j}. \tag{6.6}$$

For their calculation, the *Jaumann stress rate* is employed, with its estimate provided [Libersky et al., 1993] by:

$$\frac{\mathrm{d}\tau_{\alpha\beta,i}}{\mathrm{d}t} = \tau_{\alpha\gamma,i} \frac{\mathrm{d}\varrho_{\beta\gamma,i}}{\mathrm{d}t} + \tau_{\gamma\beta,i} \frac{\mathrm{d}\varrho_{\alpha\gamma,i}}{\mathrm{d}t} + G_i \Big(\frac{\mathrm{d}\varepsilon_{\alpha\beta,i}}{\mathrm{d}t} - \frac{1}{d} \frac{\mathrm{d}\varepsilon_{\gamma\gamma,i}}{\mathrm{d}t} \delta_{\alpha\beta} \Big). \tag{6.7}$$

In order to calculate the latter, the strain and rotation rates, respectively:

$$\frac{\mathrm{d}\varepsilon_{\alpha\beta,i}}{\mathrm{d}t} = \frac{1}{2} \Big(\partial_\beta \tilde{v}_{\alpha,i} + \partial_\alpha \tilde{v}_{\beta,i} \Big), \quad \frac{\mathrm{d}\varrho_{\alpha\beta,i}}{\mathrm{d}t} = \frac{1}{2} \Big(\partial_\beta \tilde{v}_{\alpha,i} - \partial_\alpha \tilde{v}_{\beta,i} \Big), \tag{6.8}$$

are recovered by the discrete smooth estimates of the velocity's spatial derivatives:

$$\partial_\alpha \tilde{v}_{\beta,i} = \sum_j \Big(v_{\beta,i} - v_{\beta,j} \Big) \partial_\alpha W_{ij}(h_i) \frac{m_j}{\tilde{\rho}_j}. \tag{6.9}$$

The Mie-Grüneisen equation of state (also discussed in Section 1.1.3), with the parameters Γ and ξ, is used for the prediction of pressure:

$$P_i = \Big(1 - \frac{1}{2} \Gamma_i\, \upsilon_i \Big)\, P_{H,i} + \Gamma_i\, \tilde{\rho}_i\, e_i, \tag{6.10}$$

defined from the Hugoniot state:

$$P_{H,i} = \begin{cases} A_i \upsilon_i + B_i \upsilon_i^2 + C_i \upsilon_i^3, & \upsilon_i > 0, \\ A_i \upsilon_i, & \upsilon_i \leq 0, \end{cases} \tag{6.11}$$

where the compression is:

$$\upsilon_i = \tilde{\rho}_i / \rho_{0,i} - 1, \tag{6.12}$$

and the material constants are:

$$A_i = \rho_{0,i}\, c_{0,i}^2, \quad B_i = A_i[1 + 2(\xi_i - 1)], \quad C_i = A_i[2(\xi_i - 1) + 3(\xi_i - 1)^2]. \tag{6.13}$$

The Von Mises yield criterion for material strength is:

$$\tau^*_{\alpha\beta,i} = \tau_{\alpha\beta,i} \frac{\sigma_{Y,i}}{3\tau_{\alpha\beta,i}\tau_{\alpha\beta,i}}, \tag{6.14}$$

with σ_Y the yield strength and G the shear modulus. These and all other necessary parameters for the materials used in this study, appear in Table 6.5, collected from Hasegawat and Young [1980]; Hiermaier et al. [1997]; Libersky et al. [1993]; Marsh [1980]; Millett et al. [2005]; Shintate and Sekine [2004].

In all later tests, the Gaussian kernel (2.6) is employed, with $\eta = 1.2$, truncated at $3h$. Following the discussion of Chapter 2, possible advantages of using the Wendland kernel (2.10) were examined. No advantage was experienced. Time marching is performed using the leapfrog algorithm of Section 4.3, using a constant time step, which is checked against the time-stepping criterion.

The reasons of choosing the specific scheme, sum up to the following: 1) the introduced adaptivity is with respect to the local number density; certain findings of Chapter 5 offer evidence that disrespecting it, may bring in inaccuracies; 2) the inclusion of the ω-terms, accounting for the adaptivity, allows for exact conservation, which is tantamount to the long-term stability of the system; 3) the use of particles of unequal masses allows for exact modeling in terms of geometric restrictions, as it is argued in Section 4.4; 4) artificial dissipation terms are endowed with the structure of Riemann-solvers (see Section 4.2) and are applied to all variables, so that an over-increased viscosity parameter [Hiermaier et al., 1997; Shintate and Sekine, 2004] becomes unnecessary; the latter may create over-smoothed solutions.

A comment about some of our modeling choices is in place. Regarding the equation of state, the Tillotson equation of state could have been used (see Section 1.1.3). However, its parameters for materials other than Aℓ are scarce, if existing at all in the literature. Similarly, data for advanced strength models, such as the Johnson-Cook, are scarce when materials other than Aluminum are studied, while it is not always possible to include them consistently in the variational framework. For this reason, and as a primary approach, we choose to keep the models simple.

The three-dimensional experiments, which follow, are simulated in a two-dimensional geometry. Since in all experiments the projectile is a sphere and the target a plate, we are actually simulating the impact configuration on an equatorial plane of the sphere, parallel to the vector of the impact velocity. There are good reasons for this choice. First, the computational effort to achieve fine details in 3D (both due to the higher total number of particles and the interactions of each particle with its neighbors) is prohibitive for a code which can be run on a standard personal computer. Second, the validation of the experimental data is performed with shadowgraphs depicting the projections of the three-dimensional configurations onto the observation two-dimensional frame. On this frame, the maxima of the debris cloud's length and width

are considered. They occur on exactly the plane simulated, that is the equatorial plane of the sphere, parallel to the vector of the impact velocity.

6.2 Experimental validation

The combined experimental and computational study of Hiermaier et al. [1997] serves as a validation test. Three scenarios are examined therein and they refer to the normal impacts of an Aluminum-2024 (Aℓ2) sphere of radius $R = 5\,\text{mm}$ into: 1) an Aluminum-2024 plate of thickness 4 mm, at velocity $U = 6.18\,\text{km/s}$; 2) a copper (Cu) plate of thickness 15 mm, at velocity $U = 5.75\,\text{km/s}$; and 3) a lead (Pb) plate 15 mm thick, at velocity $U = 6.85\,\text{km/s}$. The relevant data appear in Tables 6.1 and 6.2.

The left subplots of Figure 6.1, show the initial problem setups for the cases examined. In all of them, the distance of the projectile to the plate is such that it is covered by the projectile in 1 μs.

	ρ_0 10^3 Kg/m^3	c_0 Km/s	ξ	Γ	G GPa	σ_Y GPa
Aℓ1	2.710	5.300	1.500	1.7	25.0	0.550
Aℓ2	2.785	5.330	1.338	2.0	27.1	0.265
Pb	11.360	2.030	1.470	2.6	8.6	0.090
Cu	8.930	3.900	1.500	2.0	46.0	0.045
Epoxy	2.280	2.930	1.630	1.0	0.6	0.050
Homogenized	2.659	4.730	1.411	1.75	20.5	0.238

TABLE 6.1: Material data.

Materials	Sphere radius mm	Plate thickness mm	Impact velocity km/s
Aℓ2 - Aℓ2	5	4	6.18
Aℓ2 - Cu	5	15	5.75
Aℓ2 - Pb	5	15	6.85

TABLE 6.2: Geometrical and initial data.

	Experiment	Computation	Present Study
Aℓ2 - Aℓ2	1.39	1.11	1.36
Aℓ2 - Cu	1.39	1.33	1.49
Aℓ2 - Pb	1.56	1.16	1.48

TABLE 6.3: Length-to-width of the debris cloud 20 μs after impact. Experiment and computation from Hiermaier et al. [1997] compared to the results of the present study.

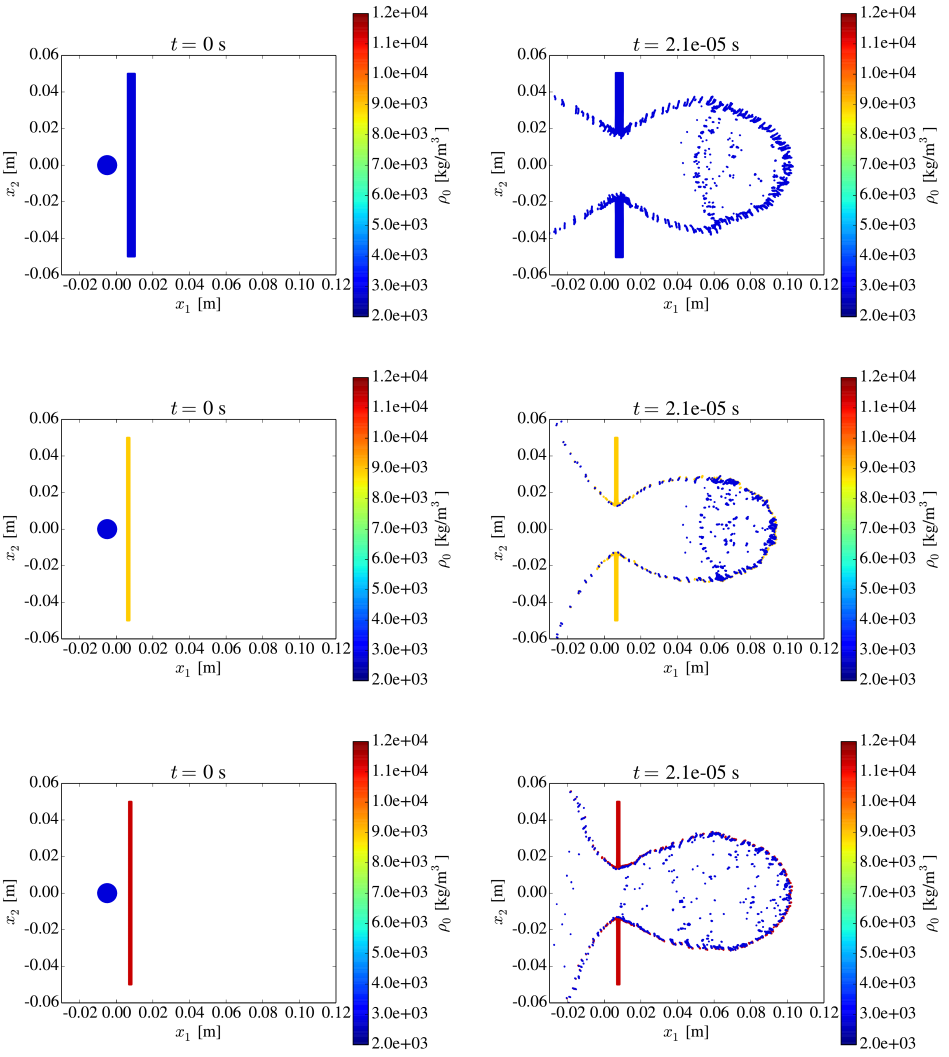

FIGURE 6.1: The hypervelocity impacts Aℓ2-Aℓ2, Aℓ2-Cu and Aℓ2-Pb, from top to bottom, initially and 20 μs after impact.

	Experiment mm	Computation mm	Present Study mm
Aℓ2 - Aℓ2	27.5 – 34.5	35	24 – 34
Aℓ2 - Cu	21.2	23	27
Aℓ2 - Pb	26.0	30	27

TABLE 6.4: Crater diameter after impact. Experiment and computation from Hiermaier et al. [1997] compared to the results of the present study. Range of values refer to crater diameters including and excluding crater lips.

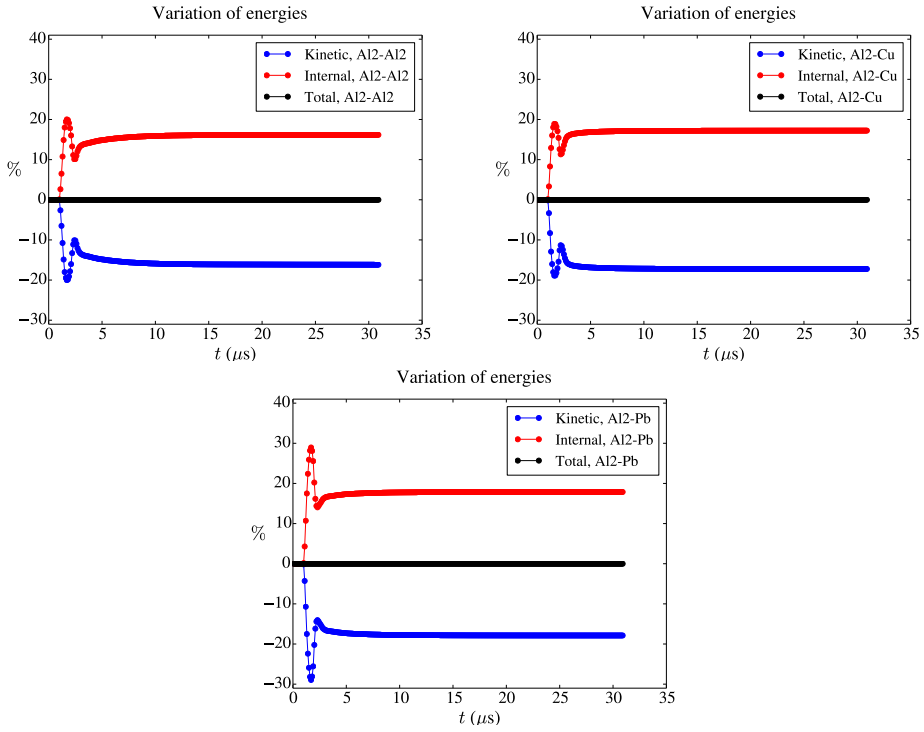

FIGURE 6.2: Energy variations for the Al-Al, Al-Cu and Al-Pb impacts.

The discretization of the projectile and the plates correspond to 20 particles per mm, so that 30 particles appear through the thickness of the Cu and Pb plates in a hexagonal formation and $N = 25184$ is the total number of particles for the related impacts. The same through-the-thickness resolution produces $N = 54059$ number of particles in the Aℓ2 plate of the corresponding impact. Regarding the chosen timestep, $\Delta t = 5 \times 10^{-5}$ μs is well above the corresponding numerical criterion as used by Hiermaier et al. [1997]; Libersky et al. [1993] and discussed in Section 4.3. The simulation is run until $t = 31$ μs. Note that there is no explicit reference to a stopping criterion in any of the relevant studies cited [Hiermaier et al., 1997; Libersky et al., 1993; Liu et al., 2013; Shintate and Sekine, 2004]. In any case, we expect that the assumption

of ideal conditions, which the employed set of equations describes, fails as time passes. The reason is that dissipative effects become effective later than the effects of compressibility.

In Figure 6.1, the right subplots show the material distribution of all cases 20 μs after impact, when the ratio of length-to-width of the debris clouds are recorded for validation by Hiermaier et al. [1997]. Table 6.3 refers to the values of the debris clouds developed $t = 20\,\mu$s post impact. For the impact with the largest density ratio, Aℓ2-Pb, the latter value is found to be 1.48, which is in good agreement with the experimentally observed 1.56, compared to the computational value 1.16 of Hiermaier et al. [1997]. Regarding the resulting opening of the plate in Table 6.4, it is 27 mm, with the experimental value being 26 mm, and the result of Hiermaier et al. [1997] being 30 mm. A similar enhancement in the computational results is observed for the case of the Aℓ2-Aℓ2 impact, with a much better prediction of the length-to width ratio of the debris cloud (Table 6.3). Regarding the Aℓ2-Cu impact, results are not as satisfactory as in the previous cases. The reason for this is that in Hiermaier et al. [1997] the specific type of Cu used is not mentioned, neither can it be deduced. Therefore, the parameters chosen for the present study for Cu, probably vary from the actual ones, thus leading to inaccurate results.

Finally, the energy losses of the scheme is in all cases smaller than 0.003% of its initial value, in contrast to the maximal energy losses of 5.5% mentioned in Hiermaier et al. [1997] for the same impacts. In Figure 6.2, the variations of kinetic, internal and total energy are presented.

6.3 Deformation patterns in laminated materials

The goal of the following investigation focuses on the opening pattern occurring after hypervelocity impacts into laminated materials. Additionally, it is highlighted that a detailed description of the deformation is possible when the laminate is modeled with piecewise constant properties in contrast to using a homogenized model.

For the purpose of experimental investigation, a laminated plate was constructed at the facilities of the Fibre Metal Laminates Centre of Competence (FMLC), TU Delft, The Netherlands. Three Aluminum 2024 plates, with surface dimensions 40 mm$\times$40 mm and of thickness 0.5 mm each, were glued together using the Stycast 2850 alumina-filled epoxy resin. The epoxy comes in two ingredients, which upon mixing in appropriate doses, were applied to the Aluminum 2024 plates. The laminate was cured in an oven. The resulting thickness of each epoxy resin was 0.25 mm giving a total thickness of 2 mm to the laminate.

The experimental hypervelocity impact took place at the facilities of the Fraunhofer Ernst Mach Institute (EMI), Freiburg, Germany on November 26th 2014, with EMI shot id: SLGG-5660 and Project Title: Impact tests for TU Eindhoven. An Aluminum series 1000 projectile was accelerated using the lab's light-gas gun (Figure 6.3) at the speed of $U = 4.28$ km/s in an almost pressure-less (100 mbar) chamber, where it

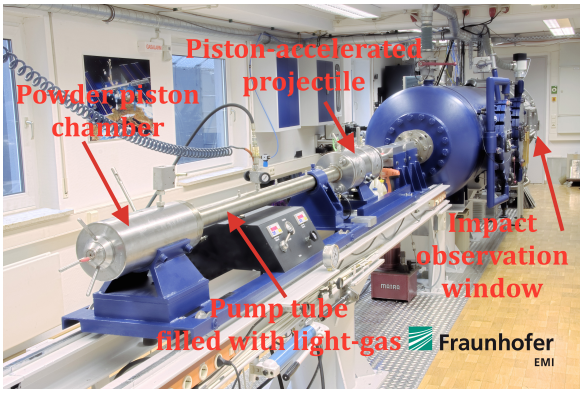

FIGURE 6.3: The two-stage light-gas gun at the hypervelocity impact facilities of the Fraunhofer EMI, Freiburg, Germany. For the related technology see Ch.1. and Ch.2, Chhabildas et al. [2005].

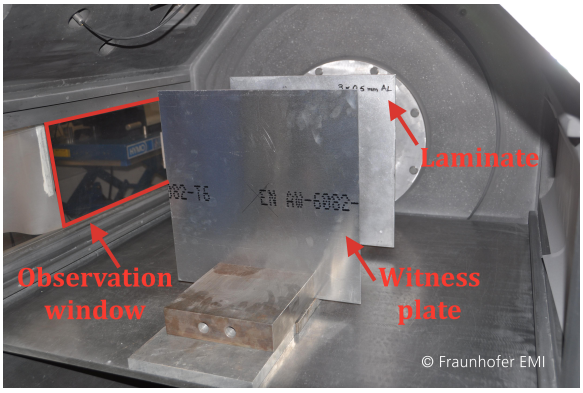

FIGURE 6.4: The initial setup of the plate in the vacuum chamber of the gas gun. The plate noted "3x0.5mm AL" is the laminate and the other plate serves as witness plate. The direction of the accelerated projectile is from the Laminate to the witness plate, with the latter receiving the impact-produced debris.

FIGURE 6.5: Front side of the Laminate after the hypervelocity impact experiment. The opening of the middle layer is 10 mm and the inner diameter of the petal-like opening 23 –25 mm. For the latter opening, a slightly larger value (27 –28 mm) is observed on the rear side.

impacted the above-mentioned laminate. The experiment was recorded by an optical camera until time 5000 μs, using a temporal resolution of 20 μs. Figure 6.4 shows the initial setup in the chamber and in Figure 6.5 the final opening on the front side of the Laminate is exhibited.

In Figure 6.6, selected camera pictures depict the evolution of the process. Starting from left to right and going top-down, the first image shows the exact moment when the projectile hits the target plate. At $t = 20\,\mu$s, a light emission appears, which characterizes hypervelocity impacts. Additionally, the two major effects of the hypervelocity impact appear: the developing debris cloud and the opening of the laminate at the impact site. In the next picture ($t = 40\,\mu$s), the debris cloud expands further, while the plate has deformed significantly and in the later image, at t =60 μs, most of the deformation has already occurred, since its differences from the previous picture are indistinguishable. The following two pictures are one timescale later, at t =200 μs and t =300 μs, when the debris cloud finally arrives on the witness plate. A secondary effect clearly appears at t =500 μs, and concerns epoxy ejecta detaching from the target and traveling in the direction opposite to the impact velocity. Eventually, the last picture refers to $t = 5000\,\mu$s, that is one timescale later than the previous picture, and shows that the process has terminated.

The camera pictures and the *post mortem* analysis of the laminate, as witnessed in Figure 6.5, show that the projectile perforated the laminate and the diameter of the opening was 10 mm. Interestingly, the deformation pattern around the impact site is characterized by a *petaling* pattern, exactly because it resembles the opening of a flower's corolla.

This opening pattern poses a challenge for any attempted computational solution of the previous problem. Inevitably, models which neglect the piecewise properties of the laminate by assuming a homogenized laminate model (of uniform properties) are doomed to miss this deformation pattern. To this end, and also in order to pronounce the necessity for multiphase modeling, we test how the results of the developed multiphase SPH scheme qualitatively compare to the experiment.

Three different numerical experiments are conducted. Each of them refers to a plate of thickness 2 mm, which is impacted by an Aluminum-1000 (Aℓ1) projectile of radius $R = 2.5$ mm, at the speed of $U = 4.28$ km/s. The material parameters of the projectile remain the same for all three experiments, while those of the plate are different in every experiment. The first plate is monolithic Aluminum-2024 (Aℓ2). The second is the layered plate of the experiment. The third plate is created as the Homogenized version of the laminated plate.

Due to the lack of data from homogenization models, and since this is a numerical experiment aiming at revealing qualitative features, the homogenization is merely an averaging of the properties over the volume of the plate's constituents. This means that all the properties of the Homogenized model-plate (see Table 6.5) are taken as $\pi_{Hmg} = 0.75\pi_{A\ell 2} + 0.25\pi_{Epx}$, depicting the volume ratio of the plate's

FIGURE 6.6: Evolution of the experimental hypervelocity impact into the Laminate, at $t = 0, 20, 40, 60, 200, 300, 500, 5000\mu$s, after impact. The temporal resolution of the camera is 20 μs.

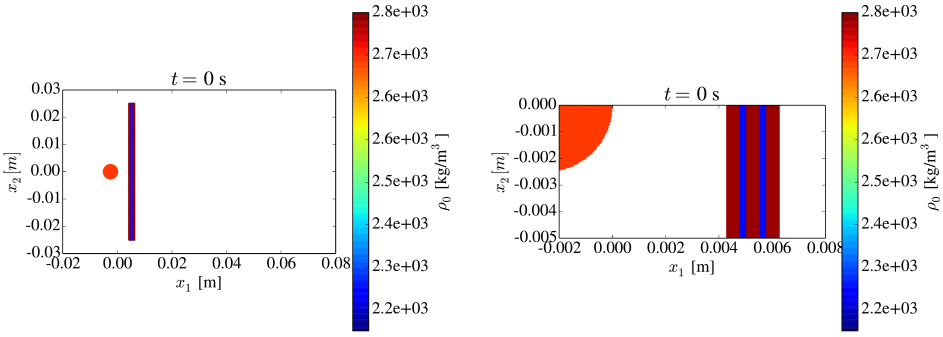

FIGURE 6.7: Initial discretization of the Laminate.

constituents[1]. Note that in this way, the total mass of the plate remains the same, only it is distributed uniformly over the plate. It is certainly not an accurate modeling choice, nevertheless it depicts the concept of homogenization and it is relevant for the extraction of qualitative conclusions *vis-à-vis* the purely discontinuous laminate model. It has the advantage that in the global scale, features such as momentum transfer and inertia, remain the same.

Figure 6.7 depicts the initial configuration and a detail of the discretization, corresponding to 20 particles per mm, resulting to 40 particles through the thickness of the plate in a rectangular formation and $N = 54509$ particles in total. Each Epoxy layer has 5 particles through the thickness, a number which is in good balance between acceptable results and the computational efficiency of obtaining results in less than a day on a standard desktop computer. The timestep is $\Delta t = 5 \times 10^{-5}$ μs, bounded by the same criterion used by Libersky et al. [1993]. Similarly to the validation test case, and according to the conservative nature of the equations, the energy losses are below 0.005% of the initial kinetc energy of the projectile. The projectile impacts the target having traveled for 1 μs from its initial position.

In all cases, the impact generates two shock waves which travel away from the projectile/target interface, moving in opposite directions; one through the projectile and the other through the target. The latter wave compresses the target, in the way depicted in the left plots of Figure 6.8, for the monolithic, the laminate the homogenized plate from top to bottom, respectively.

In the right plots of Figure 6.8, the material distribution of each plate is shown 10 μs after impact, when the projectile has perforated the target plates. No major differences are observed among the plates at that time. Nonetheless, certain differences start becoming apparent at later times. The material configurations in Figure 6.9 correspond to time 20 μs after impact. In the left plots, showing the local material configuration, for the plates with uniform initial density, a sharp opening through their thickness appears. Conversely, in the Laminate, the outer Aℓ2 layers start detaching from the middle one. This characteristic is observed in Figure 6.5, which shows the opening of

[1]Where, *Hmg* stands for Homogenized and *Epx* for Epoxy.

the specimen, following the corresponding experimental hypervelocity impact. The computational result presented here suggests that this detachment occurs within the Epoxy layers. This deformation pattern is the result of the different wave propagation mechanisms in the laminated plate as compared to the other plates.

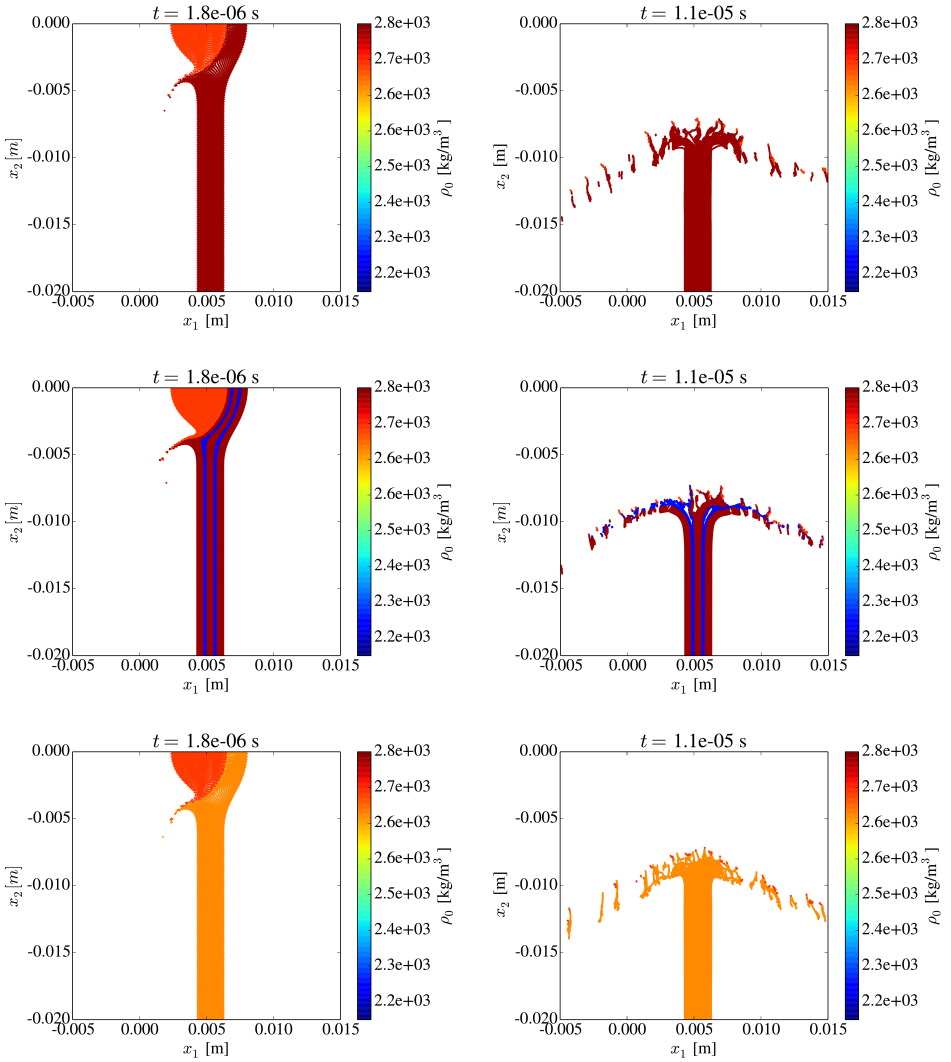

FIGURE 6.8: Monolithic, Laminate and Homogenized models, 0.8 μs and 10 μs after impact.

In the plates with uniform initial density, shocks arrive undisturbed to their rear sides, while in the Laminate, successive reflections-transmissions of waves occur. The mechanism is the following. The impact-induced shock wave starts moving through the first Aℓ2 layer and compresses it. When the shock wave arrives on the first material interface (Aℓ2/Epx), it is partly transmitted through the interface to the adjacent Epoxy layer and partly reflected back to the first Aℓ2 layer. Similar

reflections-transmissions occur inside all layers of the target. At the same time, apart from the wave propagation through the thickness of the targets, the impact-induced shocks propagate also in the transverse direction. Apparently, for the laminated plate, the waves propagate at different speeds within each material. Thus, a shearing motion occurs between layers of different materials. The different propagation mechanisms are illustrated in Figure 6.10, which shows the shock wave formation in terms of density for the laminate (*left*) and the homogenized plate (*right*). With respect to the computational result, notice that no instabilities appear on the interfaces in the profile of these two magnitudes. Additionally, the density profile is discontinuous in the case of the laminate, as expected by the Riemann-like structure of the problem.

Therefore, the characteristic deformation pattern of the laminate can be attributed to the synergy of these two propagation mechanisms: the successive reflections-transmissions and the shearing motion. It is questionable which mechanism prevails; they rather work complementary to each other.

In any case, it should be mentioned that the computational result is susceptible to numerical fracture, especially in regions of the domain which undergo large bending. A possible way to fix this is to use an adaptive method; one that splits existing particles and populates these regions with more particles. A splitting technique has been suggested by Shintate and Sekine [2004] in the context of the traditional SPH scheme for hypervelocity impacts. Although simple in concept, such techniques typically lead to momentum and energy injection in the system. Additionally, Vacondio et al. [2012] shows that such schemes cannot be derived in a straightforward manner. An extension of the present research would aim at examining this aspect.

The right plots of Figure 6.9 depict the material configurations 20 μs after impact, for the monolithic plate, the laminated plate and the homogenized plate, respectively from top to bottom. In all cases, it may be seen that the rarefaction wave decelerated the projectile material (orange-colored particles), which is lagging behind with respect to the target material. Moreover, it seems that this feature is somehow pronounced for the laminated plate, an effect which can be attributed to the multiple rarefaction waves occurring due to the discontinuous density profile of the plate. Safer conclusions can be drawn by measuring the size of the debris cloud's length, width and length-to-width ratio, 20 μs after impact. The following recordings appear for the monolithic plate: length 65 mm, width 45 mm and ratio 1.44; for the laminate: length 68 mm, width 46 mm and ratio 1.48; for the homogenized plate: length 66 mm, width 48 mm and ratio 1.38. One may expect that a lower length-to-width ratio implies that the debris cloud is dispersed in a wider region and the concentration of momentum per unit area on the tip of the cloud is smaller.

In the numerical experiments under discussion, the openings produced (Figure 6.11) are almost four times the diameter of the projectile and in specific: 18.2 mm to 18.3 mm for the monolithic plate, 19.4 mm for the laminate and 17.6 mm for the homogenized plate.

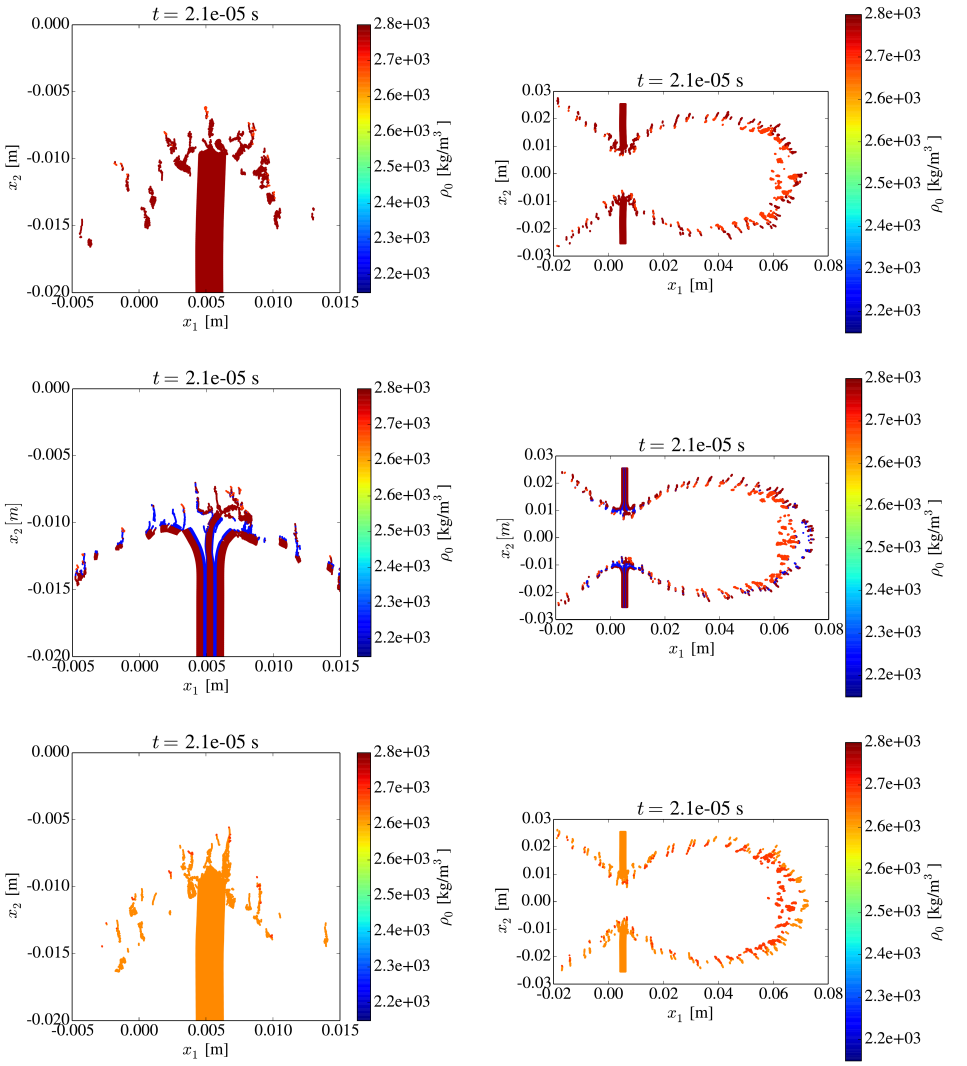

FIGURE 6.9: Monolithic, Laminate and Homogenized models, 20 μs after impact, local (*left*) and global (*right*) material configurations.

As already discussed, the computational Laminate model is able to capture correctly the petaling opening pattern, observed in the experimental result of Figure 6.5. A direct quantitative comparison is also possible, regarding the sizes of the openings. The Laminate model overestimates the experimentally observed value of 10 mm for the diameter of the opening in the middle Aluminum layer. In fact, the computational model seems to provide an opening with size closer to the inner diameter of the petal-like opening in the experiment (23 –25 mm).

The reasons for this quantitative deviation point towards ways to improve the com-

	Debris cloud	Crater diameter mm
Monolithic	1.44	18.3
Laminate	1.48	19.4
Homogenized	1.38	17.6

TABLE 6.5: Length-to-depth of the debris cloud 20 μs after impact and crater diameter

putational model. The following seem the most appropriate, in order of significance: 1) including a bond strength, since now SPH is left to do this inherently, by allowing particles of Aluminum to "see" particles of Epoxy; 2) treating numerical fracture, an issue also discussed above; 3) advanced modeling of material strength, in a way that respects the multiphase scheme; 4) improving material data, though the ones used now are already on the limits of what engineers can provide; 5) performing 3D computations with fine discretization.

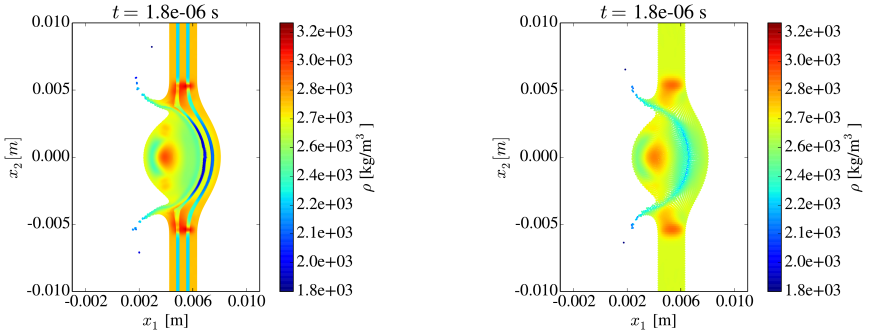

FIGURE 6.10: Density profiles for the Laminate and the Homogenized models, 0.8 μs after impact.

Finally, the variation of energies for these experiments appear in Figure 6.11 and show that the assumption for invariant total energy is correct for the time period studied.

6.4 Discussion

The present study reports some developments in the simulation of hypervelocity impacts into laminated plates with the SPH method. For detailed deformation patterns, each layer of a laminate should be modeled explicitly rather than using a homogenized model for the whole plate. To this end, a multiphase fully compressible SPH solver is extended such that it accommodates full stress models. It is found to provide good results when validated against the classical hypervelocity impact experiments of Hiermaier et al. [1997], and especially to the impact between two materials of high density ratio (Aℓ2-Pb).

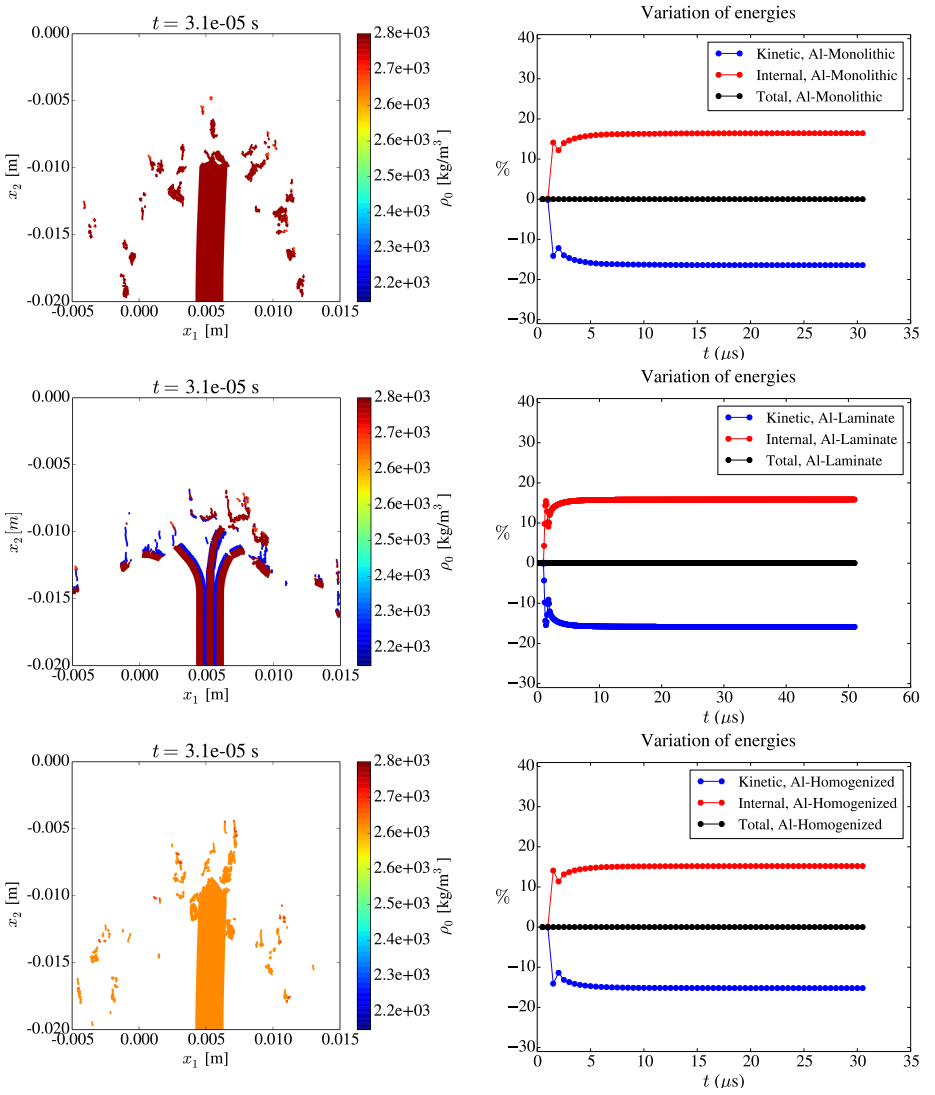

FIGURE 6.11: Monolithic, Laminate and Homogenized models, 30 μs after impact (*left plots* with magnitudes in SI units) and energy variations (*right plots*).

In order to exhibit the differences in the deformation patterns of laminates under hypervelocity impacts, the study compares the impact of a projectile at the same velocity against three plates of the same size; a monolithic Aℓ2, an Aℓ2-Epoxy laminate and a homogenized version of the latter. It is found that the differences in the sizes of the debris clouds produced after the hypervelocity impact of each plate are not critical. Conversely, there are profound differences in the deformation pattern of laminates, when compared to the deformation patterns of the plates with uniform initial density.

As a general remark, the detailed description of the deformation of laminates under

hypervelocity impacts is possible and multiphase SPH schemes are capable for this task. Furthermore, it is probably possible to achieve more accurate results using an adaptive strategy —where the number of particles increases in critical regions of the domain— so that numerical fracture is limited.

Epitome

The research elaborated in the present thesis arrives to certain conclusions and provides guidelines for further studies.

Starting from the first topic presented, the framework of measure-valued evolutions enables us to consistently analyze the smoothing operation in SPH and more importantly, the transition from the continuous system to the discrete one. Heuristically, it is shown how the smoothing length relates to the local number of particles, thus making number density a key quantity in SPH. Additionally, the coupled relation of the smoothing length to the smoothing function is tackled. This issue is discussed in the literature, the present study extends it in the following way. For the discrete system, given a smoothing length and a smoothing function, there exists a formula which calculates the necessary smoothing length, such that results of the same resolution are obtained with another smoothing function. The applicability of this formula, in practical SPH computations, is still to be investigated.

From a mathematical point of view it is shown that SPH schemes arrive from the following triptych: 1) the smoothed density of one of the basic measures, probability, counting or Lebesgue measure; 2) the principle of least action for continuous media; 3) a thermodynamic relation describing the properties of the medium under study. Note that the action of the continuum is minimized rather than the one of the discrete system. This formulation allows to define SPH as the computational method which solves the equations of continuum mechanics for a specific type of medium: *the smoothed medium*. Depending on the chosen measure, three different smoothings appear, which result to three different schemes, each with certain merits and weaknesses. The latter are examined with a series of tests in the last two chapters.

A simple convergence analysis, exhibits the conditions under which the smoothed medium converges to the classic medium of continuum mechanics. It corresponds

to a static case, however it provides insight into how the number density influences convergence.

For media which respond with a full stress tensor, the developed framework suggests that either smoothed estimates of distortions need to be constructed or smoothed estimates of the variations of the distortions. These two different options lead to SPH in total Lagrangian description and SPH in updated Lagrangian description, respectively. The choice is made based on which description suits the problem better, similarly to classical continuum mechanics. An open question is whether these two approaches can be coupled.

The form of the gradient operators in the conservation equations of the smoothed medium are bound by the variational structure of the system. In specific, they arrive as variations of the corresponding smoothed densities with respect to a change in particle trajectories, rather than being constructed as smooth approximations to the gradients of these densities. As opposed to this, the Laplacian operator of velocity —responsible for dissipative effects— is not due to variations, and thus its form can be freely chosen based on the required accuracy. Regarding dissipative media exhibiting plasticity, further understanding is required on how derivatives are constructed, especially for problems in the updated Lagrangian description.

Fully compressible SPH schemes require an adaptive smoothing length. It is conjectured that only those which respect the coupling of the smoothing length to the local number density are (the most) adequate to resolve shock propagation. Indeed, the series of numerical tests performed in the present study show the validity of this claim, in one and two spatial dimensions. This is achieved for schemes coming from the smoothing of number density and for multiphase problems, it is combined with two types of discretization: using equal particle masses per phase or equal initial particle volumes, also corresponding to uniform initial number density. In specific, the former seem to perform better around contact discontinuities and in fact, in this case the scheme becomes equivalent to the scheme coming from the smoothing of the mass density. Nonetheless, they suffer from two restrictions: a geometrical one and a computational one. Regarding the first, since for schemes with equal particle masses the ratio of the phases' initial densities should equal the ratio of the initial volumes in each phase, this cannot lead to generic particle-filling algorithms in complicated or bounded geometries. As for the second restriction, since the resolution is dictated by the phase with the highest density, large density ratios become tedious. In the present thesis, the alternative of constructing equal initial volumes (hence uniform initial number density), with the particle masses of each phase reflecting the ratio of initial densities, is shown to work remarkably well.

In the developed algorithm, artificial dissipation terms are used, in order to suppress oscillations rising around shocks and perturbed contact discontinuities. A new mass-flux term is employed and tested for delivering sharp density contact discontinuities and flat pressure profiles across them. Towards the former, the term works effectively, even for high density ratios. An open question is whether it can become more advanced, so that it treats the latter for high density and speed-of-sound ratios. To this end, comparisons with approximate Riemann-solvers are necessary.

The two last topics are part of a broader question: are very high-density ratios a bottleneck for SPH in multiphase fully compressible processes? And if they are, is it merely for reasons of computational efficiency? Tests in two spatial dimensions seem to imply that in order to answer this question, consistent approaches to introduce particle adaptivity —particle splitting and merging— are necessary.

Regarding hypervelocity impacts and the deformation patterns of laminated materials, qualitative comparisons become available, partially because of the developed algorithm's ability to describe shock description correctly. For quantitative comparisons, specific data for the involved materials are necessary, which are scarce in the literature. Additionally, it becomes obvious that two ingredients are missing from the current treatment of hypervelocity impacts: 1) some form of particle adaptivity in order to deliver finer results and possibly counteract instabilities and 2) correct application of free boundary conditions to reduce the computational cost, such that it becomes possible to go further in time. Both strategies exist in the literature, however they are mostly performed in an *ad hoc* manner. New studies should focus on making them consistent with the standard SPH framework.

Last but certainly not least, the *Golden Fleece*[2] of SPH: a proof of its convergence in the course of time, as $N \to \infty$ and $h \to 0$ simultaneously. In the present thesis, numerical evidence of convergence, under the aforementioned conditions, is exhibited with two practical applications. However, a complete proof is elusive in the literature which typically considers each condition separately. The heuristics of this work suggests that *number density* is probably the key to this longstanding problem.

[2] *The fleece of a golden ram, guarded by an unsleeping dragon, and sought and won by Jason with the help of Medea*, Oxford Dictionary of English (https://en.oxforddictionaries.com), from the poem *Argonautica* by Appolonios Rhodios [3rd century BC].

Bibliography

O. Agertz, B. Moore, J. Stadel, D. Potter, F. Miniati, J. Read, L. Mayer, A. Gawryszczak, A. Kravtsov, A. Nordlund, F. Pearce, V. Quilis, D. Rudd, V. Springel, J. Stone, E. Tasker, R. Teyssier, J. Wadsley, and R. Walder. Fundamental differences between SPH and grid methods. *Mon. Not. R. Astron. Soc*, 380(963–978), 2007.

Appolonios Rhodios. *Argonautica*. 3rd century BC.

N. Aquelet, M. Souli, and L. Olovson. Euler Lagrange coupling with damping effects: Application to slamming problems. *Comp. Methods Appl. Mech. Engrg.*, 195:110–132, 2005.

J. Asay and G. Kerley. The response of materials to dynamic loading. *Int. J. Impact Eng.*, 5(1–4):69 – 99, 1987. Hypervelocity Impact Proceedings of the 1986 Symposium.

J. Asay and M. Shahinpoor, editors. *High-Pressure Shock Compression of Solids*. Springer-Verlag, 1993.

V. Berdichevsky. *Variational Principles of Continuum Mechanics - I. Fundamentals*. Springer-Verlag, Berlin-Heidelberg, 1st edition, 2009.

J. Bonet and S. Kulasegaram. Correction and stabilization of Smooth Particle Hydrodynamics methods with applications in metal forming simulations. *Int. J. Numer. Methods Engng.*, 47(1189–1214), 2000.

J. Bonet and T.-S. Lok. Variational and momentum preservation aspects of Smooth Particle Hydrodynamic formulations. *Comp. Methods Appl. Mech. Engrg.*, 180(1–2): 97 – 115, 1999.

J. Bonet and M. Rodriguez-Paz. Hamiltonian formulation of the variable-h SPH equations. *J. Comput. Phys.*, 209:541–558, 2005.

S. Borve and D. Price. Hydrodynamical instabilities in compressible fluids using SPH. *Proceedings of the 4th SPHERIC workshop, May 26-29, Hannover*, 2009.

A. Brundage. Implementation of Tillotson equation of state for hypervelocity impact of metals, geologic materials, and liquids. *Procedia Eng.*, 58:461–470, 2013.

S. Cheng. A Crash Course on the Lebesgue Integral and Measure Theory. online, April 2008.

L. Chhabildas, L. Davison, and Y. Horie, editors. *High-Pressure Shock Compression of Solids VIII: The Science and Technology of High-Velocity Impacts*. Springer, 2005.

A. Chorin. A numerical method for solving incompressible viscous flow problems. *J. Comput. Phys.*, 2:12–26, 1967.

E. Christiansen, J. Crews, J. Williamsen, J. Robinson, and A. Nolen. Enhanced meteoroid and orbital debris shielding. *Int. J. Impact Eng.*, 17(1–3):217 – 228, 1995.

R. Clegg, C. Hayhurst, J. Leahy, and M. Deutekom. Application of a coupled anisotropic material model to high velocity impact response of composite textile armour. In *18th International Symposium and Exhibition on Ballistics San Antonio*, 1999.

A. Colagrossi and M. Landrini. Numerical simulation of interfacial flows by smoothed particle hydrodynamics. *J. Comput. Phys.*, 191(2):448 – 475, 2003.

R. Courant and K. Friedrichs. *Supersonic Flow and Shock Waves*. Interscience Publishers, 1948.

S. Cummins and M. Rudman. An SPH projection method. *J. Comput. Phys.*, 152: 584–607, 1999.

L. Davison. *Fundamentals of Shock Wave Propagation in Solids*. Springer-Verlag, Berlin Heidelberg, 2008.

W. Dehnen and H. Aly. Improving convergence in smoothed particle hydrodynamics simulations without pairing instability. *Mon. Not. R. Astron. Soc*, 425(2):1068–1082, 2012.

S. Diehl, G. Rockefeller, C. Fryer, D. Riethmiller, and T. Statler. Generating optimal initial conditions for Smoothed Particle Hydrodynamics simulations. *Pub. Astronom. Soc. Australia*, 32:e048, 2015.

R. DiLisio, E. Grenier, and M. Pulvirenti. The convergence of the SPH method. *Comput. Math. Appl.*, 35:95–102, 1998.

G. Drolshagen. Impact effects from small size meteoroids and space debris. *Adv. Space. Res.*, 41(7):1123 – 1131, 2008.

C. Dyka and R. Ingel. An approach for tension instability in Smoothed Particle Hydrodynamics. *Comp. Struct.*, 57:573–580, 1995.

L. C. Evans. *Partial Differential Equations*. American Mathematical Society, 1st edition edition, 1998.

J. Evers, I. Zisis, B. van der Linden, and M. Duong. From continuum mechanics to SPH particle systems and back: Systematic derivation and convergence. *ZAMM (accepted - preprint:* arxiv.org/abs/1501.04512), 2015.

E. Fahrenthold and J. Koo. An improved hybrid particle-element method for hypervelocity impact simulations. *Int. J. Impact Eng.*, 26:169–178, 2001.

K. Friedrichs. The identity of weak and strong extensions of differential operators. *Trans. Am. Math. Soc.*, 55:132–151, 1944.

R. Gingold and J. Monaghan. Binary fission in damped rotating polytropes. *Mon. Not. R. Astron. Soc*, 184:481–499, 1978.

R. A. Gingold and J. Monaghan. Smoothed Particle Hydrodynamics: theory and application to non-spherical stars. *Mon. Not. R. Astron. Soc*, 181:375 – 389, 1977.

N. Grenier, M. Antuono, A. Colagrossi, D. L. Touzé, and B. Alessandrini. An hamiltonian interface SPH formulation for multi-fluid and free surface flows. *J. Comput. Phys.*, 228(22):8380 – 8393, 2009.

J. Haas and B. Sturtevant. Interaction of weak shock waves with cylindrical and spherical gas inhomogeneities. *J. Fluid Mech.*, 181:41–76, 1987.

M. Hasegawat and W. Young. Grüneisen parameters for simple metals. *J. Phys. F: Metal Phys.*, 10:225 – 234, 1980.

C. Hayhurst, C. Livingstone, R. Clegg, G. Fairlie, S. Hiermaier, and M. Lambert. Numerical simulation of hypervelocity impacts on aluminum and nextel/kevlar whipple shields. *Hypervelocity Shielding Workshop, 8-11 March 1998, Galveston, Texas*, 1998.

L. Hernquist. Some cautionary remarks about Smoothed Particle Hydrodynamics. *Astrophys. J.*, 404:717–722, 1993.

S. Hiermaier. *Structures Under Crash and Impact - Continuum Mechanics, Discretization and Experimental Characterization*. Springer Science+Business Media, LLC, New York, 1st edition, 2008.

S. Hiermaier and F. Schafer. Hypervelocity impact fragment clouds in high pressure gas numerical and experimental investigations. *Int. J. Impact Eng.*, 23:391–400, 1999.

S. Hiermaier, D. Könke, A. Stilp, and K. Thoma. Computational simulation of the hypervelocity impact of Al-spheres on thin plates of different materials. *Int. J. Impact Eng.*, 20:363 – 374, 1997.

P. Hopkins. A general class of Lagrangian Smoothed Particle Hydrodynamics methods and implications for fluid mixing problems. *Mon. Not. R. Astron. Soc*, 428: 2840–2856, 2013.

N. Hosono, T. Saitoh, and J. Makino. Density-independent Smoothed Particle Hydrodynamics for a non-ideal equation of state. *Publi. Astron. Soc. Japan*, 108, 2013.

X. Y. Hu and N. A. Adams. A multi-phase SPH method for macroscopic and mesoscopic flows. *J. Comput. Phys.*, 213(2):844–861, 2006.

S. Inutsuka. Reformulation of Smoothed Particle Hydrodynamics with Riemann solver. *J. Comput. Phys.*, 179(1):238 – 267, 2002.

G. Johnson. Artificial viscosity effects for SPH impact computations. *Int. J. Impact Eng.*, 18(5):477 – 488, 1996.

G. Kerley. The linear $u_s - u_p$ relation in shock-wave physics. Technical report, Kerley Techncal Services, https://arxiv.org/pdf/1306.6916.pdf, March 2006.

J. Kreeft and B. Koren. A new formulation of Kapila's five-equation model for compressible two-fluid flow, and its numerical treatment. *J. Comput. Phys.*, 229: 6220–6242, 2010.

B. Li, F. Habbal, and M. Ortiz. Optimal transportation meshfree approximation schemes for fluid and plastic flows. *Int. J. Numer. Methods Mech. Eng.*, 83:1541–1579, 2010.

L. Libersky, A. Petschek, T. Carney, J. Hipp, and F. Allahdadi. High strain Lagrangian hydrodynamics: A three-dimensional SPH code for dynamic material response. *J. Comput. Phys.*, 109:67 – 75, 1993.

L. Libersky, P. Randles, T. Carney, and D. Dickinson. Recent improvements in SPH modeling of hypervelocity impact. *Int. J. Impact Eng.*, 20(6–10):525 – 532, 1997.

G. Liu and M. Liu. *Smoothed Particle Hydrodynamics: A Meshfree Particle Method*. Singapore: World Scientific, 2003.

G. Liu, C. Zhou, and G. Wang. An implementation of the Smoothed Particle Hydrodynamics for hypervelocity impacts and penetration to layered composites. *Int. J. Comput. Methods*, 10:1350056 (1 – 23), 2013.

L. Lucy. A numerical approach to the testing of the fission hypothesis. *Astron. J.*, 1013 - 1024, 1977.

F. Macia, L. Gonzales, J. Cercos-Pita, and A. Souto-Iglesias. A boundary integral SPH formulation: Consistency and applications to ISPH and WCSPH. *Prog. Theor. Phys.*, 128(3):439–462, 2012.

L. Malvern. *Introduction to the Mechanics of the Continuous Medium*. Prentice-Hall, Inc., 1969.

S. Marsh, editor. *LASL Shock Hugoniot Data*. University of California Press, 1980.

V. Mehra and S. Chaturvedi. High velocity impact of metal sphere on thin metallic plates: A comparative Smooth Particle Hydrodynamics study. *J. Comput. Phys.*, (212):318–337, 2006.

J. Millett, N. Bourne, and D. Deas. The equation of state of two alumina-filled epoxy resins. *J. Phys. D: Appl. Phys*, 38:930 – 934, 2005.

J. Monaghan. Simulating free-surface flows with SPH. *J. Comput. Phys.*, 110(399 - 406), 1994.

J. Monaghan. SPH simulation of multi-phase flow. *Comput. Phys. Commun.*, 87: 225–235, 1995.

J. Monaghan. SPH and Riemann solvers. *J. Comput. Phys.*, 136(2):298 – 307, 1997.

J. Monaghan. Smoothed Particle Hydrodynamics. *Rep. Prog. Phys.*, 68(8):1703, 2005.

J. Monaghan. Smoothed Particle Hydrodynamics and its diverse applications. *Annu. Rev. Fluid Mech.*, 44:323 – 346, 2012.

J. Monaghan and R. Gingold. Shock simulation by the particle method SPH. *J. Comput. Phys.*, 52(2):374 – 389, 1983.

J. Monaghan and J. Lattanzio. A refined particle method for astrophysical problems. *Astron. Astrophys.*, 149:135 – 143, 1985.

J. Monaghan and D. Price. Variational principles for relativistic Smoothed Particle Hydrodynamics. *Mon. Not. R. Astron. Soc*, 328:381–392, 2001.

J. Monaghan and A. Rafiee. A simple SPH algorithm for multi-fluid flow with high density ratios. *Int. J. Numer. Methods Fluids*, 71(5):537–561, 2013.

R. Nelson and J. Papaloizou. Variable smoothing lengths and energy conservation in Smoothed Particle Hydrodynamics. *Mon. Not. R. Astron. Soc*, 270(1–20), 1994.

J. Owen, J. Villumsen, P. Shapiro, and H. Martel. Adaptive Smoothed Particle Hydrodynamics: Methodology II. *Astrophys. J. (supplement series)*, 116:155 – 209, 1998.

A. Parshikov and S. Medin. Smoothed particle hydrodynamics using interparticle contact algorithms. *J. Comput. Phys.*, 180:358 – 382, 2002.

L.-R. Plumerault. Numerical modelling of aerated-water wave impacts on a coastal structure, 2009.

D. Price. Modelling discontinuities and Kelvin–Helmholtz instabilities in SPH. *J. Comput. Phys.*, 227(24):10040 – 10057, 2008.

D. Price. Smoothed Particle Hydrodynamics and Magnetohydrodynamics. *J. Comput. Phys.*, 231:759 – 794, 2012.

K. Puri and P. Ramachandran. A comparison of SPH schemes for the compressible Euler equations. *J. Comput. Phys.*, 256:308 – 333, 2014.

J. Quirk and S. Karni. On the dynamics of a shock-bubble interaction. *J. Fluid Mech.*, 318:129–163, 1996.

T. Rabczuk, T. Belytschko, and S. Xiao. Stable particle methods based on Lagrangian kernels. *Comput. Methods Appl. Mech. Engrg.*, 193(12-14):1035–1063, 2004.

P. Randles and L. Libersky. Smoothed Particle Hydrodynamics: Some recent improvements and applications. *Comput. Methods Appl. Mech. Engrg.*, 139(1–4):375 – 408, 1996.

W. Riedel, H. Nahme, D. White, and R. Clegg. Hypervelocity impact damage prediction in composites: Part I & II. *Int. J. Impact Eng.*, 33:670 – 680, 2006.

B. W. Ritchie and P. Thomas. Multiphase smoothed-particle hydrodynamics. *Mon. Not. R. Astron. Soc*, 323(3):743–756, 2001.

W. Rudin. *Real and Complex Analysis*. McGraw-Hill Book Company, 3rd edition, 1987.

M. Salas. The curious events leading to the theory of Shock Waves. Lecture at the 17th Shock Interaction Symposium, 4-8 September 2006.

L. Schwartz. *Application of Distributions to the Theory of Elementary Particles in Quantum Mechanics*. Gordon and Breach Science Publishers, Inc., 1969.

R. Seliger and G. Whitham. Variational principles in continuum mechanics. *Proc. Roy. Soc. A*, 305(1-25), 1968.

K. Shintate and H. Sekine. Numerical simulation of hypervelocity impacts of a projectile on laminated composite plate targets by means of improved SPH method. *Compos. Part A*, 35(6):683 – 692, 2004.

G. Sod. A survey of several finite difference methods for systems of nonlinear hyperbolic conservation laws. *J. Comput. Phys.*, 27(1):1 – 31, 1978.

V. Springel and L. Hernquist. Cosmological Smoothed Particle Hydrodynamics simulations: the entropy equation. *Mon. Not. R. Astron. Soc*, 333:649–664, 2002.

J. Stewart. Positive definite functions and generalizations, an historical survey. *Rocky Mountain J. Math.*, 6(3):409–434, 1976.

J. Tillotson. Metallic equations of state for hypervelocity impacts. Technical report, Air Force Weapons Lab, 1962.

E. Toro. *Riemann Solvers and Numerical Methods for Fluid Dynamics - A Practical Introduction*. Springer-Verlag, Berlin-Heidelberg, 3rd edition, 2009.

R. Vacondio, B. Rogers, and P. Stansby. Accurate particle splitting for Smoothed Particle Hydrodynamics in shallow water with shock capturing. *Int. J. Numer. Methods Fluids*, 69:1377–1410, 2012.

R. Vacondio, B. Rogers, P. Stansby, and P. Mingosa. Variable resolution for SPH in three dimensions: Towards optimal splitting and coalescing for dynamic adaptivity. *Comput. Methods Appl. Mech. Engrg.*, 300:442 – 460, 2016.

R. Vignjevic, S. Lepage, and T. DeVuyst. Simulation of high velocity impacts on thin metallic targets I & II. In *International Conference on Impact Loading of Lightweight Structures*, 2005.

R. Vignjevic, J. R. Reveles, and J. Campbell. SPH in a total Lagrangian formalism. *CMES*, 14(3):181–198, 2006.

D. Violeau. *Fluid Mechanics and the SPH method*. Oxford University Press, 2012.

F. Whipple. Meteorites and space travel. *Astron. J.*, 52:131, 1947.

G. Whitham. *Linear and Nonlinear Waves*. John Wiley & sons, 1999.

M. Wicklein, S. Ryan, D. White, and R. Clegg. Hypervelocity impact on CFRP: Testing, material modelling, and numerical simulation. *Int. J. Impact Eng.*, 35(12):1861 – 1869, 2008.

C. Zhang, X. Hu, and N. Adams. A generalised transport-velocity formulation for Smoothed Particle Hydrodynamics. In *Proceedings of the 10th International SPHERIC Workshop*, 2015.

G. Zhang and R. Batra. Wave propagation in functionally graded materials by Modified Smoothed Particle Hydrodynamics (MSPH) method. *J. Comput. Phys.*, 222(1): 374–390, 2007.

C. Zhou, G. Liu, and K. Lou. Three-dimensional penetration simulation using Smoothed Particle Hydrodynamics. *Int. J. Comput. Methods*, 4(4):671–691, 2007.

I. Zisis, B. van der Linden, and C. Giannopapa. Towards a Smoothed Particle Hydrodynamics algorithm for shocks through layered materials. In *Proceedings of the 2013 ASME Pressure Vessels & Piping Conference*, 2013.

I. Zisis, R. Messahel, M. Souli, B. van der Linden, and B. Koren. Two-phase benchmarks for SPH multiphase fully compressible schemes. In *Proceedings of the 9th International SPHERIC Workshop*, Paris, France, 2014a.

I. Zisis, B. van der Linden, C. Giannopapa, and J. Dam. Smoothed Particle Hydrodynamics for hypervelocity impacts into inhomogeneous materials. In *Proceedings 2014 ASME Pressure Vessels & Piping Conference*, Anaheim, CA, USA., July 20-24 2014b.

I. Zisis, R. Messahel, B. van der Linden, A. Boudlal, and B. Koren. Validation of robust SPH schemes for fully compressible multiphase flows. *Int. J. Multiphysics*, 9:225 – 234, 2015a.

I. Zisis, B. van der Linden, C. Giannopapa, and B. Koren. On the derivation of SPH schemes for shocks through inhomogeneous media. *Int. J. Multiphysics*, 9:83 – 99, 2015b.

I. Zisis, J. Evers, B. van der Linden, and M. Duong. Recent results in the systematic derivation and convergence of SPH. (*submitted - preprint:* arxiv.org/abs/1612.06687 - *Libersky prize* for best student paper and presentation at the *11th International SPHERIC Workshop*), 2016a.

I. Zisis, B. van der Linden, C. Giannopapa, J. Dam, and B. Koren. Towards detailed material deformation patterns in the hypervelocity impacts of laminated plates with Smoothed Particle Hydrodynamics. In *Proceedings 2016 ASME Pressure Vessels & Piping Conference*, 2016b.

J. Zukas. *Introduction to Hydrocodes*. Elsevier Ltd., Amsterdam, 1st edition, 2004.

Acknowledgments

My PhD study was a great journey. Gladly, it lacked the hurdles of Odysseus on his way to Ithaca and I did not have to fight against windmills like Don Quixote. Still, it was the kind of journey which marks a whole life. And on this journey I did not feel alone, due to the contributions of the following people.

First and foremost, I would like to thank Barry, my promoter for diligently reading every manuscript I gave him. Apart from the precious scientific knowledge, the teachings I got from him: precision, correction towards perfection and an optimistic spirit in research, will follow me.

Our discussions with Bas, my first co-promoter, followed a purely Hegelian pattern: a blunt *thesis* from my side, a fierce *antithesis* from his side and a healing *synthesis* in the end. I am grateful to him for his questioning helped me build my current mathematical understanding. Additionally, he should be credited for teaching me proper coding, while we were developing the LimeSPH code, and taking care such that I build a multidisciplinary curriculum.

Christina, my second co-promoter, was the first person from CASA whom I met, when after my application for the PhD position, I received her email about arranging a first interview in Athens. I thank her for reading my thesis, providing me advice on how to choose collaborations and for giving me tips for academic-style paper-writing.

Regarding the members of my PhD committee, I would like to thank dr. Sjoerd Rienstra and prof. Federico Toschi for accepting to comment on my thesis, prof. Mhamed Souli, for reading my thesis and for his outstanding hospitality whenever I visited U Lille. Finally, Dr. Gerhard Drolshagen, for the times he welcomed me at ESA/ESTEC and for reviewing my thesis.

There are other two persons, whom I would like to thank: prof. Bob Mattheij for entrusting me with this PhD research position and for securing its funding when bureaucratic reasons put it at stake, as well as prof. Jacques Dam for accepting me in the PhD project and leading the hypervelocity impact experiments.

I am more than grateful to my co-authors Joep and Hong; without their help in understanding measure-valued evolutions, this work would be of far less value and the Libersky prize would only be a wild dream. Moreover, I would like to thank my coauthor Ramzi, for working together and advancing our knowledge on shock problems and SPH. I am thankful to Stan and Darcy for our SPH-related discussions during our PhD years, as well as to Upanshu, for all the times I disturbed him for a mathematical question. Additionally, Michiel is to be thanked for a year of supervising me, with discussions on numerics and Matlab, and Fons for helping me formalize the part on plasticity. Finally, I am thankful to Enna for lifting the burden of all bureaucratic issues.

CASA will stay in my mind as home of my scientific growth. I would also like to thank M2i and LIME for all they contributed to the project. Additionally, Fraunhofer EMI in Freiburg and FMLC in Delft (specifically Rob Leonard) for their commitment in our experimental work.

From all my friends, I think everyone has received a big ”thank you” one way or another. Friends with whom we pub-crawled in my first years in Eindhoven, friends who came to visit me in Eindhoven and above all, friends —I should be explicit here: Giovanni— who made ”The Mansion” at Kabelstraat deserve its legendary reputation!

An enormous ”thank you” goes to my parents, Alkis and Roula, for all their support and advice while I am following my research and life choices. I am eager to congratulate my brother Foivos for his own research achievements in a few years. And last but far from least, my loving thanks go to my girlfriend Olga, for being my partner in PhD agonies, extraordinary travels and the challenge of living together.

Biography

Iason Zisis was born on October 1st, 1985, in Athens, Greece, where he also grew up. Upon graduation from the Anavryta Experimental Lyceum, in September 2003, he started studying Mechanical Engineering at the National Technical University of Athens.

He concluded his graduate studies with a thesis on Computational Fluid Dynamics and then, in April 2011, he opted for deepening his understanding of Mathematics with a PhD project at the Department of Mathematics and Computer Science of the Eindhoven University of Technology, The Netherlands. What you now read is the result of that work.

For contributing to the understanding of the Smoothed Particle Hydrodynamics (SPH) computational method, he was awarded the Libersky prize at the 11th International Workshop of the SPH European Research Interest Community, June 2016, Munich, Germany.

He is currently working on mesh generation algorithms for simulations with the finite volume method, at Praxis Software, in Patras, Greece.